8-2014

Calcitized Evaporites in the Precambrian: Deposition and Diagenesis in a Low Sulfate Ocean

Ashley René Manning Berg
University of Tennessee - Knoxville, aberg@vols.utk.edu

To the Graduate Council:

I am submitting herewith a thesis written by Ashley René Manning Berg entitled "Calcitized Evaporites in the Precambrian: Deposition and Diagenesis in a Low Sulfate Ocean." I have examined the final electronic copy of this thesis for form and content and recommend that it be accepted in partial fulfillment of the requirements for the degree of Master of Science, with a major in Geology.

Linda C. Kah, Major Professor

We have read this thesis and recommend its acceptance:

Christopher M. Fedo, Theodore C. Labotka

Accepted for the Council:
Carolyn R. Hodges

Vice Provost and Dean of the Graduate School

(Original signatures are on file with official student records.)

Calcitized Evaporites in the Precambrian: Deposition and Diagenesis in a Low Sulfate Ocean

A Thesis Presented for the
Master of Science
Degree
The University of Tennessee, Knoxville

Ashley René Manning Berg
August 2014

DEDICATION

I would like to dedicate this thesis to my grandfather, “Pops,” for teaching me that any goal is obtainable with hard work and dedication.

ACKNOWLEDGEMENTS

I would like to thank the faculty, staff, and students, at the University of Tennessee Department of Earth and Planetary Sciences, who have supported and assisted me in my pursuit of degree.

I would like to thank my advisor, Dr. Linda Kah, for her guidance and encouragement, and my committee members, Dr. Chris Fedo and Dr. Ted Labotka for their assistance. Dr. Julie Bartley at Gustavus Adolphus College, for introducing me to geology and the Precambrian, for all of the support and mentoring, and time sacrificed discussing my research and helping me collect my ICP data.

I would also thank the organizations who have financially supported my research: The Geological Society of America (GSA), The Society for Sedimentary Geology (SEPM), Sigma Xi, and The University of Tennessee Department of Earth and Planetary Sciences.

Finally, I would like to thank my husband, Chris for his patience and support, including the numerous discussions regarding "ingredients capable of becoming interesting rocks." Thank you mom, dad, grandma, and Cassidy for always being there, willing to listen, and ready to help in any way possible. And a special thanks to my niece for brightening up my world with her new found love of rocks.

ABSTRACT

One of the most profound byproducts of the Great Oxidation Event (GOE) was the onset of oxidative weathering on land and the riverine delivery of sulfate to marine systems. The marine sulfur system therefore plays a critical role in reconstructing the oxygenation of the early Earth. Although the exact nature of marine oxygenation in aftermath of GOE remains uncertain, examination and modeling of marine sulfate suggest that sulfate concentrations remained below 2 millimolar (mM) until at least the middle Mesoproterozoic, and may have only reached about 10 mM in the latest Neoproterozoic. Such a low concentration of marine sulfate had dramatic effects on the deposition and diagenesis of marine sulfate deposits. Prior to the Mesoproterozoic, precipitation of sulfate evaporites was inhibited by the low concentration of marine sulfate and potentially by elevated carbonate saturation. The first indisputable gypsum-anhydrite deposits occur in a variety of fluvial, playa, and marine sabkha environments at 2.1 Giga annum (Ga), although much of the rock record is represented by relatively few pseudomorphs and molds. The first laterally extensive, marine sulfate evaporite deposits are found in the late Mesoproterozoic, where up to 60 meters of bedded marine gypsum and anhydrite occur within the Grenville Supergroup, and gypsum beds up to several meters thick occur in the lower Bylot Supergroup. Together, these occurrences indicate that, by the mid-Mesoproterozoic, marine sulfate concentrations were sufficient to sustain the first widespread evaporite deposition.

Unfortunately, our understanding of the dynamics of marine sulfate reservoir growth is hampered by the sparse preservation of marine evaporites. Here I present a series of unusual limestone deposits in the 1.1 Ga Atar Group Formation, Toudeni Basin, Mauritania, that contain both macroscopic and microscopic features suggestive of a primary origin as sulfate evaporites. Carbon- and oxygen-isotope compositions indicate a history of diagenesis similar to that of surrounding marine limestones. Elemental concentrations, however, show retention of elevated sodium and potassium, suggesting retention of original hypersaline composition. Models of potential fluid composition indicate deposition under low sulfate, high salinity conditions, with diagenetic calcitization under low water–rock ratios from a combination of fresh, marine, and hypersaline marine fluids.

TABLE OF CONTENTS

LIST OF TABLES

LIST OF FIGURES

CHAPTER 1: INTRODUCTION

The evolution of the early Earth was marked by fundamental changes in the extent of Earth surface oxygenation, which is reflected in complex and changing redox behavior in marine systems (Johnston et al., 2006; Scott et al., 2008; Laakso and Schrag, 2013). Over the last decade, the marine sulfur system has played a critical role in unravelling marine evolution (Claypool et al., 1979; Habicht et al., 2000; Farquhar and Wing, 2003; Strauss, 2003; Bekker et al., 2004; Canfield, 2004; Bottrell and Newton, 2005; Kaufman et al., 2007; Lyons and Gill, 2010; Scott et al., 2011). During the Archean, Earth had a reduced biosphere with little sulfate available within the oceans (Pavlov and Kasting, 2002; Canfield et al., 2000; Kah et al., 2004; Lyons and Gill, 2010). The earliest evidence of widespread Earth surface oxidation occurs at the ~2.4 Ga great oxidation event (GOE) which is recorded in the appearance of oxidized terrestrial sediments (Melezhik et al., 2010; Bekker and Holland, 2012), in the disappearance of detrital pyrite, siderite, and uraninite (Bekker and Holland, 2012; Johnson et al., 2014), the largest known positive excursion of $\delta^{13}C$ (Karhu and Holland, 1996; Melezhik et al., 2012; Bekker and Holland, 2012), and the disappearance of mass-independent (MIF) sulfur isotopic signatures (Farquhar et al., 2000; Guo et al., 2009; Ono et al., 2003). Oxygenation of the biosphere likely reflects the irreversible oxidation of the mantle reservoir resulting from a combination of escape of upper atmospheric hydrogen into space, changes in the composition of volcanic gas, and changes in the rate of oxygen production (see review in Kah and Bartley, 2011).

One of the most profound byproducts of the GOE was the onset of oxidative weathering on land and the riverine delivery of SO_4 to marine systems. Atmospheric oxidation had a dramatic effect on the marine sulfur cycle, particularly in the loss of MIF sulfur signatures (Farquhar et al., 2000; Farquhar and Wing, 2003), and in the fractionation between sedimentary sulfide and sulfate associated with increased marine sulfate concentration (Shen et al., 2002). Analysis of sulfur isotopes during fractionation experiments indicates that Archean oceans likely had <200 μmol of sulfate (Habicht et al., 2002). At this low concentration, bacterial sulfate reduction (BSR) shows minimal S-isotope fractionation, <10‰, consistent with the sulfur isotope record prior to the GOE. At concentrations >200 μmol, BSR has substantially greater effect on fractionation (Habicht et al., 2002; Strauss, 2003).

The extent of marine oxygenation in aftermath of GOE, however, remains uncertain (Kah and Bartley, 2011). Reservoir-size modeling suggests that sulfate concentrations remained below 2 mM (modern marine sulfate concentrations are 28 mM; Kah et al., 2004; Spear et al., 2014) until at

least the mid-Mesoproterozoic, and may have reached only approximately 10 mM in the latest Neoproterozoic (Kah et al., 2004). The geologic record of marine evaporites also provides evidence regarding the evolution of marine sulfate. Prior to the Mesoproterozoic, precipitation of sulfate evaporites was likely inhibited by a small marine sulfate reservoir and potentially, by elevated carbonate saturation (Grotzinger, 1989; Grotzinger and Kasting, 1993; Kah et al., 2001). The first indisputable evaporite deposits are recorded as anhydrite-containing pseudomorphs after Ca-sulfates (Melezhik et al., 2005) that occur within a variety of fluvial, playa, and sabkha environments at 2.1 Ga. These pseudomorphs have been argued to indicate well-oxidized surface waters associated with a dramatic—although potentially short-lived—increase in the size of the marine sulfate reservoir (Melezhik et al., 2005; Bekker and Holland, 2012). An alternative hypothesis suggests that these evaporites, which occur within a thick succession of terrigenous deposits, may reflect elevated oxidative weathering and sulfate delivery to marginal marine environments whose sulfate concentrations may have been higher than that of the global ocean (Chakrabarti et al., 2014). After 2.1 Ga, evidence for sulfate evaporite deposits is represented by only a few observations of possible gypsum pseudomorphs and gypsum molds (Cook and Ashley, 1991; Grotzinger and Kasting, 1993; Pope and Grotzinger, 2003; Gandin and Wright, 2007; Braiser et al., 2011; Bekker and Holland, 2012) until the mid-Mesoproterozoic.

The first laterally extensive, demonstrably marine, sulfate evaporites are found in the late Mesoproterozoic (Kah et al., 2001; Whelan et al., 1990). Up to 60 meters of bedded marine gypsum and anhydrite occurs within the ~1.1 to 1.3 Ga Grenville Supergroup and has been interpreted to represent evaporation within an isolated marine basin (Whelan et al., 1990). Similarly, gypsum beds up to several meters thick occur throughout the lower portion of the ~1.1 Ga Society Cliffs Formation (now Angmaat Formation; Turner and Kamber, 2012) of northern Baffin and Bylot islands, which are interpreted to reflect repeated episodes of evaporation within marine peritidal environments (Kah et al., 2001). Together, these two occurrences indicate that, by the mid-Mesoproterozoic, sustained delivery of sulfate to the oceans had resulted in surface environments with sulfate concentrations exceeding that which was removed from these environments by bacterial sulfate reduction (BSR).

Unfortunately, our understanding of the dynamics of marine sulfate reservoir growth is hampered by the sparse preservation of marine evaporites. Estimates of marine sulfate concentration have been derived from proxies involving the isotopic composition of sulfur from both marine pyrite and carbonate associated sulfur (CAS) (Shen et al., 2002; Kah et al., 2004), and

integration with other proxy information such as biomarkers (Blumenberg et al., 2012; Brocks et al., 2005), and redox sensitive metals (Canfield, 2005) like iron (Lyons and Severman, 2006; Anderson and Raiswell, 2004; Wijsman et al., 2001) molybdenum (Neubert et al., 2008; Scott et al., 2008; Duan et al., 2010; Gilleaudeau and Kah, 2013a), and chromium (Frei et al., 2009; Guo et al., 2009) that mark the presence of sulfidic environments (i.e. environments which contain free hydrogen sulfide). These data support a view of protracted oxygenation, and suggest only 1-2% (<0.5 mM) of present marine sulfate concentrations (28mM) in the Early Mesoproterozoic, as much as 5-7% (~1.5 mM) present concentrations by late Mesoproterozoic, and perhaps as much as 10% (<3 mM) present concentrations by the end of the Proterozoic (Kah et al., 2004).

A better understanding of both the distribution of sulfate evaporites and their diagenesis may help constrain the environments in which early evaporite deposits formed and, thus, provide further constraint on the broader story of marine oxygenation and chemical evolution. Here we focus on the series of unusual limestone deposits in the 1.1 Ga Atar Group Formation, Toudeni Basin, Mauritania (Kah et al., 2012), that contain macroscopic features suggestive of a primary origin as sulfate evaporites. Fabrics and textures of these unusual limestone deposits are described on both the macroscopic and microscopic scale in order to identify the range of primary and secondary fabrics. Carbon and oxygen isotopic compositions and the concentration of major and trace elements is then used to reconstruct the potential composition of primary depositional environments, as well as secondary diagenetic fluids that may have acted to alter primary components. Finally, geochemical modeling is used to explore the behavior of evaporite deposition and diagenesis in a potentially low sulfate ocean.

CHAPTER 2: GEOLOGIC SETTING

Regional Geology

The Taoudeni basin extends more than 1,750,000 km^2 and preserves more than 2000 m of flat-lying, unmetamorphosed sedimentary strata (Pique, 2001; Rooney et al., 2010; Kah et al., 2012) that overlie Archean amphibolite and quartzo-feldspathic schist, and Paleoproterozoic granite of the Archean Reguibat and Leo Shields (Fig. 1) (Villeneuve and Cornée, 1994). Strata of the Tauodeni Basin are subdivided into three unconformity-bounded units: the Char, Atar, and Assabet el Hassiane Groups (Bertrand-Sarfati and Moussine-Pouchkine, 1988). The Char Group consists of fluvial and marine sediment deposits that mark the onset of sedimentation on the craton in the aftermath of cratonal rifting events (Benan and Deynoux, 1998). The Atar Group (Fig. 2) consists of alternating carbonate and siliciclastic rocks that mark tectonic stabilization, craton-wide flooding, and depositional control via changes in sea level and regional subsidence (Bertrand-Sarfati and Moussine-Pouchkine, 1988; Kah et al., 2012; Gilleaudeau and Kah, 2013a). Finally, the Assabet el Hassiane Group is composed of predominantly shallow siliciclastic deposits that were deposited above a basinwide unconformity that caps the Atar Group (Bertrand-Sarfati and Moussine-Pouchkine, 1988). Proterozoic strata were not deeply buried or exposed to temperatures higher than 100°C, although local post-deposition deformation and hydrothermal alteration occurred within the basin post-deposition (Girard et al., 1989; Rooney et al., 2010; Blumenberg et al., 2012).

Atar Group Strata

The Atar Group preserves the most lithologically variable strata within the basin and is subdivided into ten formations. In its type locality near the town of Atar (Fig. 1), strata consist of alternating deposits of stromatolite-bearing carbonate, fine-grained shale, and sandstone (Bertarand-Sarfati and Moussin-Pouchkine, 1988; Kah et al., 2012). Coarse- to medium-grained, fining-upward fluvial to marine sandstone of the Foum Chor Formation (unit I-3) comprises the basal unit of the Atar Group, which unconformably onlaps strata of both the Char Group and underlying basement. The overlying Ksar Torchane Formation (unit I-4) is marked by fining upward siliciclastic deposition during marine transgression.

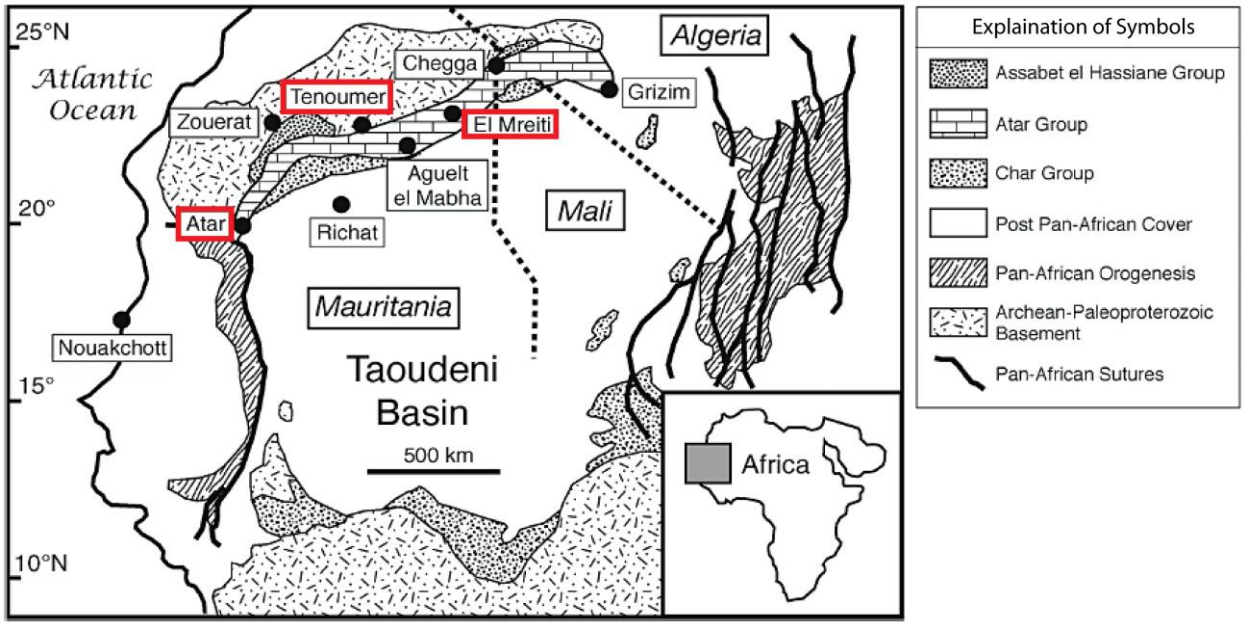

Figure 1. Geologic map of the Taoudeni Basin (after Kah et al., 2012). Highlighted areas mark outcrop and drill core sample localities.

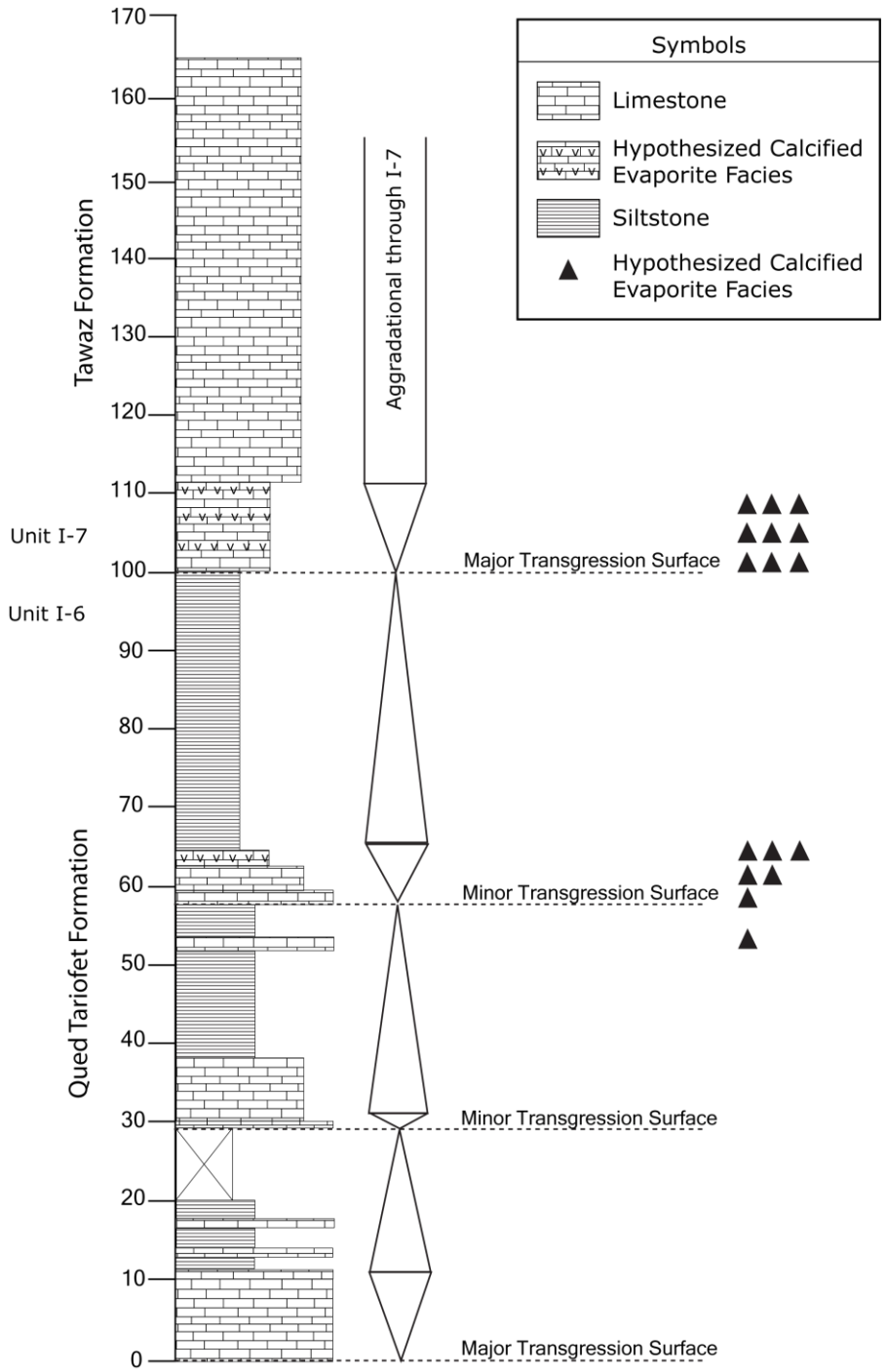

Figure 2. Stratigraphy of Units I-6 and I-7 within the Atar Group, as measured near Atar (Kah et al., 2012). Bright white limestone beds within Units I-6 and I-7 (triangles, with number of triangles marking abundance) have massive laminar and nodular fabrics, stylolites and microkarstic fabrics and have been hypothesized to be calcitized evaporite facies. Potential calcitized evaporite facies mark marine transgression (and concomitant decrease in influx of terrigenous sediment) within restricted marginal marine environments of Unit I-6 and the basal portion of Unit I-7, after which open marine deposition is reestablished.

Carbonate deposition in the uppermost Ksar Torchane Formation unit marks the onset of marine deposition in the Atar Group (Kah et al., 2012).

Unit I-5, the Atar Formation, is characterized by the development of three distinct stromatolite reef units, the bases of which mark successive marine transgressions (Kah et al., 2009; Kah et al., 2012). An abrupt regression at the top of Atar Formation is marked by deposition of the Oued Tarioufet Formation (unit I-6), which is dominated by silt and fine sand-sized siliciclastic influx and restricted carbonate facies, until shallow marine deposition is re-established near the boundary with the lower Tawaz Formation (unit I-7), which marks return of shallow marine to intertidal stromatolitic deposition (Kah et al., 2012). Units I-8 through I-12 of the Atar Group are composed of alternating carbonate and fine-grained siliciclastic deposits deposited in intertidal to shallow subtidal environments (Bertrand-Sarfati and Moussine-Pounchkine, 1985; Kah et al., 2012).

This investigation focuses on the Oued Tariofet Formation (I-6) and basal Tawaz Formation (I-7) (Fig. 2), which are marked by the presence of bright white, massively-bedded, and locally microkarstic limestone (Goodman and Kah, 2004; Kah et al., 2012). In the north and northeastern part of the basin where core samples were obtained (Fig 1), these units are correlated with the Gouamir and Tenoumer formations (Moussine-Pouchkine and Bertrand-Sarfati, 1997; Kah et al., 2012; Gilleaudeau and Kah, 2013b). Facies within the north and northeastern parts of the basin represent deposition in a shallow, epicontinental sea (Gilleaudeau and Kah, 2013b), generally contain a higher proportion of fine-grained (silt to clay-sized) siliciclastic material, and commonly record brecciation related to subaerial exposure (Gilleaudeau and Kah, 2013b). The Gouamir consists predominantly of interbedded shale, siltstone, and clay but contains several distinct bright white, nodular and laminar horizons that are similar to those in the correlative Oued Tariofet Formation (Gilleaudeau and Kah, 2013b). The overlying Tenoumer Formation is predominantly limestone, with distinctly shaly limestone and bright white limestone beds in the lowermost 20 meters. In both outcrop and core, potential calcitized evaporite facies are associated with a decrease in the influx of terrigenous sediment and reappearance of marine carbonate. These intervals are therefore interpreted to represent marine transgression within restricted marginal marine environments.

CHAPTER 3: MATERIALS AND METHODS

Samples

Samples of distinct bright white limestone beds were collected primarily from drill core (Fig. 1), and augmented by previously collected outcrop material (Goodman and Kah, 2004; Kah et al., 2012). Core samples include primarily material from the R2 core, which was drilled north of the town of Atar, and retrieved 111 m of Unit 1-7 (and possibly the uppermost beds of unit I-6); and the R1 core, which was drilled near Tenoumer, and retrieved samples between the base of Unit I-5 through the top of Unit I-7. Additional samples were examined from the F4 core collected near El Mreiti in the north-central part of the basin. Samples from the F4 core were influenced by hydrothermal fluid flow (450-525 °C; Girard et al., 1989; Rooney et al., 2010; Blumenberg et al., 2012) related to local emplacement of diabase dikes and sills during the Mesozproterozoic Central Atlantic Magmatic Province (Girard et al., 1989). Obvious alteration associated with these intrusions is limited to narrow zones of contact metamorphism (i.e., less than 10 meters at either side of a sill that cuts the F4 core), although moderately thermal fluids (<170 °C; Girard et al., 1989), may have circulated more widely.

Intervals containing potential calcitized evaporites were identified by their bright white color and abundant stylolitization, and were sampled every 10–20 cm. Additional studies (Blumenberg et al., 2012; Gillaudaeu and Kah 2013a, 2013b) characterized associated rock types within these cores.

Petrographic Procedures

After examination of mesoscale fabrics in core, paired thin sections and polished thick sections were analyzed by a combination of plane and polarized light, cathodoluminescence (CL), and scanning electron microscopy (SEM) to characterize and evaluate rock fabrics. Plane and polarized light microscopy were performed on an Olympus BM60 microscope equipped with an accompanying Q-Imaging Micropublisher 5.0 camera, and were used to determine the range of fabrics preserved in the samples, the presence of any potential evaporite pseudomorphs, and the degree and style of recrystallization (cf. Kendall, 2001; Sanz-Rubio et al., 2001; Ulmer-Scholle and Scholle, 1994; Fernandez-Diaz et al., 2009; Reuschel et al., 2011). Cathodoluminescence (CL) petrography, performed on an ELM-3RP Spectrumedix luminoscope equipped with an Optronix low light CCD camera, aided in the diagnosis of fabrics and provided insight into recrystallization

pathways (cf. Pierson et al., 1981; Hemming et al., 1989; Savard et al.,1995; Habermann et al., 1998). Finally, SEM energy-dispersive x-ray spectroscopy (EDX) was performed on an FEI Quanta 200 environmental scanning electron microscope (ESEM). SEM was used to help identify patterns of recrystallization related to specific depositional or diagenetic fabrics, and EDS elemental maps were used to highlight the distribution of specific elements such as sulfur, sodium, and potassium, which indicate paleosalinity.

For SEM analysis areas of interest were determined through thin section analysis and marked on polished thick sections. Thick sections were then placed in the SEM oriented in the same direction. Maps were produced using Brunker's ESPIRIT software and continuous data was collected at a voltage of 20 kV and spot size of 4.5 μm under low vacuum conditions with a partial pressure of 0.45 T. Interaction of electrons with the surface of the sample results in x-ray emissions at wavelengths that are collected by the EDX detector, producing elemental spectra (or maps). Images were produced at a working distance of 10 mm and elemental analyses were performed at a working distance of 13 mm in order to obtain higher quality data.

Geochemical Procedures

Isotopic and elemental compositions of bulk samples were used to help determine the range in chemical composition, which should reflect a combination of primary minerals and subsequent water–rock interaction that occurred during diagenesis (Veizer, 1983; Brand and Veizer, 1980, 1981; Banner and Hanson, 1990; Marshall, 1992; Brand, 2004).

Sulfate Concentrations

The amount of sulfur present in these samples was measured by sulfur coulometry and by extraction of carbonate-associated sulfate (CAS; i.e., sulfate encompassed within the carbonate structure). For coulometric analysis, 50 mg of powdered sample was placed on a disposable ceramic boat with an excess of V_2O_5 and heated to 1000°C in a UIC CM350 Total Sulfur Analyzer. Sulfur species released as the sample is heated are converted to SO_2, which, along with H_2S, is then transferred to an acidification cell, where total sulfur is measured by standard coulometric titration. Multiple readings provide precision of 0.25%, with total sulfur provided in milligrams per sample.

Because coulometric analysis provides a measurement of total sulfur (i.e., including sulfur from both sulfate and sulfide phases) sulfur content was also measured by extraction of carbon-associated sulfate. Carbonate-associated sulfate (also referred to as SSS, or Structurally Substituted

Sulfate; Kampschulte and Strauss, 2004) consists of trace amounts of sulfate that is substituted into the carbonate structure, presumably as direct substitution for carbonate in the crystal lattice (Takano, 1985; Staudt et al., 1994; Pingitore et al., 1995). To extract CAS, approximately 100 g of powdered sample were dissolved in 3N HCl. During dissolution, 5-10 mL aliquots of HCl were added to samples, which were stirred on a magnetic stir plate until no additional reaction was visible. Additional aliquots were delivered until dissolution was complete, approximately 500–600 mL of HCl were added to each sample. During dissolution, pH was monitored and kept as close to neutral as possible, to avoid dissolution of iron sulfide phases. Insoluble residue was removed by vacuum filtration, dried, and analyzed by X-ray diffraction. Approximately 140 mL of saturated $BaCl_2$ solution was added to the filtrate and left overnight to complete reaction of filtrate sulfate to form $BaSO_4$. The $BaSO_4$ filtrate collected by vacuum filtration and dried before being weighed. A mass calculation was then performed to determine the amount of sulfate present in the sample.

Because petrographic analyses revealed some samples to contain a minor amount of hydrocarbons, an additional step was performed on these samples in order to remove any organically bound sulfur before CAS extraction. Samples containing visible hydrocarbons were soaked for 24 hours in a 6% NaClO solution, and multiply rinsed in Milli-Q water, prior to the addition of HCl. Samples without petrographically visible organic matter did not undergo this step during CAS extraction.

Carbon and Oxygen Isotopes

Carbon and oxygen isotope analyses were performed at the University of California at Santa Cruz. Milligram sample splits were analyzed for $\delta^{18}O$ and $\delta^{13}C$ isotopes by acid digestion using an individual vial acid drop ThemoScientific Kiel IV carbonate device interfaced to ThermoScientific MAT-253 dual-inlet isotope ratio mass spectrometer (IRMS). Samples were reacted in orthophosphoric acid (specific gravity = 1.92 g/cm^3) at 75°C to generate carbon dioxide, which was cryogenically purified prior to introduction into the IRMS. Multiple runs of a Carrera Marble standard, calibrated to NIST Standard Reference Materials (NBS-19, NBS-18, and LSVEC), were used to correct the data which includes correction for machine drift. Four NBS-18 limestone standards were also used to correct for instrument specific source ionization effects, and two NBS-19 limestone samples were run to monitor quality control and long term performance. Results are expressed in delta notation relative to international standards PDB (PeeDee Belemnite) for $\delta^{13}C$ and $\delta^{18}O$ (UCSC Stable Isotope Laboratory, 2008)

$$\delta‰ = [(R_{sample}/R_{VPDB})] - 1) * 1000 \quad (1)$$

where R is the ratio ($^{13}C/^{12}C$) for carbon and ($^{18}O/^{16}O$) for oxygen. Precision of these measured values is ±0.08‰.

Trace Elements

A variety of major, minor, and trace elements were measured using inductively coupled plasma mass spectrometry. A standard suite of major, minor, and trace elements (Ca, Mg, Sr, Mn, Fe) was measured to infer potential primary and diagenetic fluid compositions (Brand and Veizer. 1980; Marshall, 1992). Additional trace elements (Na and K) were measured as potential indicators of hypersaline conditions. Elemental analyses were run at Gustavus Adolphus College in St. Peter, Minnesota, on an Agilent Technologies 7700 Series ICP-MS. Approximately 10 mg of powdered sample were placed into a centrifuge tube, and dissolved in 3 mL of 2% HNO_3. Samples were then centrifuged at 950 RPM for 10 minutes to pellet insoluble residue. Liquid was transferred to a new vial, and 6 mL of 2% NH_3 were added. Based on replicate analyses of lab standards, the precision on major elements is ±2.5% and ±5% on trace elements. ICP-MS results provide elemental concentrations within the liquid, which was used calculate the concentration of elements within the rock.

X-ray Diffraction

To identify non-carbonate phases, insoluble residue from whole rock powders obtained from CAS were analyzed using x-ray diffraction (XRD) with a Rigaku Ultima IV at the University of Tennessee. Measurements were taken at a step size of 0.02, between 4° and 70° 2θ, at 40 kV and 30 mA. Resulting spectra were analyzed via PDXL software.

CHAPTER 4: RESULTS AND INTERPRETATION

Petrographic Fabrics

Macro- and Mesocale Fabrics

Bright white limestone beds within the Atar Group (Fig. 3) occur within peritidal carbonate rocks of units I-6 (Gouamir Formation) and I-7 (Tenoumer Formation), within intervals that are marked by progradation of terrigenous sand and silt into a marginal marine realm. These limestone beds can be massive (up to 40 cm thick), but are more commonly represented by intervals (up to 1.5 meters in thickness) composed of cm-scale laminae separated by stringers of quartz silt and rare clay drapes. In both outcrop and core materials, these intervals are also marked by prominent stylolites every 2-10 cm. Stylolites are typically absent from over- and underlying carbonate-dominated facies.

In outcrop, massive and laminated intervals contain evidence of both laterally continuous deposition and laterally discontinuous, irregularly shaped nodules (2-10 cm in diameter), suggesting a potential combination of deposition at the sediment-water interface as well as growth within the substrate (Fig 3B, C). Additionally, several beds show evidence of development of microkarstic surfaces and dissolution collapse.

Core materials reveal macro- and mesoscale fabrics similar to that observed in outcrop, particularly the presence of a combination of massive, laminar, and cm-scale nodular fabrics (Fig. 4A-F). Greater concentrations of detrital clay, mica, and quartz silt in core materials also preserve nodular fabrics on the mm- to cm-scale (Fig. 4E-F). The most prominent fabric within core materials, however, are sedimentary breccias (cf., Fig. 5A, B, D). These breccias contain a combination of platy to nodular clasts. Platy clasts are typically 1-10 mm in length and approximately 1 mm in thickness, show angular terminations, and sometimes contain internal, sub-mm scale laminae. By contrast, nodular clasts are 2-10 mm in length and 3-4 mm in thickness, are irregular to rounded in their morphology, and show no indication of internal lamination.

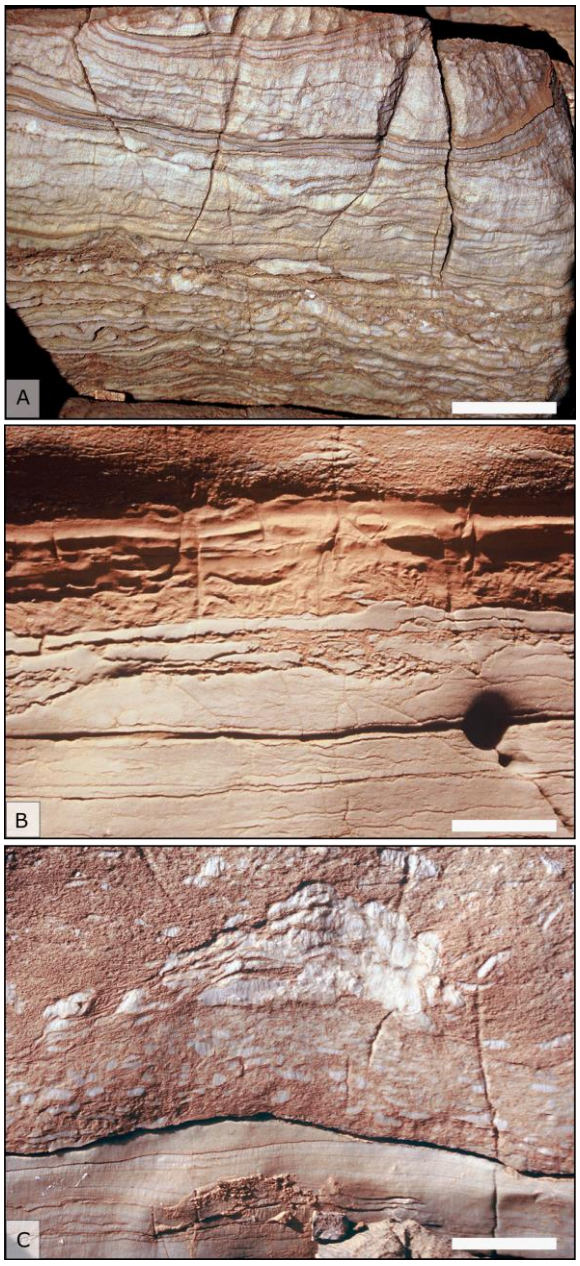

Figure 3. Bright white carbonate beds within the Atar Group. (A) Bright white limestone beds contrast sharply with grey and orange weathering limestone and silty limestone of the Atar Group. Here, a single laterally continuous bed within the lowermost Tawaz Formation (unit I-7). Massive to nodular textures common in outcrop. (B) Massive bright white limestone showing karstic dissolution at the upper surface and dissolution collapse features, overlain by a discrete horizon of siltstone. (C) Massive to nodular fabrics overlain by breccia containing substantial siliciclastic material and, fragments of bright white limestone, and discrete nodules. Scale bars are 5 cm in all images.

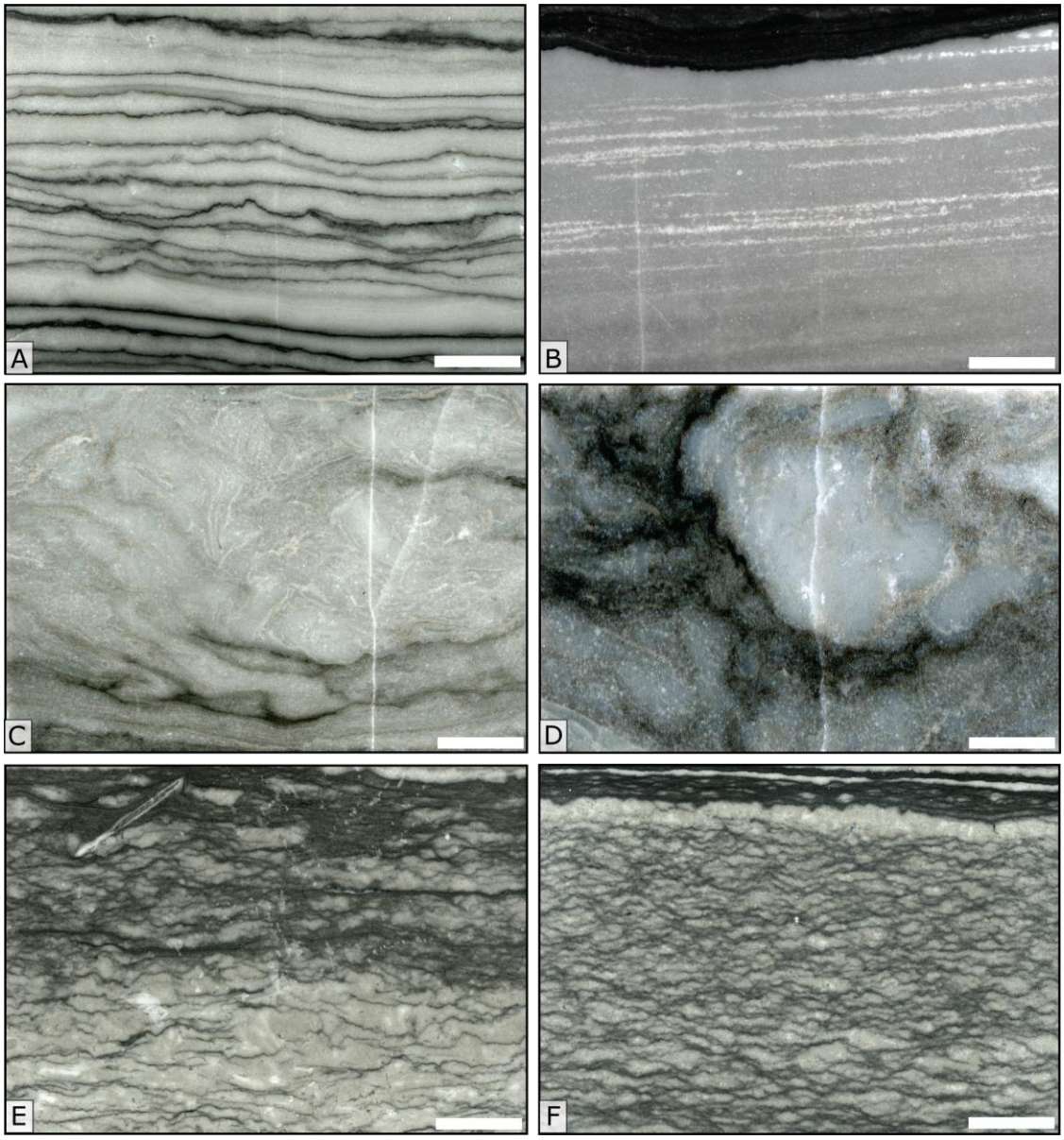

Figure 4. Preserved textures within bright white carbonate facies of the Atar Group. (A) Massive bedding with planar lamination. (B) Planar laminated fabric with laminae defined by detrital clay and silt. Detrital laminae also contains abundant euhedral dolomite, suggesting that detrital layers were conduits for secondary fluid flow. (C) and (D) Centimeter-scale nodular regions, defined by thin partings of detrital clay. (E) and (F) Millimeter-scale nodules separated by silt- and clay stringers, that coalesce (in E) into larger nodular masses. Scale Bar is 0.5 cm in all images.

Microscale Fabrics

Petrographic examination of samples reveals a variably recrystallized fabrics. Massive textures are composed predominantly of uniformly coarse spar (20-80 μm diameter) that displays predominantly anhedral crystals with irregular intercrystalline boundaries (Fig 5A) (i.e. equivalent to nonplanar crystal fabrics described by Sibley and Gregg, 1987). Laminated and nodular fabrics (Figs 5B-C) similarly consist of anhedral carbonate spar, and contain approximately 2% rounded to angular quartz silt (<60 μm diameter) and rare, unoriented mica flakes. Individual carbonate laminae and nodules are separated by irregular, dense laminae that consist predominantly of clay, mica, quartz silt and 25-40 micrometer euhedral dolomite rhombs (with quartz silt and dolomite visually estimated 10% to 20%, respectively). Samples with a greater abundance of silt and clay commonly show evidence of stylolitization that ranges from minor condensation of clay- and silt-rich laminae to development of highly irregular dissolution seams. In both cases, concentration of dolomite rhombs suggest that clay- and silt-rich intervals acted as pathways for secondary fluid flow.

Clastic breccia samples show the greatest variation in carbonate fabric development (Fig. 5). Clasts can be tightly to sparsely packed, are sometimes arrayed in edgewise rosettes, and are typically encompassed by anhedral carbonate spar (typically 50-200 μm diameter; Fig. 5C). Angular, platy clasts are composed predominatly of fine, anhedral microspar crystals (<20 μm diameter) or, in some cases, of distinctive, uniform, equant microspar referred to as molar-tooth microspar (Fig. 5C, E; Furniss et al., 1998; Pollock et al., 2006; Bishop and Sumner, 2006). By contrast, nodular clasts contain no clear evidence of primary lithology. Rather, nodular clasts consist of coarse (>250 micrometer), euhedral spar, and preserve regions—typically at the margins of the clasts—consisting of a mixture of chlorite, >100 micrometer dolomite rhombs, and pyrite. These regions also preserve substantial void space that is often associated with hydrocarbon accumulation (Fig. 5B).

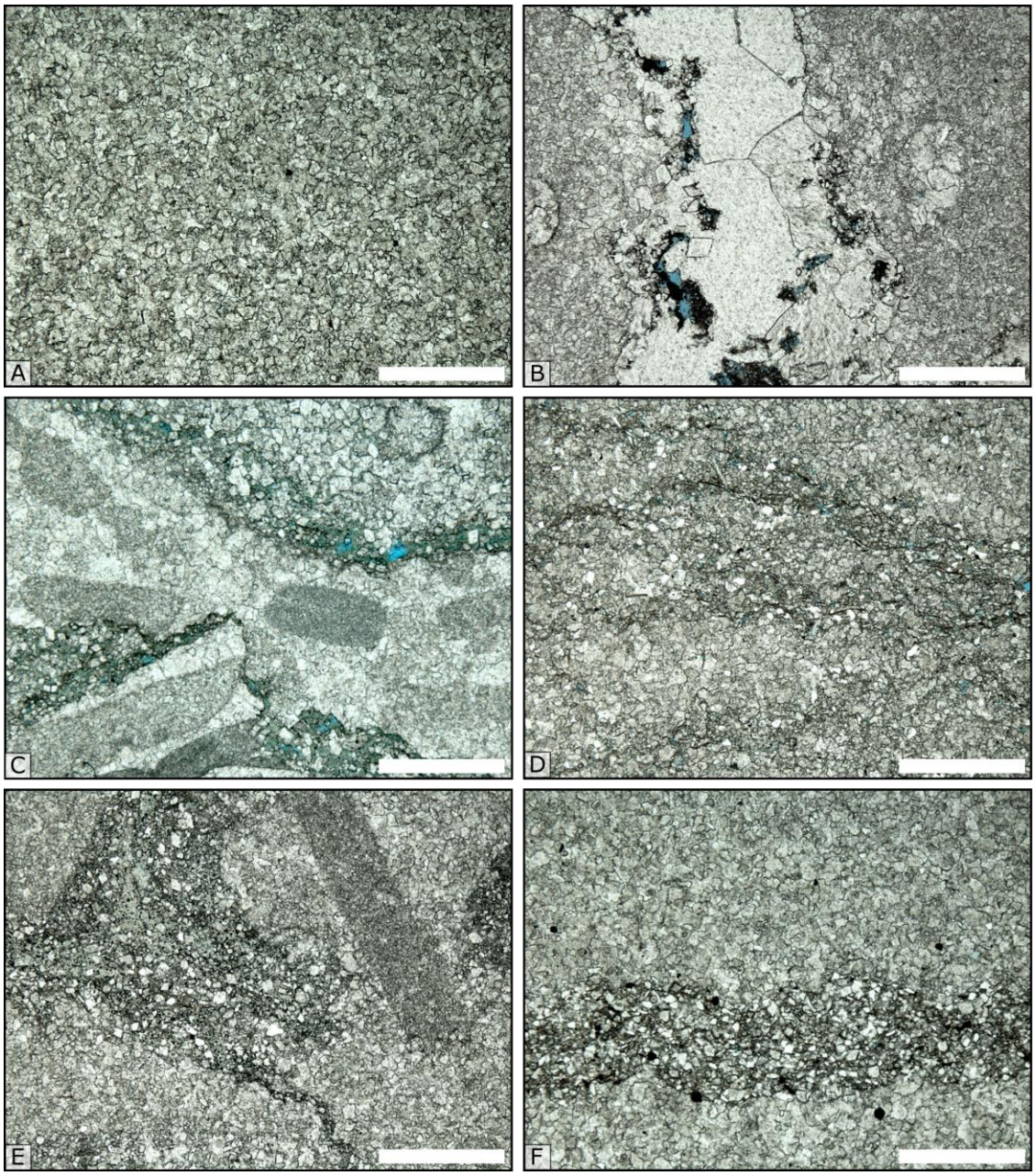

Figure 5. Petrography of samples. (A) Massive textures composed predominantly of uniformly coarse microspar with irregular intercrystalline boundaries. (B) Large crystals of calcite commonly replaced intraclasts within brecciated samples, and are commonly associated with oil inclusions. (C and D) Intraclastic breccias showing various degrees of recrystallization within of clasts; most consist of microsparitic limestone, or (as in D) are comprised of molar-tooth microspar (cf. Pollock et al., 2006). Depositional clay minerals and diagenetic chlorite are commonly found in stylolites. (E and F) Laminated and nodular fabrics, as with massive fabrics, consist of anhedral carbonate microspar, with individual nodules separated by irregular laminae that consist predominantly of clay, mica, quartz silt. Scale bar in each figure is 0.5 mm.

In addition to the most common fabrics described above, the R2 core also contains an additional piokilotopic fabric atypical of the general carbonate facies within the Atar Group (Kah et al., 2012; Gilleaudeau and Kah, 2013). This fabric occurs exclusively within clay-dominated facies in close stratigraphic proximity to bright white carbonate beds and consists of cm-thick cross-laminated ripples with mm-thick clay drapes (Fig 6A). Under crossed polarization, these rippled features are revealed to consist of quartz silt, and minor mica, encased within poikilotopic calcite (Fig. 6B). Critically, higher magnification shows that detrital siliciclastic components do not contact each other (Fig. 6C), implying the earlier presence of an additional detrital component that has now been entirely replaced by poikilotopic calcite.

Associated Mineral Phases

As noted above, non-carbonate phases associated with bright white carbonate beds are dominated by quartz, biotite mica, chlorite, clay minerals, and pyrite. Chlorite (Fig. 7A, B) is present in up to 35% of the R1 core samples, but rarely makes up more than 15% of any single sample, except where it is concentrated along stylolites. In most occurrences, chlorite is associated with non-luminescent euhedral dolomite, indicating a ferroan composition (Sommer, 1972; Machel and Burton, 1991; Savard et al., 1995). Pyrite is rare in most samples but is most commonly associated with bright white limestone facies in the R2 and F4 core samples. In R2 samples, pyrite occurs only in trace abundances, predominantly as small (<25 μm diameter) euhedral crystals, or clusters of crystals, associated with secondary chlorite and dolomite phases. In F4 core samples, which have undergone interaction with hydrothermal fluids, pyrite abundance can be locally much greater (up to 7% of several samples), and occurs as both euhedral crystals >3 mm diameter that occur in association with fluid pathways (i.e. interface between laminae, or within cross-cutting veins (Fig. 7C), and euhedral crystals <250 μm diameter disseminated through the matrix of intraclastic breccia phases (Fig. 7D).

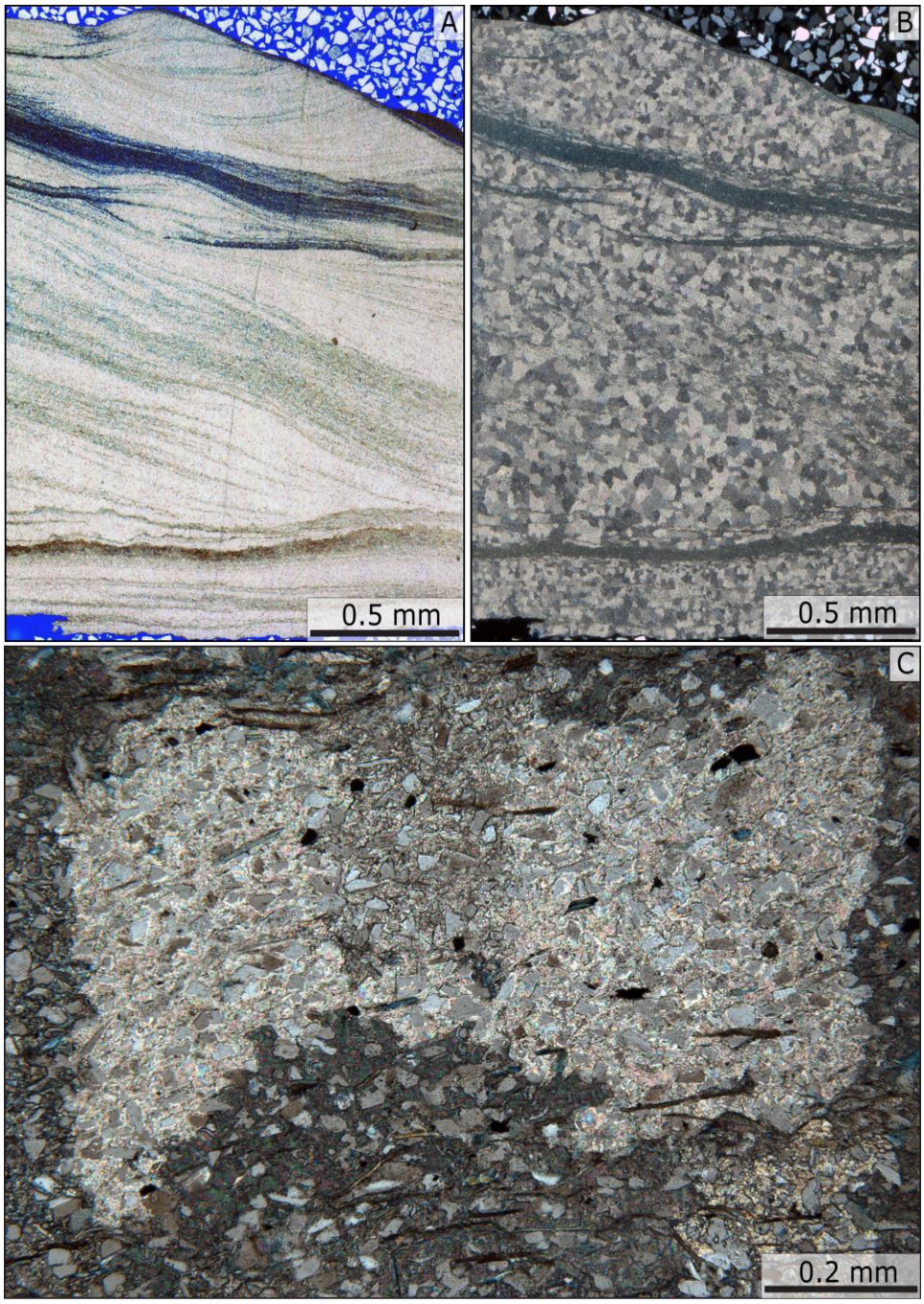

Figure 6. Cross-bedded quartz silt. (A) Rarely, cross laminated quartz silt is preserved in association with hypothesized calcitized evaporite facies. Here shown under transmitted, plane light, cross lamination is highlighted by the presence of clay drapes. (B) Under crossed polarization, cross-bedded intervals are shown to consist predominantly of poikilotopic calcite. (C) At higher magnification, quartz silt and biotite grains are clearly suspended within piokilotopic calcite.

Cathodoluminescence Petrography

Potential evaporite samples from the Atar Group luminesce across a spectrum from yellow-orange to red-orange. The majority of the samples display a matrix with an irregular and patchy texture consisting of large, subtly zoned crystals where dark calcite crystals are outlined by a brighter orange rim (Figure 8A and B). Secondary dolomite crystals appear as darker rhombic crystals dispersed throughout samples. Nodules that are found in samples with nodular fabric display this same texture with stringers of dark, iron-rich clay typically outlining individual nodules. Clastic breccias also display an irregular and patchy matrix, as well as various types of clasts, including bright orange, fine-grained clasts, clasts composed of molartooth cement, and clasts occasionally containing zoned crystals dispersed throughout the samples. Clasts composed of crystals >250 μm, commonly containing or outlined by darker clay components are the most frequently observed, and are commonly associated secondary dolomite (Figure 8C).

Relative abundances of manganese, rare earth elements, and iron are responsible for the luminescence characteristics exhibited by carbonates (Boggs and Krinsley, 2003). Brighter orange hues indicate a manganese-rich composition while darker reds represent an iron-rich or manganese depleted composition (Boggs and Krinsley, 2006). The irregular and patchy texture and various hues of orange suggest that either the diagenetic fluid composition evolved over time or that multiple diagenetic fluids are responsible for the calcitization process (Machel, 2000; Boggs and Krinsley, 2006). Darker clays and secondary dolomite are evidence of alteration after replacement. In addition to a general patchy texture, cathodoluminescence analyses also show small clusters of cubes (Goodman and Kah, 2004). Unlike primary fabrics that show large interlocking crystals with various shades of luminescence cubic morphologies are only moderately luminescent and show no evidence of zoning (Fig. 8D), interpreted to be polymorphs of former halite.

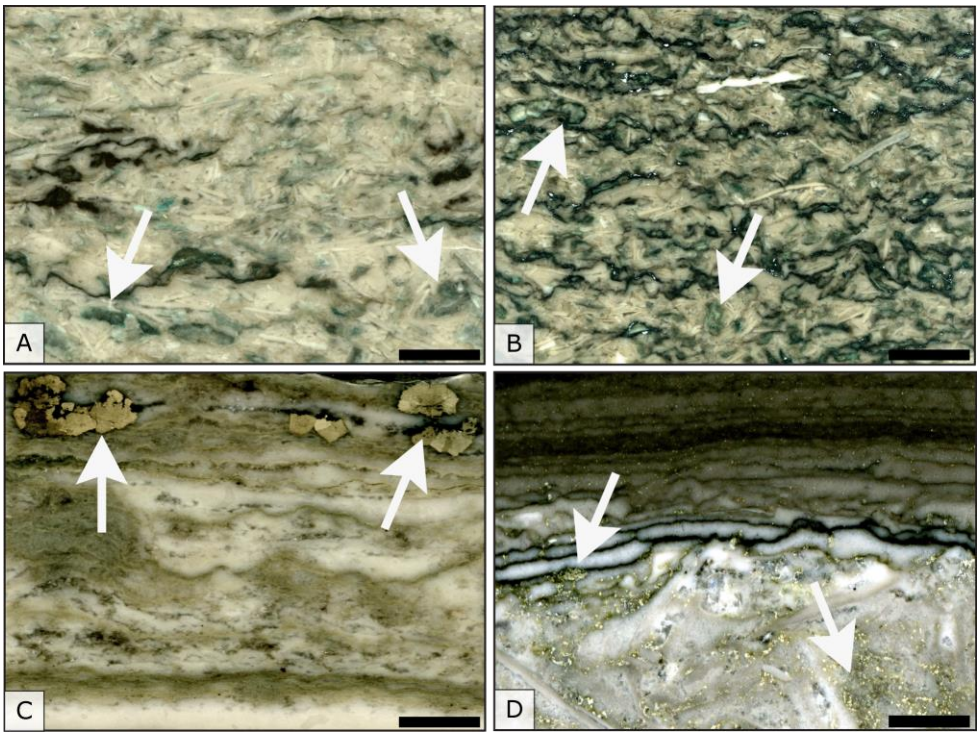

Figure 7. Chlorite is a common mineral phase associated with the Atar Group samples hypothesized to contain calcitized evaporites. (A) Chlorite commonly replaces clasts within intraclastic breccias, or occurs as diffuse concentrations along stylolites. (B) Samples containing more than 15% chlorite are always associated with abundant stylolitization. (C) Pyrite clusters within samples in the northern part of the basin. (D) Pyrite occurs most commonly in associated with chlorite and dolomite replaced clasts, and more rarely in discrete mineralized veins and regions (as in C), and disseminated throughout sample (as in D).

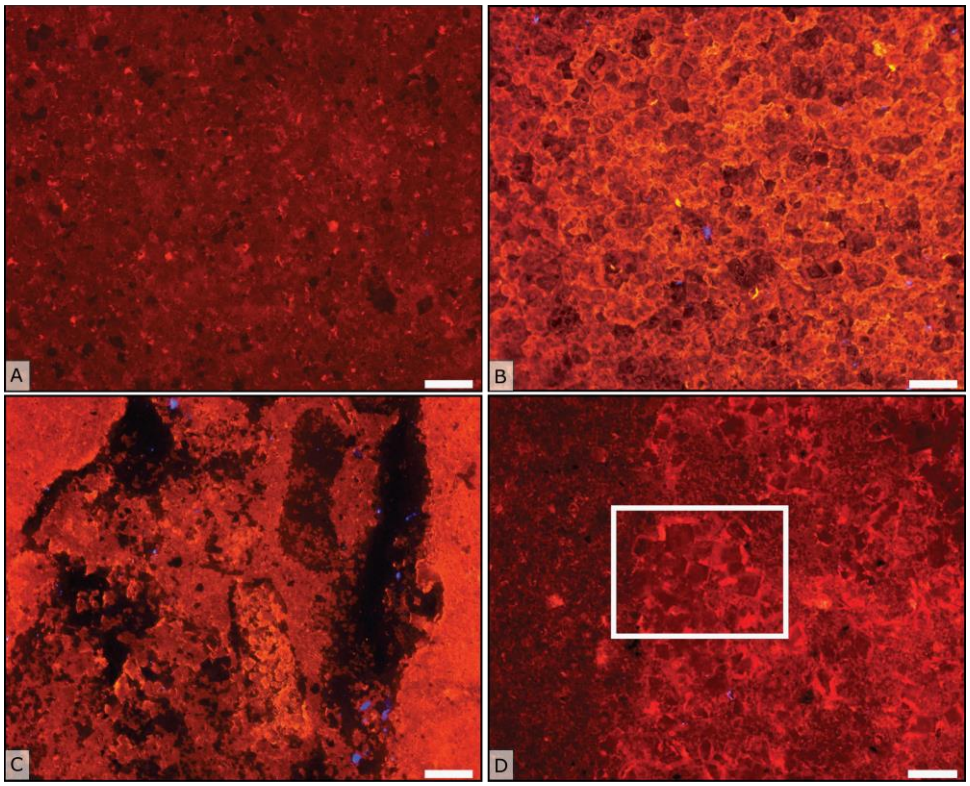

Figure 8. Atar Group carbonates luminesce various shades of orange under cathodoluminesence intraclastic breccias (A and B) contain various types of clasts, and the differences are noticeable under CL. (A) Clasts are generally outlined by a dark, almost black color. A clast of molartooth cement is found in the top left hand corner; while other clasts appear patchy and have darker rhombs within them, (B) other samples contain clasts comprised of other clasts with an irregular appearance. Larger crystals within the clasts display evidence of alteration (look choppy?). Massive (C) and nodular fabrics are similar under CL, both contain relatively uniform, and speckled coloration. Clay can be seen interspersed within nodular fabrics. Rare, clusters of uniform cubic crystals (D) are seen within these samples.

Scanning Electron Microscopy Analysis

Scanning electron microscopy was used in an attempt to relate relict fabrics within the Atar Group carbonates to evaporite precipitation by examination of mineralogic relationships and the identification of patterns in trace element abundance within fabric elements. The majority of these samples, with massive, nodular, and breccia fabrics have an irregular, patchy texture (Fig. 9A, B), and the overall primary texture appears to have been lost which suggests that replacement occurred rapidly which produced larger crystals. Elemental distribution maps generated via energy dispersive spectroscopy (EDS) indicate that the matrix of these samples is relatively uniform, typically Ca- or Mg –rich (Figure 9B, F, and H). Mg- and Al-rich clay phases can also be seen with SEM (Figure 9D and H); in clastic breccia samples, clasts are commonly outlined with this phase (Figure 9H).

Accessory minerals make up a minor part of these carbonate rocks. The most commonly observed accessory mineral was pyrite; however barite also occurs within the samples. When pyrite is present, it is typically disseminated throughout the sample. Barite was generally associated with styolites and clays. Bitumen or oil inclusions were also seen filling void spaces.

Interpretation of Macro- and Meso-scale Fabrics

Evidence for a Precursor Mineralogical Phase

At the outcrop scale, discrete bright white carbonate beds within units I-6 (Oued Tariofet) and I-7 (Tawaz) contrast sharply with surrounding orange-weathering carbonate rock (cf. Fig. 3), massive to nodular fabrics, and a high degree of stylolitization, which is not apparent in surrounding carbonate strata. Additionally, these beds commonly show evidence of subaerial exposure, epikarst, and collapse. Core samples from units I-6 (Gouamir Formation) and I-7 (Tenoumer Formation) are marked, similarly, by their bright white color, massive to nodular fabrics, and high degree of stylolitization. In addition to outcrop samples, core samples also contain abundant intraformational breccias, and are associated with both chlorite and pyrite phases. Combined, differences in color, degree of stylolitization, and presence of dissolution and collapse features suggest the existence of a primary depositional phase that was soluble relative to surrounding carbonate facies.

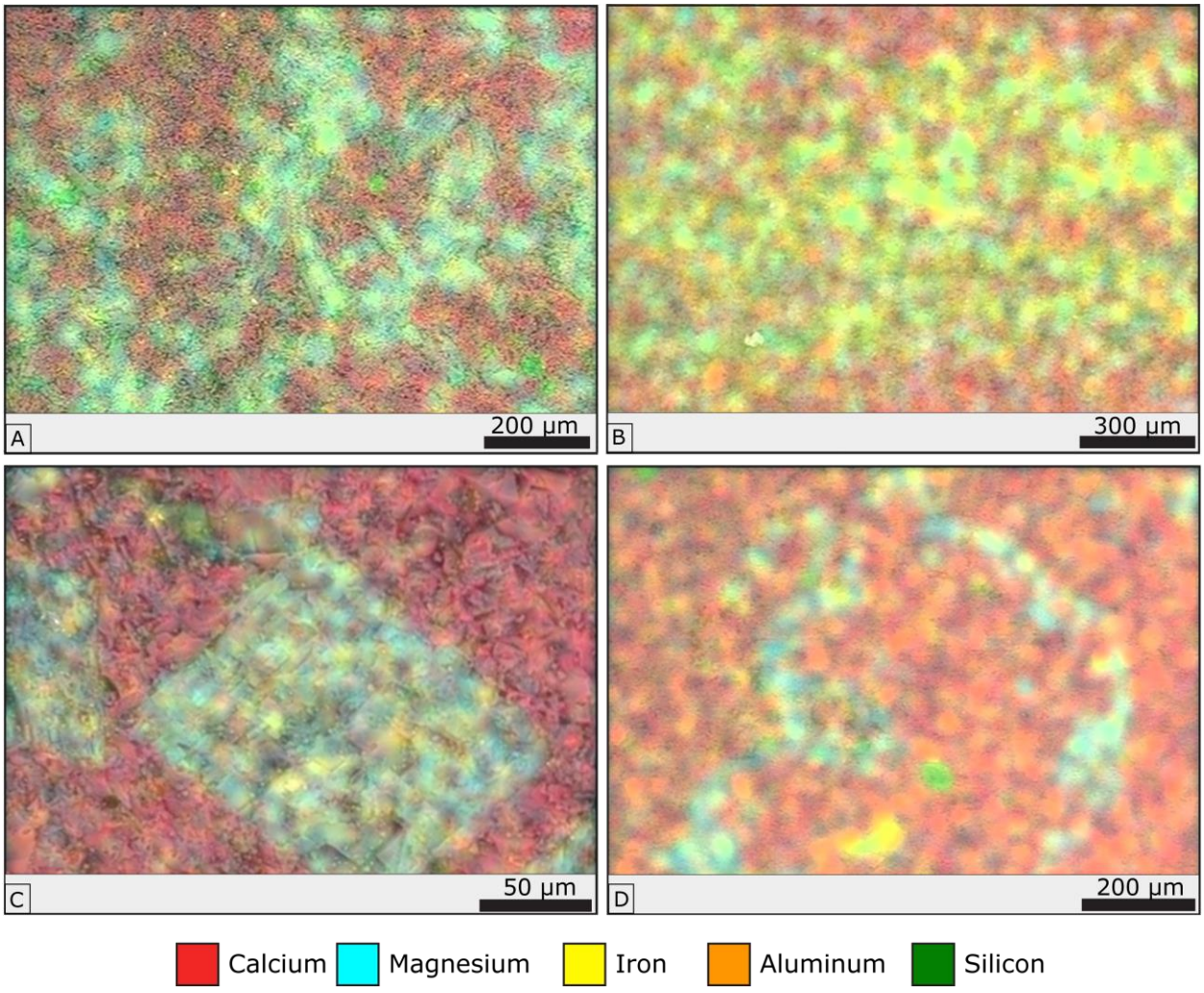

Figure 9. Scanning electron microscopy reveals an irregular texture, generally appearing patchy or grainy. According to elemental maps, this texture may be the result of mineralogic differences (A and B). Rhombic shapes, slightly darker in color, can be seen sporadically within the Atar Group carbonate samples (C), and are identified as dolomite using elemental mapping. In intraclastic breccia samples, clasts are commonly outlined by smooth, darker gray area (D) composed of Mg, Fe, Al, and Si.

Stylolites

Stylolites are generally uncommon in carbonate rocks of the Atar Group; however, the frequency and concentration of stylolites is substantially higher within the samples identified as Atar Group evaporites. Pressure dissolution that results in stylolitization is typically associated with burial (Park and Schot, 1968). Within carbonate rocks, stylolitization typically forms at burial depths ≥ 0.5–1.0 km (Bathurst, 1980); although incipient stylolitization has been documented in carbonate rocks at depths as low as 90 m (Schlanger, 1964). A variety of factors, such as water chemistry and the presence of clay minerals and organic matter, may promote stylolitization regardless of depth (Alsharhan and Sadd, 2000). Stylolites have also been described in evaporite deposits like gypsum and halite although they are typically less common in evaporite beds (Warren, 2006), because the higher solubility promotes wholesale dissolution or replacement. Additionally, stylolites that form within evaporite beds may not necessarily result from burial (Warren, 2006). Stylolites form in gypsum soon after deposition (Jaworska and Nowak, 2013), but are more scarce in anhydrite deposits as a result of porosity and permeability loss during the transformation of gypsum to anhydrite (Warren, 2006) which occurs at shallow depths and at temperatures above 50° C (Warren, 2006; Jaworska and Nowak, 2013).

Sedimentary rocks of the Proterozoic Atar Group have been buried to depths of 2.5–3.0 km, reaching maximum burial temperatures of 100°C (Girard et al., 1989) and have not experienced regional metamorphism (Rooney et al., 2010). The general absence of stylolites within the Atar Group carbonate rocks suggest that burial fluids were largely saturated with respect to the host limestone. In this scenario, stylolites within samples hypothesized to be evaporites, are best explained by incomplete calcitization prior to burial and the dissolution of a more soluble (evaporite) phase during (potentially shallow) burial diagenesis.

Microscale Support for a Gypsum Precursor

Although macro- and meso-scale textures described here are consistent with evaporite deposition (c.f. San-Rubio et al., 2001; Warren, 2001; Melezhik, 2005), ancient evaporite deposits are, commonly dominated by secondary textures reflecting the highly reactive nature of evaporite minerals (Warren, 2006). The high solubility of evaporite minerals results in repeated dissolution and precipitation, and much of the ambiguity regarding the distribution of ancient evaporites derives from their notoriously poor preservation potential (Spencer and Lowenstien, 1990; Scholle

et al., 1992; Ulmer-Scholle and Scholle, 1994; Schreiber and El Tabakha, 2000; Sanz-Rubio et al., 2001; Kendall, 2001; Brasier et al., 2011).

Microscale observations, however, provide additional evidence for an evaporitic precursor for bright white carbonate beds within the Atar Group. Petrographically, most samples lack evidence of primary fabrics, indicating nearly complete overprinting during postdepositional recrystallization. Several petrographic features, however, provide additional evidence for primary depositional minerals. First, preservation of cross-laminated quartz silt and biotite are preserved within poikilotopic calcite. The absence of grain support between detrital components indicates an original presence of an additional soluble detrital phase, such as gypsum (or anhydrite), which has been replaced by poikilotopic calcite (cf. Smosna, 1983; Smoot and Lowenstein, 1991; Warren, 2006).

Similarly, although intraformational breccias contain multiple different preservational styles,only a single clast type is characterized by coarse euhedral spar, and is associated with secondary porosity development, chlorite precipitation, euhedral dolomite, and pyrite. Differences in clast preservational style suggest the potential of a variety of original depositional mineralogies. Replacement of intraclasts by coarse spar, in particular, indicate a highly soluble primary phase, while associated pyrite suggest a primary, sulfur-bearing phase. Mg-rich clay minerals such as sepiolite and stevensite commonly co-precipitate with gypsum (Meunier, 2010), with sepiolite dominant in environments conducive to the co-precipitation of carbonate and gypsum (Meunier, 2010). These depositional phases can then transform to chlorite when exposed to low temperatures (~100 °C) as depositional clay minerals interact with Mg-rich diagenetic fluids derived from evaporite dissolution (Hillier, 1993). Chlorite is commonly associated with evaporite deposits and is present in the Atar Group calcitized evaporites. Additionally, the potential presence of Mg-rich brines is also evidenced by the association of chlorite and euhedral dolomite rhombs.

Finally, massive fabrics have been shown under cathodoluminescence to contain rare clusters of cubic crystals. The uniform luminescence of these features, which contrasts with zoned fabrics of the matrix component, suggests dissolution of a precursor phase that had greater solubility than the surrounding matrix, and was therefore dissolved completely, rather than undergoing incremental dissolution and reprecipitation. In this case, the cubic morphology suggest the potential for primary halite, which would be consistent with co-precipitation of a primary gypsum phase (Spencer and Lowenstein, 1990; Ulmer-Scholle and Scholle, 1994; Schreiber and El Tabakh, 2000; Warren, 2006).

Support for an Evaporitic Precursor

Deposition as gypsum provides an intriguing possibility for the origin of bright white limestone beds in the Atar Group. Environments in which evaporite minerals form include sabkhas, salinas, and other marine and terrestrial environments that experience extensive evaporation (Kendall, 1984; Rosen, 1994; Warren, 1996, 2006). In these environments, precipitation occurs as the solution reaches and exceeds supersaturation at the brine surface, sediment-brine interface, or interstitially within the sediment (Kendall, 1984). In modern marine systems, evaporite deposits are composed of various combinations of calcite, gypsum and anhydrite, halite, and potash salts (Warren, 2006, 2010), with gypsum precipitation occurring predominantly after calcium carbonate precipitation ceases and once the salinity of the brine has reached between ~150‰ and ~320‰ (Rouchy and Monty, 2000; Babel, 2004).

Within evaporite deposits, lithologic textures reflect the origin of mineral precipitation either within the brine column or within the sedimentary substrate. Laminated gypsum deposits and alternation of laminae of a different composition—usually gypsum interbedded with calcite, halite, detrital components, or organic matter—commonly reflect subaqueous deposition (Schreiber and El Tabakh, 2000; Tucker, 2001). By contrast, sabkha environments are dominated by precipitation that takes place either within subaerially exposed sediment or in very shallow saline pans. In these environments, gypsum occurs either as individual lenticular crystals or clusters of crystals that grow displacively within phreatic and capillary groundwater zones (Kasprzyk and Ort□, 1998; Schreiber and El Tabakh, 2000; Tucker, 2001), or as laterally coherent laminae reflecting precipitation within water column or at the brine-air interface (Warren, 2006). Often in these environments, gypsum dehydrates during arid periods to form anhydrite, only to be rehydrated during wet periods. Volume changes associated with dehydration and rehydration result in formation of enterolithic and nodular morphologies that typify sabkha environments (Hardie and Eugester, 1970; Dean et al., 1975; Warren and Kendall, 1985; Shearman, 1987; Hussian and Warren, 1989; Warren, 2000, 2006, 2010; Aleali et al., 2013). Marine sabkha accumulations can also be identified by the presence of evaporites as capping rocks within marine depositional cycles, and by common occurrence of wind or water-cut surfaces, and dissolution (epikarst formation) during subaerial exposure (Grunau, 1987; Schreiber et al., 1976; Sarg, 2001; Pomoni-Papioannou and Karakitsios, 2002; Warren, 2006).

Geochemistry of Potential Calcitized Evaporites

A combination of macro- to micro-scale fabric evidence is consistent with the hypothesis that bright white carbonate beds within the Atar Group may represent the presence of calcitized evaporite deposits. To further test this hypothesis, I examined the bulk isotopic and elemental compositions of 73 samples (62 samples from the R1 core, and 11 samples from the R2 core), 36 of these samples were from the potential evaporite phases. The remaining samples were from the associated carbonate phases (Appendix 1). Geochemical results are compiled in Table 1, illustrated in Figures 10 and 11, and summarized below.

Carbon isotope compositions of whole rock samples range from -0.02 to -1.33‰ with an average value of -0.45±0.3‰ VPDB (N=36). Similarly, oxygen isotope compositions range from -6.8 to -11.71‰ with an average value of -8.1±1.1‰ VPDB (N=36) (Fig. 10). Measured elemental compositions include Mg/Ca ratio (0 to 0.19, averaging 0.03±0.05), which was used to determine variation in the composition of current calcite phases; concentrations of Sr (59 to 1805 ppm, averaging 516±390 ppm), Mn (67 to 5875 ppm, averaging 850±1217 ppm), and Fe (832 to 55,208 ppm, averaging 8050±9013 ppm) to investigate diagenetic trends; and concentrations of Na (107 to 17,147 ppm, averaging 1905±2946 ppm), K (47 to 13,090 ppm, averaging 1097±2246 ppm) and SO_4 (75 to 720 ppm, averaging 317±163 ppm) to determine potential for enhanced salinity during deposition or diagenesis.

Interpretation of Geochemical Results

Carbon and Oxygen Isotope Compositions

Isotope composition of marine carbonate phases can aid in the reconstruction of both parent fluid composition and the composition of diagenetic fluids (Brand and Veizer, 1980; Banner and Hanson, 1990; Marshall, 1992; Brand, 2004), with observed variation in isotopic composition reflecting the extent of water–rock interaction on a primary mineral during the diagenetic process (Banner and Hanson, 1990). Although diagenesis is capable of overprinting primary isotope compositions, the composition of the diagenetic product can also preserve trends that reflect variable water–rock interaction during diagenesis. For example, because diagenetic fluids are commonly depleted in carbon (Kaufman et al., 1991; Bartley et al., 2007), carbon isotope signatures of carbonate rocks are not strongly affected by water-rock interaction and remain buffered to the composition of the

originally precipitated carbonate phase (cf. Kaufman et al., 1991; Frank et al., 2003; Bartley et al., 2007).

Diagenetic contributions to the carbon isotope composition of marine carbonates most often reflect either *in situ* decomposition of organic components during early lithification (cf. Kah et al., 1999; Kah et al., 2012; Gilleaudeau and Kah, 2013b), or the thermal decomposition of organic components during burial diagenesis (McKirdy and Powell, 1974; Heydari and Moore, 1989; Des Marais, 2001; Lehmann et al., 2002). By contrast, oxygen isotope compositions are strongly affected by water-rock interaction, wherein precipitation from evaporative waters or interaction with a saltwater brine results in enrichment in ^{18}O (Veizer, 1983; Kah, 2000), diagenesis in the presence of fresh or meteoric water result in generally small (commonly <4-6‰; Bowen and Wilkinson, 2002) depletion with respect to ^{18}O, and exchange with hydrothermal fluids during burial result in carbonate compositions strongly depleted with respect to ^{18}O (Morse and Mackenzie, 1990; Brenneke, 2007; Bojanoswki et al., 2014).

Oxygen isotope values of petrographically well preserved carbonate rock samples from the Atar Group range from approximately −6 to −9‰ (Kah et al., 2012; Gilleaudeau and Kah, 2013). Although there remains considerable controversy regarding the oxygen isotope composition of ancient marine systems (cf. Walker and Lohmann, 1989; Kah, 2000; Kasting et al., 2006; Jaffrés et al., 2007), interpretation of evaporitic trends showing an increase of ~6‰ in samples from open marine environments to those at gypsum saturation (Sofer and Gat, 1975; Kah, 2000) suggest that isotopically light values may be non-diagenetic origin.

Table 1. Isotopic and elemental results from the R1 and R2 core for the samples hypothesized to represent calcitized evaporite lithologies.

Sample Name	$\delta^{13}C$ (‰ VPDB)	$\delta^{18}O$ (‰ VPDB)	Mg/Ca ratio	Na [ppm]	K [ppm]	Sr [ppm]	Fe [ppm]	Mn [ppm]	SO_4 [ppm]
R1-D127	-0.63	-7.16	0.011	160	161	324	1638	250	324
R1-D128	-0.61	-7.04	0.026	286	227	533	2726	257	368
R1-D129	-0.59	-7.49	0.006	5018	117	282	1243	223	75
R1-D130	-0.64	-7.11	0.005	816	252	281	1056	269	177
R1-D131	-0.41	-7.05	0.081	1066	158	170	5470	415	686
R1-D132	-	-	0.029	725	251	186	3007	260	167
R1-D133	-0.16	-7.64	0.028	477	355	234	3565	258	418
R1-D136	-0.35	-8.38	0.008	8268	158	659	1865	204	386
R1-D137	-0.46	-7.92	0.027	5575	130	230	3263	246	196
R1-D138	-0.41	-7.43	0.008	1039	201	432	1740	209	386
R1-D139	-0.45	-7.8	0.045	1093	129	263	5279	329	170
R1-D140	-0.55	-7.67	0.005	788	130	215	1418	234	-
R1-D141	-0.34	-8.5	0.045	153	111	261	5439	334	90
R1-D142	-0.47	-7.43	0.004	435	131	253	1360	284	411
R1-D143	-0.34	-8.45	0.010	107	136	262	2216	295	100
R1-D144	-0.28	-8.17	0.015	705	152	289	3730	387	109
R1-D148	-0.29	-7.16	0.006	1157	768	430	4146	530	337
R1-D149	-0.26	-6.8	0.004	4199	326	289	2967	439	409
R1-D150	-0.25	-7.5	0.024	323	472	327	6642	619	259
R1-D151	-0.21	-7.57	0.005	6987	466	464	3421	426	488
R1-D152	-0.02	-8.16	0.016	1826	127	431	4651	497	470
R1-D154	-0.25	-7.93	0.007	815	225	436	3679	489	721
R1-D155	-0.18	-7.72	0.007	502	569	537	4045	493	502
R1-D156	-0.31	-7.27	0.041	1383	214	304	10379	808	110
R1-D157	-0.43	-6.86	0.006	261	498	264	3150	490	529
R1-D158	-0.27	-7.31	0.023	251	328	309	6511	575	494
R1-D159	-	-	0.029	6622	218	325	8289	658	213
R1-D161	-1.33	-11.71	0.048	456	201	274	11872	736	317
R1-D162	-0.29	-7.47	0.031	840	245	342	8628	584	446
R1-D165	-0.09	-8.42	0.013	817	427	150	5087	661	287
R2-D2-12	-0.84	-10.16	0.008	1108	95	217	832	67	83
R2-D2-13	-0.44	-7.97	0.195	794	137	78	8462	243	393
R2-D2-2	-0.68	-8.43	0.272	481	105	59	24190	601	356
R2-D2-3	-0.89	-9.5	0.055	262	47	81	5888	196	159
R2-D2-4	-0.98	-9.21	0.049	9776	212	113	4643	163	302
R2-D2-5	-0.73	-8.27	0.069	711	156	104	4771	166	262
R2-D2-6	-	-	0.040	595	167	177	2710	112	124
R2-D2-7	-0.38	-10.08	0.129	259	61	80	5852	184	240

Figure 10. Diagenetic indicators in the Atar Group carbonates. (A) Carbon and oxygen isotope composition of formations within the Atar Group. The black circles and squares represent the potential evaporite phases while the other markers represent data from the associated carbonate formations. Potential evaporite phases, located in the Gouamir Formation, plot within the same region as marine carbonates within the surrounding formations. The R2 core shows slightly lighter oxygen isotope values. The inset shows isotope data for the potential evaporites, with low carbon isotopes and the majority of the oxygen isotopes ranging from -7 to -10 per mil. (B) Potential evaporite phases are depleted in strontium relative to the associated carbonates. (C) Potential evaporite phases also contain low concentrations of iron and manganese relative to many of the associated formations, suggeting diagenetic recrystallization primarily in oxic environments. An insert shows the widespread range within the potential evaporite phases.

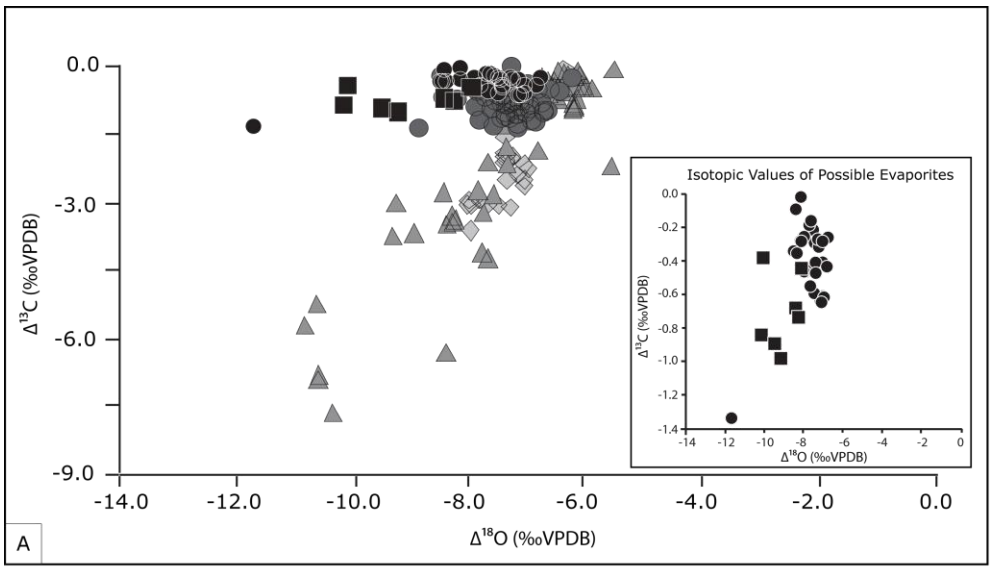
0.0
-3.0
-6.0
-9.0
Δ13C (‰VPDB)
-14.0
-12.0
-10.0
-8.0
-6.0
-4.0
-2.0
0.0
Δ18O (‰VPDB)
A
Isotopic Values of Possible Evaporites
0.0
-0.2
-0.4
-0.6
-0.8
-1.0
-1.2
-1.4
Δ13C (‰VPDB)
-14
-12
-10
-8
-6
-4
-2
0
Δ18O (‰VPDB)

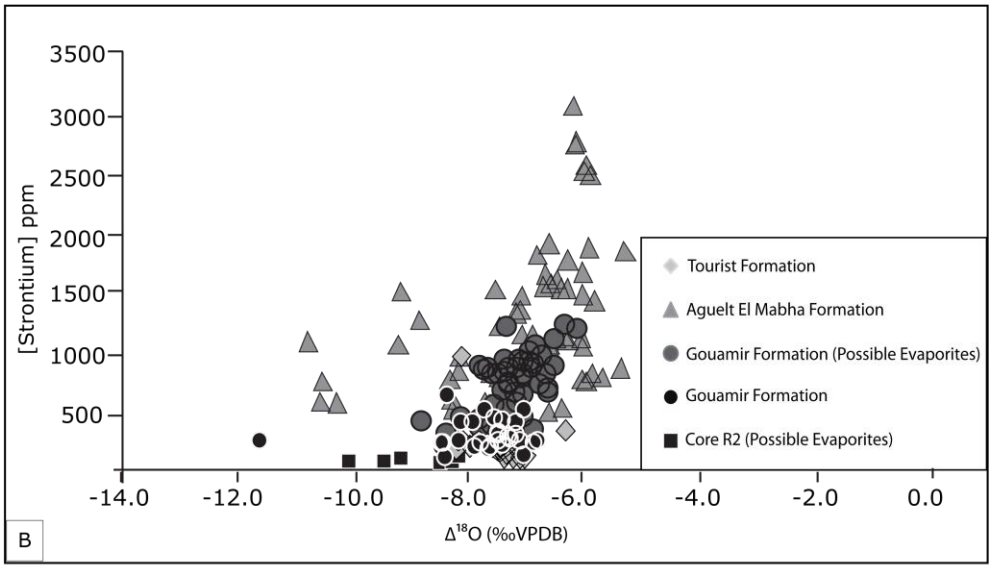
3500
3000
2500
2000
1500
1000
500
[Strontium] ppm
-14.0
-12.0
-10.0
-8.0
-6.0
-4.0
-2.0
0.0
Δ18O (‰VPDB)
B
Tourist Formation
Aguelt El Mabha Formation
Gouamir Formation (Possible Evaporites)
Gouamir Formation
Core R2 (Possible Evaporites)

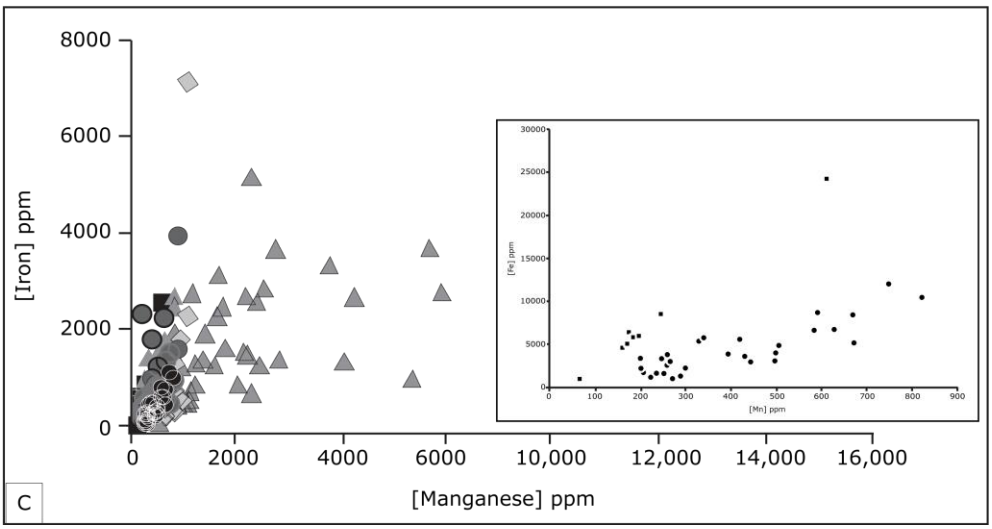
8000
6000
4000
2000
0
[Iron] ppm
0
2000
4000
6000
10,000
12,000
14,000
16,000
[Manganese] ppm
C
30000
25000
20000
15000
10000
5000
0
[Fe] ppm
0
100
200
300
400
500
600
700
800
900
[Mn] ppm

Figure 10 shows the carbon and oxygen isotope composition of hypothesized calcitized evaporites of the Gouamir Formation (Unit I-6) in the R1 and R2 cores, plotted against marine carbonate strata of the R1 core (unpublished data, Appendix 1). Carbon isotope values typically vary by less than 1‰, consistent with their stratigraphic position near the top of the Gouamir Formation (cf. Gilleaudeau and Kah, 2013b). Carbon isotope variation in the other units represented in the R1 core is consistent with stratigraphic variation observed in the Atar Group throughout the Taoudeni Basin (Kah et al., 2012; Gilleaudeau and Kah, 2013b). Similarly, the oxygen isotope data of hypothesized calcitized evaporite facies (-6.8 to -11.71‰) are similar, at their heaviest to those recorded by most well-preserved, non-evaporitic carbonates from both the Atar Group (Kah et al., 2012; Gilleaudeau and Kah, 2013b) and Mesoproterozoic carbonate successions worldwide (Kah et al., 1999; Frank and Lyons, 2000; Kah, 2000; Frank et al., 2003; Bartley et al., 2007). Oxygen isotope compositions less than -9‰ may reflect diagenetic interaction with meteoric or mixed marine-meteoric fluids.

Combined, these data demonstrate that carbon and oxygen isotope compositions of potential calcitized evaporite facies are nearly indistinguishable from petrographically well-preserved marine carbonate lithologies within the same succession. Particularly, this facies does not preserve ^{18}O-enriched isotopic compositions that might be expected from facies deposited within evaporative marine environments. If these materials *were* originally deposited under evaporative marine conditions, current oxygen isotope compositions suggest that diagenesis must have occurred in the presence of fluids similar to that of the surrounding carbonate facies. Together, these data suggest that carbon and oxygen isotope compositions alone are insufficient to test the hypothesis that bright white carbonate beds within the Atar Group represent calcitized evaporite facies.

Trace Elements

Trace element incorporation into the carbonate lattice can provide an additional assessment of deposition and diagenesis. Elemental concentrations of Sr^{2+}, Mn^{2+}, and Fe^{2+}, for example, are typically used to assess both depositional environments and the degree of post-depositional alteration (Marshall, 1992), wherein recrystallization of the initial phase, under different degrees of water–rock interaction, will result in data that reflect a mixture between the primary rock composition and the composition of diagenetic mineral growth. Strontium concentration within marine carbonate rocks will reflect a combination of the strontium

concentration of marine systems, the lattice structure of the precipitating mineral (e.g., calcite versus aragonite), and secondary parameters such as the temperature and rate of precipitation (Lorens, 1981; Mucci and Morse, 1983; Carpenter et al., 1991; Carpenter and Lohmann, 1992). Strontium concentrations in petrographically well preserved marine limestone are typically <500 ppm, unless the original precipitate is aragonite, which can have Sr concentrations up to several 1000 ppm. Precipitation under evaporative conditions is typically reflected in the concentration of major and trace elements, such as strontium, over that of open marine waters (Kah et al., 2001; Horita et al 2002; Sanz-Rubio et al., 2001). During diagenesis, however, strontium is typically released from the crystal reflecting a combination of lower concentration of strontium that is common in fresh and meteoric waters, and the expulsion of strontium during recrystallization to a more stable carbonate phase (Brand and Veizer, 1980; Vahrenkamp and Swart, 1990). That strontium is typically expelled from the crystal lattice even during early diagenetic recrystallization in marine fluids makes strontium one of the most sensitive indicators of diagenetic recrystallization.

Similarly, manganese and iron incorporation into marine carbonate rocks are most often interpreted to reflect enriched during diagenesis in the presence of anoxic, burial fluids (Brand and Veizer, 1980; Banner and Hanson, 1990; Savard et al., 1995; Hemming et al., 1999), because the concentration of these elements in their divalent state is nearly zero in well-oxygenated marine and surface waters. Generally elevated concentrations of manganese and iron, however, in even petrographically well-preserved Proterozoic marine carbonate rocks, however, suggest that redox-stratification of the water column (Kah et al., 2012) and substrate pore waters (Kah et al., 1999; Gilleaudeau and Kah, 2013a, 2013b) resulted in enhanced biological cycling and availability of these elements for incorporation into marine carbonate rocks.

Figures 10B and C show the concentrations of Sr, Mn, and Fe in potential calcitized evaporite facies, plotted against marine carbonate strata of the R1 core (unpublished data, see Appendix 1). Strontium concentrations (Fig. 10B) are generally <500 ppm, consistent with those observed in open marine carbonate rocks of the deeper-water Touirist Formation, but are substantially lower than that observed in both shallow marine facies of the Aguelt el Mabha Formation, and marine carbonate facies of the Gouamir Formations (cf. Kah et al., 2012; Gilleaudeau and Kah, 2013a). The degree of recrystallization observed in potential calcitized evaporites, however, greatly exceeds that observed in surrounding carbonate rocks (cf. Kah et al., 2012;

Gilleaudeau and Kah, 2013a), suggesting the possibility that low strontium concentrations reflect post-depositional recrystallization, potentially as evaporites were exposed to less saline (marine or fresh water) brines. Whereas the high solubility of evaporite facies would enhance the potential for near-penecontemporaneous dissolution and recrystallization, the elevated carbonate saturation state of Proterozoic marine environments (Grotzinger, 1990; Kasting and Grotzinger, 1993; Bartley and Kah, 2004) would have resulted in much lower susceptibility of marine carbonate rocks to early diagenetic dissolution and recrystallization.

Similarly, the concentration of manganese and iron within hypothesized calcitized evaporite facies (Fig. 10C) are similar to that recorded in carbonate rocks of both the deeper-water Touirist Formation and the rest of the Gouamir Formation. These concentrations, however, are substantially lower than those measured in the carbonates of the Aguelt el Mabha formation, which has been interpreted to represent deposition under dysoxic, shallow-marine conditions that may have received a contribution from terrestrially sourced waters (Gilleaudeau and Kah, 2013b). In this case, relatively low manganese and iron concentrations in the hypothesized calcitized evaporite facies likely represent dissolution and recrystallization within distinctly oxic, well-circulating—and therefore potentially marine—fluids (Gilleaudeau and Kah, 2013a, 2013b).

Paleosalinity Indicators

As discussed above, both strontium concentration and oxygen isotope composition of hypothesized calcitized evaporites are ambiguous, and appear to reflect diagenetic recrystallization in fluids similar to that recorded in surrounding oxic, open marine strata. Data suggests that salinity of fluids can also accurately be portrayed using several other trace elements, such as the concentration of Na, K, and even SO_4, within of depositional or diagenetic phases (Staudt et al., 1993; Fritz and Katz, 1972; Land and Hoops, 1973; White, 1977; Veizer et al., 1977;1978;).

The most abundant cation in seawater is sodium (Land and Hoops, 1973), which has been shown to be an effective indicator of the paleosalinity of the both parent and diagenetic brines (Fritz and Katz, 1972; Veizer et al., 1977; Veizer et al., 1978). Experimental work of Veizer et al. (1977) further suggested that sodium could be used to indicate paleosalinity in ancient carbonates and also noted that redistribution of sodium through secondary diagenetic processes does not necessarily overprint the original sedimentary geochemistry. Modern, open marine waters contain approximately 11,154 ppm sodium (Spear et al., 2014). Although partition coefficients are not well established for sodium (Ishikawa and Ichikuni 1984; Wit et al., 2013), a combination of empirical

(Badiozamani, 1973; Veizer 1978) and experimental data suggests open-marine calcite typically contains 100-300 ppm sodium. Sodium incorporation appears to be very sensitive to crystal structure, however, with 1000-4000 ppm sodium more typical of aragonite and biogenic high-magnesian calcite (Land and Hoops, 1973; White, 1977).

Sodium concentrations in potential calcitized evaporites of the Atar Group (Fig. 11A) fall largely within the range of 107 to 1828 ppm, broadly consistent with that expected from marine low-magnesian calcite (i.e., their current mineralogy). A second subset of these samples have sodium concentrations that range from 4207 to 9790 ppm, substantially higher than the average concentration incorporated into a modern carbonate indicating sodium enrichment from either a primary phase of a diagenetic fluid. Differences between these two patterns may be the result of variable water–rock ratios during diagenesis. Variation in petrographic fabrics suggests that samples underwent variable amounts of recrystallization, likely resulting from a combination of different original mineralogy (i.e. calcite or gypsum), and different degrees of water-rock interaction. In this scenario, lower trace element incorporation may be the result of higher ratios of water–rock interaction capable of removing sodium from the system prior to recrystallization. Samples with strongly elevated concentrations may have experienced recrystallization at water–rock ratios (or fluid compositions) insufficient to fully remove sodium from the system. If this was the case, elevated Na concentrations may be interpreted to reflect primary mineral precipitation (gypsum ± halite) at elevated salinities.

Surrounding siliciclastics facies in the Atar Group are composed of quartz, kaolinite, illite, feldspar, and pyrite (Rooney et al., 2010); therefore, it is likely that diagenetic fluids were enriched in sodium and potassium as a result of leaching of these beds. Concentrations of sodium were plotted against concentrations of potassium within the Atar Group calcitized evaporites (Fig. 11). If the source of both cations was the same diagenetic fluid, trace elements would likely display a covariance. In this case, samples that are enriched in sodium are not the same samples that are enriched in potassium. Instead, low concentrations of both ions are present with a few exceptions elevated in sodium and depleted in potassium, which may indicate that the source of the potassium was not the same as the source of sodium. Decoupling of sodium and potassium is also seen stratigraphically in figure 11B as well. Samples with elevated concentrations of sodium occur within a thin interval of the Atar Group section; if these concentrations were the result a widespread diagenetic fluid, all of the samples should be elevated with respect to sodium. Only

seven samples have elevated concentrations and are interpreted to be preserved geochemistry of a former evaporative phase.

Much like sodium, potassium concentrations can also be used as an indicator of paleosalinty (Ishikawa and Ichikuni, 1984; Okumura and Kitano, 1986). Potassium is less straightforward as a paleosalinity indicator, however, because potassium contents are strongly associated with the presence of aluminosilicate minerals, and commonly show a strong correlation with the concentration of insoluble residue (Veizer et al., 1978). Modern, open marine waters contain approximately 400 ppm potassium. When weight percent insoluble residue is taken into account, potassium concentrations within open marine carbonate minerals are typically <100 ppm, with hypersaline carbonate phases ranging to several 100 ppm (Veizer et al., 1978). Partition coefficients for potassium incorporation into carbonate minerals, however, are poorly constrained (Ishikwana and Ichikuni, 1984; Okumura 1986; Veizer et al., 1978), and limited data suggests that co-precipitation of K may decrease with increased Na incorporation (Veizer et al., 1978).

According to SEM elemental distribution maps (Fig. 9), clay minerals within samples of potential calcitized evaporites from the Atar Group are dominated by iron and magnesium, and contain little sodium or potassium. Additionally, samples contained relatively little or no insoluble residue; the few samples that contained chlorite were still <15% non-carbonate phases. Most Atar Group samples (Fig. 12B) fall within the range of potassium concentrations expected from marine calcite. As with sodium, several samples contain potassium concentrations >750 ppm which may imply primary deposition under hypersaline conditions. Siliciclastic strata of the Atar Group, however, contain clays and other K-rich minerals like glauconite. K-Ar dating on these glacuonite yield ages substantially lower than those established by Re-Os dating and chemostratigraphy (Clauer, 1981). The disparity between these ages are believed to be the result of Ar loss during meteoric diagenesis (Clauer, 1982; Rooney et al., 2010; Kah et al., 2009), but may also represent mobility of potassium during burial diagenesis. At present, potassium mobility during diagenesis cannot be fully discounted as a source of potassium in these samples, although burial diagenesis is more likely to result in higher water-rock interaction and increased uniformity in the composition of samples. Substantially variable compositions preserved here is more consistent with variability in both original mineralogy and water-rock interaction.

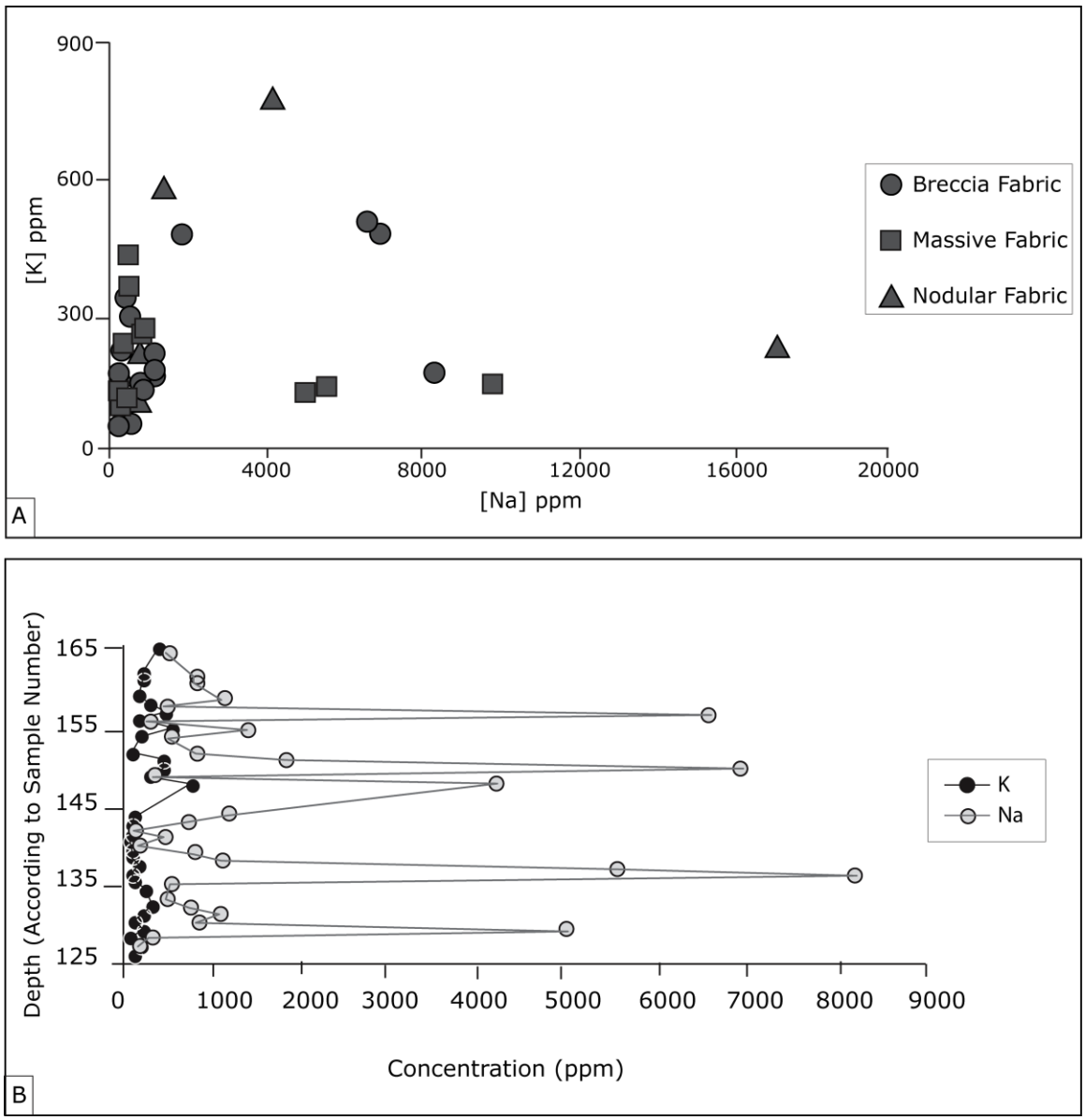

Figure 11. Sodium and potassium as paleosalinity indicators. (A) Sodium and potassium concentrations are decoupled with samples high in sodium and low in potassium and other samples high in potassium and low in sodium. (B) The decoupling is also seen with depth.

Figure 12. Trace elements that provide indication of paleosalinity. (A) Most calcitized evaporite facies record sodium concentrations between 100 ppm and 2000 ppm. Multiple samples however, record sodium concentrations substantially higher than that expected from modern carbonate minerals (cf. Viezer et al., 1978; Wit et al., 2013) indicating the potential for original hyersaline depositional conditions (gypsum ± halite). (B) Potassium concentrations within calcitized evaporite facies largely fall between 40 ppm and 300 ppm. Several samples, however, record potassium concentrations above those expected in modern carbonates (Veizer et al., 1978), suggesting incomplete replacement of a potassium-rich phase. (C) Similarly, most calcitized evaporite samples contain between 100 ppm to 500 ppm of sulfate. Values <200 ppm are expected Proterozoic carbonates (Kah et al., 2004; Gellatly and Lyons, 2005), also indicating potential retention of chemistry associated with a primary hypersaline depositional phase.

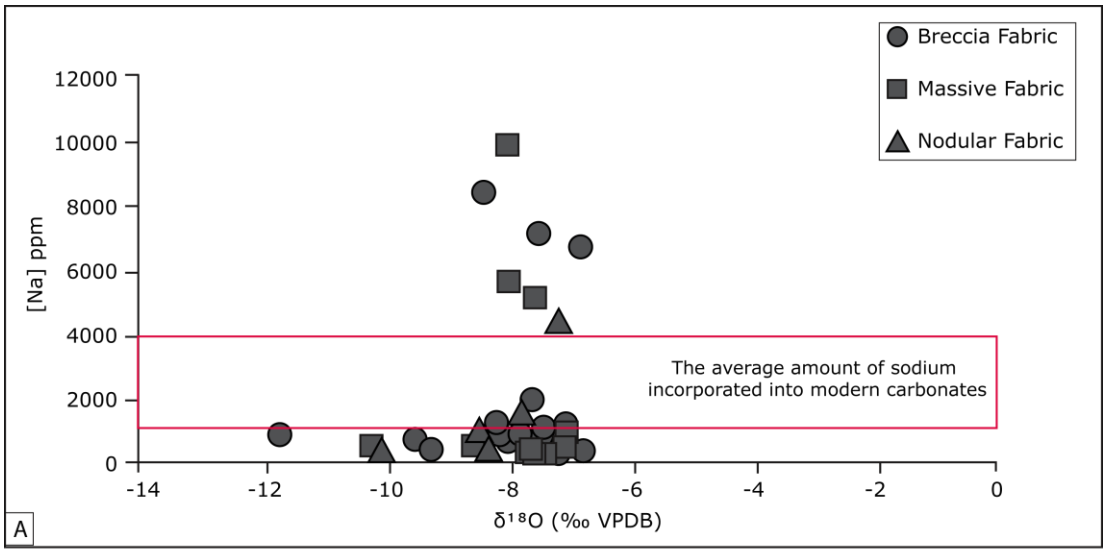
Breccia Fabric
Massive Fabric
Nodular Fabric
12000
10000
8000
6000
4000
2000
0
[Na] ppm
The average amount of sodium incorporated into modern carbonates
-14
-12
-10
-8
-6
-4
-2
0
δ¹⁸O (‰ VPDB)
A

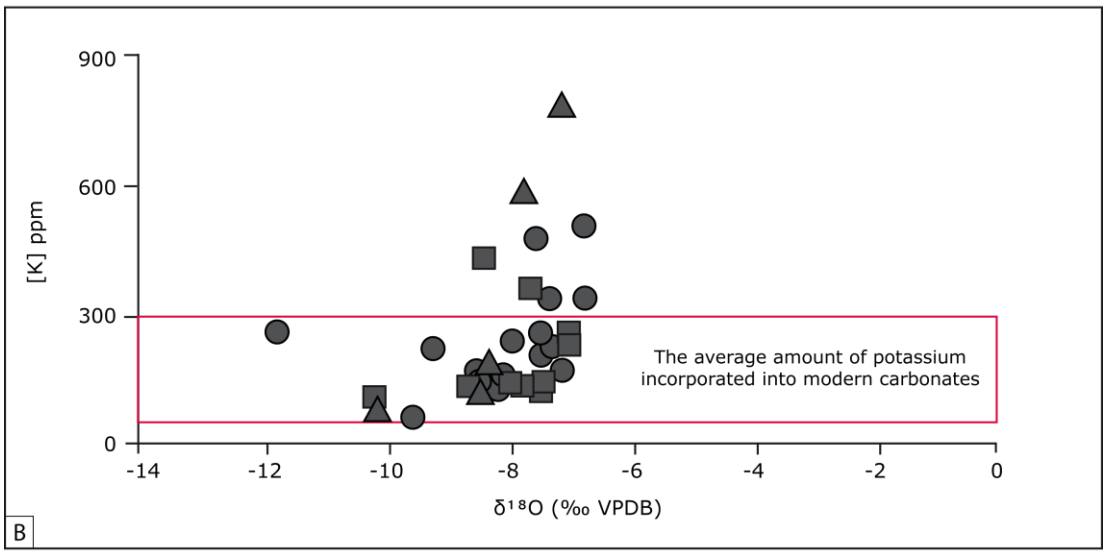
900
600
300
0
[K] ppm
The average amount of potassium incorporated into modern carbonates
-14
-12
-10
-8
-6
-4
-2
0
δ¹⁸O (‰ VPDB)
B

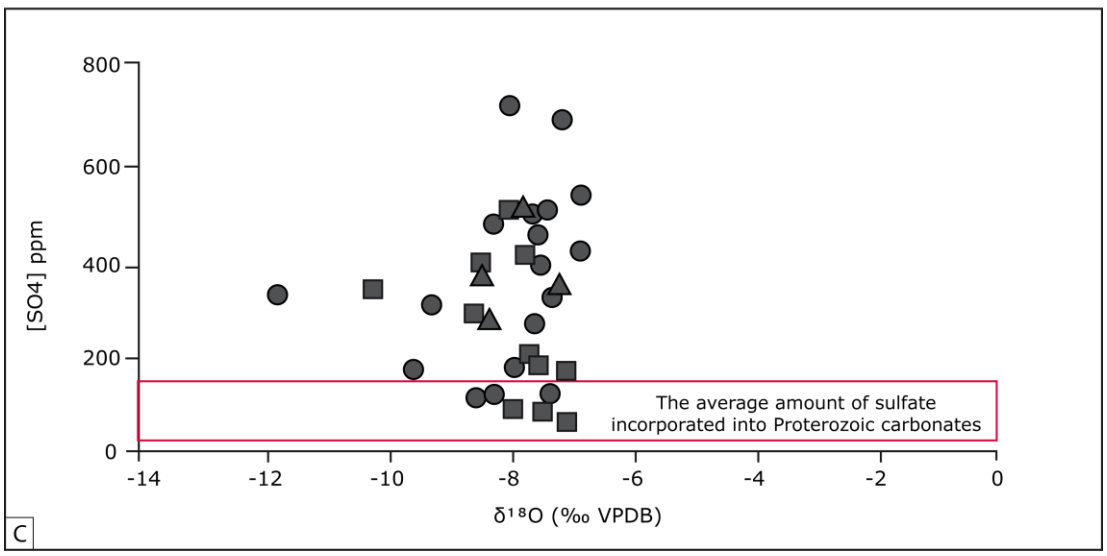
800
600
400
200
0
[SO4] ppm
The average amount of sulfate incorporated into Proterozoic carbonates
-14
-12
-10
-8
-6
-4
-2
0
δ¹⁸O (‰ VPDB)
C

In addition to the cations sodium and potassium, sulfate may also be an effective indicator of paleosalinity (Eugster and Hardie, 1978; Meyers et al., 1997), and carbonate associated sulfate (CAS) within calcite can be used to infer the composition of depositional and diagenetic fluids (Gill et al., 2008; Marenco et al., 2008; Staudt and Schoonen, 1995). CAS consists of sulfate ions structurally bound within the carbonate mineral, presumably incorporated through substitution for the carbonate ion (Busenberg and Plummer, 1985; Pingitore et al., 1995; Staudt and Schoonen, 1995; Kampschulte and Strauss, 2004). Modern, open marine waters contain approximately 28 mM, or about 2700 ppm sulfate. Whereas incorporation of CAS into biogenic calcite and aragonite can be as high as 10,000 ppm, concentrations are more typically 1000-3000 ppm in abiotic calcite (Staudt and Schoonen 1995). Phanerozoic marine carbonate rocks, however, typically contain between <1000 ppm sulfate (Staudt and Schoonen, 1995), reflecting a combination of diagenetic loss (cf. Gill et al., 2008) and potentially lower sulfate concentrations of the ancient ocean. Sulfate concentration in seawater at gypsum saturation is approximately 10,565 ppm and 21,321 ppm at halite saturation (Fontes and Matray, 1993); therefore, increased sulfate concentration in hypersaline waters, should be reflected in enhanced CAS incorporation (Staudt et al., 1993; Meyers et al., 1997).

Sulfate incorporation into carbonate during the Precambrian is more difficult to constrain, because the concentration of atmospheric oxygen, and thus marine sulfate, was likely substantially lower than in the modern (Canfield et al., 2000; Farquhar et al., 2000; Pope and Grotzinger, 2003; Kah et al., 2004; Kump, 2008). Current data on CAS concentration suggests average concentrations of up to approximately 1963 ppm in the Paleozoic (Horita, 2004; Spear et al., 2014), rising from approximately 300 ppm in the latest Proterozoic (Staudt and Schoonen, 1995; Hurtgen et al., 2002). These values, in turn, record a substantial increase in CAS incorporation from the late Mesoproterozoic (<150 ppm; Kah et al., 2004), the early Mesoproterozoic (~50 ppm; Gellatly and Lyons, 2005) and the late Paleoproterozoic (~30 ppm; Gellatly and Lyons, 2005). Combined, these data suggest that Mesoproterozoic marine carbonate minerals should preserve <150 ppm.

CAS data within potential calcitized evaporites facies of the Atar Group (Figure 11C) range from 75 to 721 ppm, with the majority showing concentrations greater than 100 ppm. The average concentration of these samples (317 ppm) is twice as high as sulfate concentrations recorded in marine carbonate from the 1.2 Ga Bylot Supergroup (~150 ppm; Kah et al., 2004), which are interbedded with marine gypsum deposits (Kah et al., 2001; 2004). Additionally, some values within the current sample suite are higher than the Paleozoic average of 324 ppm (Staudt et al.,

1993). Such elevated values are here interpreted to reflect an abundance of sulfate in the primary depositional phase. Primary deposition of gypsum, under conditions of low water–rock ratios, would be expected to produce sulfate-rich diagenetic fluids, even with the introduction of less saline fluids such as marine or meteoric water.

CHAPTER 5: DISCUSSION

Evaporite Minerals and their Diagenesis

A combination of macro- to microscale petrographic fabrics, mineralogical indicators, and trace element signatures—specifically the incorporation of Na, K, and SO_4—suggest that bright white limestone beds within Units I-6 (Oued Tariefet/Gouamir formations) and I-7 (Tawaz/Tenoumer formations) of the Atar Group represent the sedimentary deposition of marine evaporites and their subsequent calcitization. Macro-scale fabrics include massive and laminated, as well as an abundance of nodular fabrics that are characteristic of gypsum deposition and subsequent dehydration to anhydrite. Fabrics also display abundant evidence of dissolution, such as microkarstic features and stylolitization, indicating the presence of a soluble mineral phase. Many of these features are observed across the basin, although intraclastic breccias dominate fabrics in the interior basin (i.e., the Gouamir Formation). Within breccia facies, clasts are composed of microsparitic calcite, molar-tooth microspar, and coarse euhedral spar, and associated with secondary chlorite, pyrite, and euhedral dolomite. Nearly all samples—even those that preserve primary depositional fabrics preserved in poikilotopic calcite—contain coarse recrystallization fabrics, indicating a greater degree of overprinting of primary fabrics during diagenetic recrystallization than associated marine carbonate phases.

Although a majority of these samples which contain petrographic evidence for evaporite mineral deposition, Carbon and oxygen isotopes, and a standard suite of major, minor, and trace elements (Ca, Mg, Sr, Mn, Fe) do not uniquely indicate deposition from hypersaline waters. Carbon isotope compositions, for instance, are consistent with the stratigraphic position of the samples, and oxygen isotope compositions provide no clear support for primary deposition under hypersaline conditions. This latter observation contrasts sharply with data from other Mesoproterozoic evaporite-bearing basins that show distinct enrichment in oxygen isotopes of carbonate minerals in hypersaline environments relative to well-mixed marine waters (Kah, 2000). Similarly, trace elements such as Sr generally record lower concentrations than that of associated marine carbonate rocks. Together, these observations suggest that current lithologies dominantly reflect the diagenetic process of replacement of original phases by calcite, a process known as calcitization. Several samples, however, retain elevated concentrations of paleosalinity indicators

such as Na, K, and SO_4, which suggest retention of ions from dissolution of a soluble precursor phase.

Calcitization of evaporite deposits has been well documented, with numerous studies documenting the occurrence of evaporite replacement and their associated fabrics (West, 1973; Chafetz, 1979; Scholle et al., 1992; Ulmer-Scholle and Scholle, 1994; Dargam and Depetris, 1996; Sanz-Rubio et al., 2001; Gandin et al., 2005; Melezhik et al., 2005; Arp et al., 2008;). Many of these studies have economic focus (Eugster, 1985; Warren, 1986; Pierre and Rouchy, 1988), because the dissolution and precipitation process can result in substantial changes in porosity and permeability of deposits (Ulmer-Scholle and Scholle, 1994; Fernández-Díaz et al., 2009). Others studies focus on ancient lacustrine deposits, whose chemical history may be very different than that of marine evaporites (Eugster and Hardie, 1975; Martini, 1990; Bensin and Goldstein, 2001; Simpson et al., 2004; Warren, 2006). Unfortunately, only a few studies have focused on relative diagenetic behaviors of sulfate and associated carbonate from the same succession (Wigley, 1973; Pierre and Rouchy, 1988; Dargam and Depetris, 1996; Rouchy et al., 2001; Sanz-Rubio; 2001; Fernández-Díaz et al., 2009).

The primary necessity for the calcitization of evaporite deposits is the presence of bicarbonate. Therefore, investigation of the calcitization process has focused primarily on production of bicarbonate via thermochemical or bacterial sulfate reduction (TSR and BSR, respectively), or the delivery of bicarbonate through interaction with marine or meteoric fluid (Rouchy et al., 2001). TSR is a late diagenetic process that results from interaction of hydrocarbons and sulfate in anoxic environments, often at depth, and generally at temperatures greater than 100°C (Machel, 1992; Ulmer-Scholle and Scholle, 1994). Resulting calcite are associated with deposits of native sulfur (Stafford et al., 2008), as well as an association with a variety of sulfide minerals (pyrite, galena, and sphalerite) that reflect a combination of hydrogen sulfide production (Machel, 1992; Ulmer-Scholle and Scholle, 1994) and hydrothermal release of metals from surrounding facies. In lower temperature systems, typically between 20°C and 80°C, BSR appears to be the primary mechanism of reducing sulfate while increasing bicarbonate in the system (Machel, 1992). Although the products of BSR and TSR are similar, the two processes can be distinguished from one another by several factors. Dolomite formed via BSR is commonly microcrystalline, and easily distinguishable from coarse saddle dolomite precipitated via TSR (Machel, 1995). Additionally, both sulfur and oxygen isotopes can be used to distinguish between

BSR and TSR; with small, negative $\delta^{34}S$ values reflecting TSR processes and larger negative vales reflecting BSR (Machel, 1995). Similarly, oxygen isotopes in resultant calcites can be used to differentiate the temperature under which calcitization occurred with strongly negative isotopic compositions indicative of hydrothermal fluids (Machel, 1995).

A third mechanism of calcitization involves early diagenetic replacement by bicarbonate-rich near surface fluids, such as through the introduction of undersaturated water provided by underlying or adjacent aquifers (Schreiber and El-Tabakh, 2000; Armenteros, 2010). Such diagenetic processes occur most commonly in geologic areas where carbonates and evaporites are linked through sedimentary relationships, such as in supratidal marine settings, where carbonate deposition transitions to evaporite deposition in marginal areas (Rouchy et al., 2001). In this scenario, dissolution of sulfate occurs by the introduction of carbonate-rich waters undersaturated with respect to gypsum (Fernández-Díaz et al., 2009; Pierre and Rouchy, 1988; Sanz-Rubio et al., 2001; Wigley, 1973). Subsequent calcitization requires a supply of Ca^{2+} (much of which is supplied by the original gypsum) and CO_3^{2-} (supplied by the diagenetic fluids), and the removal of SO_4^{2-} (through water-rock interaction or local BSR). The reaction for calcitization of gypsum is:

$$CaSO_4 \bullet 2H_20 + Ca^{2+} + 2CO_3^{2-} \rightarrow SO_4^{2-} + 2CaCO_3 + 2H_2O \qquad (2)$$

The fabric of the resultant calcite depends strongly on the salinity of diagenetic fluids and the degree of water-rock interaction, wherein mimetic recrystallization (i.e. preservation of original fabric details; cf. Armenteros, 2010; Schreiber and El Tabakh, 2000) reflects interaction with strongly saline fluids. By contrast, this process can also result in very coarsely crystalline replacement, wherein low-salinity fluids result in rapid gypsum dissolution, and precipitation of calcite occurs primarily within open void space (Armenteros, 1999; 2010). The spar created by calcitization of gypsum can represent either the replacement (often poikilotopic) of the gypsum or passive fill of void spaces (Armenteros, 2010).

Calcitization of evaporites can occur at any point in the burial process (Warren, 1999) when the diagenetic fluids are undersaturated with respect to gypsum. The process is widely documented in phreatic zones and meteoric waters interact with evaporite beds (Lee and Harwood, 1989; Warren et al., 1990; Scholle et al., 1992; Warren, 1999). Under laboratory conditions, Fernandez-Diaz et al., (2009) demonstrated that the calcitization of gypsum proceeds through multiple dissolution and recrystallization reactions, which begins as soon as a carbonate-rich solution comes

in contact a with gypsum crystal. Both the path of reaction and degree of preservation of primary fabrics are strongly dependent on the initial carbonate concentration within the solution. Higher carbonate concentrations in the diagenetic fluid require a smaller amount of gypsum dissolution to reach saturation states necessary to initiate carbonate precipitation, thus permitting a finer scale of dissolution and reprecipitation necessary to preserve detailed features of the primary phases. Convserely, lower initial carbonate concentrations require that more gypsum be dissolved before supersaturation can occur and a calcite phase can nucleate, resulting in loss of original textures during the calcitization process and preservation of more coarsely recrystalline fabric (Fernandez-Diaz et al, 2009).

Observations of the meso- and microscale fabrics of Atar Group samples suggests calcitization via the introduction of one or more bicarbonate-rich fluid. Specifically, primary fabrics preserved within piokilotopic calcite, indicate a fine scale of dissolution and reprecipitation common to hypersaline fluid replacement, whereas clasts containing coarse, euhedral spar indicate a greater degree of dissolution prior to replacement by calcite, as would be expected from interaction with less saline fluid. Cubic clusters observed under cathodoluminescence are interpreted to be pseudomorphs after halite; and their uniform luminescence suggests wholesale dissolution of this highly soluble phase and subsequent, precipitation of calcite within the void space. This observation, in particular, suggests that fluids responsible for halite dissolution were sufficiently saline to readily dissolve halite, yet insufficiently saline to readily dissolve surrounding gypsum.

Reconstruction of Depositional and Diagenetic Fluids

Information regarding potential depositional and diagenetic fluids can be found using trace element concentrations preserved in mineral components. Trace elements can be incorporated into a crystalline phase by adsorption onto the crystal surface, as mineral or fluid inclusions, or through direct substitution into the crystal lattice by solid solution (McIntire, 1963). Substitution into a crystal lattice is assumed to occur under equilibrium conditions, and thus thermodynamic properties of the trace element and the solid solution can be used to calculate a distribution coefficient (Brand and Viezer, 1980a). Both empirically and experimentally derived distribution coefficients are used to relate the concentration of the co-precipitated cation, in reference to its

carrier ion in a homogeneous mineral phase, to the composition of the brine from which the mineral precipitated using the equation:

$$Dx = [X/Ca]_{solid}/[X/Ca]_{brine}$$

where X is the co-precipitated ion, and Ca represents the ion that is replaced through co-precipitation.

Distribution coefficients are often used to interpret the geochemistry of ancient environments (Rimstidt et al., 1998); however, the amount of a trace element that is incorporated into the mineral is dependent on variable parameters including precipitation rates and hydrodynamics, which are often unable to be constrained for ancient systems (Rimstidt et al., 1998). For instance, concentrations of trace elements are typically higher in biogeneic calcite than they are in abiotic marine calcite (Morse and Bender, 1990), likely reflecting biologically driven differences in mineral growth rate. Additionally, the presence of other trace elements in a solution may affect the distribution coefficient of trace element incorporation into a mineral (Ichinkuni, 1973; Mucci and Morse, 1983; Pingatore et al., 1986; Dromgoole and Walter, 1990; Rimstidt et al., 1998). Distribution coefficients determined experimentally have helped identify and constrain some of the influencing parameters, such as temperature and solution composition (Morse and Bender, 1990); however, applying distribution coefficients to natural systems involves uncertainty. Modeling of diagenetic fluids and their products using distribution coefficients must therefore be understood to reflect only a first-order approximation.

For this investigation, we calculated projected incorporation of Mg, Sr, Na, and K into calcite precipitated from a variety of fluid compositions. Table 2 provides distribution coefficients. Magnesium was inferred, however, not to be a viable recorder of fluid composition in whole rock samples because small amounts of later diagenetic dolomite was observed petrographically within most samples. Although the presence of dolomite indicates that local brines were enriched in Mg^{2+}, there is no way to differentiate to what extent the magnesium is sourced from original calcite or secondary brines. Similarly, Sr concentrations can reflect complex interactions between temperature, mineral precipitation rate, crystal structure, and Mg concentration (Carpenter and Lohmann, 1992; Mucci, 1998), which together can overprint the equilibrium signal represented by distribution coefficients, even at low water-rock ratios (Pingitore, 1982; Banner and Hanson, 1990). Generally low Sr concentrations in these rocks (cf. Figure 10) suggest that extensive

recrystallization may have overprinted signals of fluid composition. We therefore focused primarily on incorporation of salinity indicators Na and K.

To constrain a range of potential diagenetic fluids, we also considered two distinct classes of samples. Figures 11A and 11B show Na and K concentrations of all calcitized evaporite samples. For modeling purposes, we divided these values into trace element depleted and trace element enriched classes (Table 3). Trace element depleted (TED) samples make up the majority of samples, and preserve measured concentrations of Na and K that are within or below that expected from marine calcite precipitation. These samples have an average [Na/Ca] of 0.0019 ± 0.0148 ppm and an average [K/Ca] of 0.0005 ± 0.004 ppm. Trace element enriched (TEE) samples comprise a subset of calcitized evaporite samples and preserve measured concentrations of Na and K that are above that expected from marine calcite precipitation. These samples record [Na/Ca] of 0.0172 ± 0.1041 ppm and [K/Ca] of 0.0014 ± 0.0003 ppm (Table 3).

To establish a first order understanding of potential diagenetic fluids, we used known distribution coefficients (D_{Na} = 0.00015, and D_K = 0.0003; see Table 2) to calculate the average [Na/Ca] and [K/Ca] of fluids required to precipitate calcite with the composition of TED and TEE sample suites. For sodium, these calculations indicated liquids with [Na/Ca] of ~12 is required to precipitate calcite with [Na/Ca] similar to the TED sample suite, and liquids with [Na/Ca] of ~115 is required to precipitate calcite with [Na/Ca] similar to the TEE sample suite. For TED samples, a fluid composition with [Na/Ca] ~12 could clearly reflect a mixture of marine ([Na/Ca] = 26) and fresh ([Na/Ca] = 0.23) waters. Application of a simple mixing model (Table 3 suggests that such fluid would represent a mixture of 95% fresh water and 5% seawater. For TEE samples, [Na/Ca] of ~115 requires a fluid substantially more concentrated than seawater ([Na/Ca] = 26). Evaporation of seawater through gypsum salinities, however, are represented by a uniform increase in ionic compositions, and no substantial change in [Na/Ca]. These values, therefore, cannot be achieved simply through evaporation of seawater.

Table 2. Published distribution coefficients for trace element incorporation into calcite used throughout this study. A D_{Na} of 0.00015 was used, however the published D_{Na} ranges from 0.00017-0.0002 (c.f. Wit et al., 2013). *The high D_{Sr} value was determined using the equation from 3.52x10-6 (ppm Mg) + 0.0062 (Carpenter and Lohmann, 1982). The distribution coefficients for trace element incorporation into gypsum were used to model a pure gypsum.

Distribution Coefficients for Calcite			
Ratio mol/mol	D_x		Reference
	Low	High	
Mg/Ca	0.019	0.21	Mucci, 1998; Oomori et al., 1987
Sr/Ca	0.24	0.44*	Gabitov and Watson, 2006; Carpenter and Lohmann, 1982
Na/Ca	0.00015	0.0002	Ishikawa and Ichikuni, 1982; Wit et al., 2013
K/Ca	0.0003		Ishikawa and Ichikuni, 1982; Veizer et al., 1978

Distribution Coefficients for Gypsum			
Ratio mol/mol	Dx		Reference
	Low	High	
Mg/Ca	0.0000	0.00004	Kushnir, 1980
Sr/Ca	0.15	0.68	Kushnir, 1980
Na/Ca	0.00001	0.00031	Lu et al., 1997
K/Ca	0.00001	0.00034	Kushnir, 1980

Similarly, for potassium, calculations indicated liquids with [K/Ca] of ~1.5 is required to precipitate calcite with [K/Ca] similar to the TED sample suite, and liquids with [K/Ca] of ~4.5 is required to precipitate calcite with [K/Ca] similar to the TEE sample suite. Unlike for sodium, values for TED and TEE samples are greater than that expected from either seawater ([K/Ca] = 0.995), or seawater evaporated to gypsum salinities. The similarity between [K/Ca] values for seawater and TED samples, however, suggests that measured [K/Ca] values may be overestimated, suggesting a minor contribution of potassium from insoluble residues (Veizer et al., 1978).

Neither of these first-order approximations, however, takes into account the potential contribution of ions from the dissolution of precursor mineral phases. In order to explore the effects of gypsum dissolution on potential diagenetic fluids, we performed a series of calculations that explored the dissolution of a hypothetical gypsum by (i) average freshwater, (ii) seawater, and (iii) seawater of various evaporative concentrations (Table 5). Each of these scenarios was explored across water-rock ratios of 100 (i.e., 100 parts water to every 1 part gypsum) to 0.1 (i.e. 1 part water to 10 parts gypsum). In each scenario, composition of hypothetical gypsum was calculated using known distribution coefficients for trace element incorporation into gypsum (Table 2), and fluid compositions of modern seawater evaporated to gypsum saturation (Table 4). Fluids of different water–rock ratio were then calculated assuming dissolution of gypsum by the fluid, and incorporation of trace elements from the gypsum into the new fluid. Hypothetical diagenetic calcite was then precipitated from these fluids using known distribution coefficients for trace element incorporation into calcite (Table 2), and these concentrations compared to values observed in calcitized evaporite facies from the Atar Group (Table 3).

In each of these scenarios—dissolution of gypsum in fresh water, in seawater, and in evaporative seawater—calculated [Na/Ca] and [K/Ca] ratios of carbonate rock precipitated from modeled fluids are consistently several orders of magnitude lower (see Appendix 2) than concentrations measured in both TED and TEE samples (cf. Table 3), indicating that fluids arising from dissolution of precursor gypsum are incapable of reproducing [Na/Ca] and [K/Ca] measured in Atar Group calcitized evaporites.

Table 3. Concentration of sodium and potassium in the Atar Group calcitized evaporite phases. Trace element depleted samples preserve measured concentrations of Na and K that are within or below that expected from marine calcite precipitation. Trace element enriched samples preserve measured concentrations of Na and K that are above that expected from marine calcite precipitation.

Sodium Concentrations		
Trace Element Depleted Samples (N=32)		
	[Na] ppm	[Na/Ca]
Average	707.79	0.0019
High	1825.56	0.0049
Low	159.78	0.0004
Standard Deviation	396.77	0.0148
Trace Element Enriched Samples (N=6)		
	[Na] ppm	[Na/Ca]
Average	6636.99	0.0092
High	9775.66	0.0215
Low	4199.48	0.0007
Standard Deviation	2113.01	0.0085

Potassium Concentrations		
Trace Element Depleted Samples (N=32)		
	[K] ppm	[K/Cl]
Average	172.96	0.00046
High	768.42	0.00199
Low	46.91	0.00013
Standard Deviation	142.31	0.00037
Trace Element Enriched Samples (N=6)		
	[K] ppm	[K/Ca]
Average	533.33	0.0014
High	768.41	0.0020
Low	426.53	0.0011
Standard Deviation	124.54	0.0003

Neither of these first-order approximations, however, takes into account the potential contribution of ions from the dissolution of precursor mineral phases. In order to explore the effects of gypsum dissolution on potential diagenetic fluids, we performed a series of calculations that explored the dissolution of a hypothetical gypsum by (i) average freshwater, (ii) seawater, and (iii) seawater of various evaporative concentrations (Table 5). Each of these scenarios was explored across water-rock ratios of 100 (i.e., 100 parts water to every 1 part gypsum) to 0.1 (i.e. 1 part water to 10 parts gypsum). In each scenario, composition of hypothetical gypsum was calculated using known distribution coefficients for trace element incorporation into gypsum (Table 2), and fluid compositions of modern seawater evaporated to gypsum saturation (Table 4). Fluids of different water–rock ratio were then calculated assuming dissolution of gypsum by the fluid, and incorporation of trace elements from the gypsum into the new fluid. Hypothetical diagenetic calcite was then precipitated from these fluids using known distribution coefficients for trace element incorporation into calcite (Table 2), and these concentrations compared to values observed in calcitized evaporite facies from the Atar Group (Table 3).

In each of these scenarios—dissolution of gypsum in fresh water, in seawater, and in evaporative seawater—calculated [Na/Ca] and [K/Ca] ratios of carbonate rock precipitated from modeled fluids are consistently several orders of magnitude lower (see Appendix 2) than concentrations measured in both TED and TEE samples (cf. Table 3), indicating that fluids arising from dissolution of precursor gypsum are incapable of reproducing [Na/Ca] and [K/Ca] measured in Atar Group calcitized evaporites.

Table 4. A summary of major and minor ions in modern freshwater, seawater, gypsum saturated water, and halite saturated water. Seawater values from Fontes and Matray (1993) and Spear et al. (2014). Freshwater values were an average of river data from Banner (2004) and Garrels and Thompson (1962).

Element	Freshwater		Modern Seawater		Gypsum Saturation		Halite Saturation		Gypsum at Gypsum Saturation	
	mmol/Kg	ppm	mmol/Kg	ppm	mmol/Kg	ppm	mmol/Kg	ppm	mmol/Kg	ppm
Na	0.27	6.10	485.2	11159.6	1714.0	39422.0	4616.0	106168.0	97.4	2240
K	0.05	1.99	10.6	413.4	39.2	1528.8	103.0	4017.0	2.4	95.3
Mg	0.50	12.00	55.1	1322.4	194.0	4656.0	615.0	14760.0	1.5	36.7
Sr	0.00	0.11	0.1	8.2	0.3	23.0	0.5	39.6	32.4	2819.3
SO4	0.12	11.20	29.2	2803.2	110.0	10560.0	222.0	21312.0	7352.9	705882.0
Ca	0.65	25.95	10.6	424.0	40.1	1604.0	12.5	500.0	7353.0	294118.0
Cl	0.23	7.90	565.7	19799.5	2029.0	71015.0	5527.0	193445.0	-	-
[Na/Ca]	0.41	0.24	45.8	26.3	42.7	24.6	369.3	212.3	0.0	0.008
[K/Ca]	0.08	0.08	1.0	1.0	1.0	1.0	8.2	8.0	0.0	0.0003
[SO4/Ca]	0.18	0.43	2.8	6.6	2.7	6.6	17.8	42.6	1.0	2.4

This somewhat counterintuitive result, however, reflects the addition of Ca during dissolution of gypsum water-rock interaction in a closed system, where ionic products released from mineral dissolution remain within in the diagenetic fluid. The inability of these scenarios to reproduce likely diagenetic fluids therefore implies that calcitization occurred under open system conditions, wherein ions resulting from dissolution from precursor minerals were not necessarily constrained to remain within the system. Even in an open system, however, it is difficult to achieve [Na/Ca] and [K/Ca] compositions of TEE samples from ambeint surface waters (fresh, marine, or hypersaline) without an additional source of these monovalent cations. The most plausible explanation, therefore is that the original depositional phases consisted of a combination of gypsum+halite+potash salts (Fig. 12), and that the calcitization process occurred under water-rock ratios insufficient to flush these additional ions from the system. This scenario is consistent with cathodoluminescence evidence of halite pseudomorphs (Fig. 8D).

Insight into Proterozoic Seawater

In addition to examination of trace cations in Atar Group samples, we must also consider that the composition of these samples reflects more fundamental changes in ocean chemistry through time. Ancient marine sediments are mineralogically similar to modern marine sediments, and it is generally assumed that the evaporation sequence—the precipitation of carbonate is followed by the precipitation of gypsum, halite, and finally potash salts (Warren, 2006)—has remained constant throughout geologic time (Holland, 1972). Grotzinger (1989) however, proposed that the sequence in which evaporite minerals precipitate may have been different during the Precambrian as a result of an increased carbonate saturation state triggered by elevated atmospheric CO_2 during the Precambrian (Walker, 1983; Kasting, 1987; Grotzinger and Kasting, 1993; Bartley and Kah, 2004). If the ratio of $[HCO_3^-]$ to $[Ca^{2+}]$ reached values wherein $2[HCO_3^-] \geq [Ca^{2+}]$, available calcium would be depleted from the water column during carbonate precipitation, thereby preventing the formation of gypsum. Under these conditions, halite would precipitate directly after calcite. Support for this hypothesis comes from the general scarcity of evidence for gypsum precipitation in Proterozoic successions, yet evidence for halite precipitation (c.f. Pope and Grotzinger, 2003).

Table 5. Elemental concentrations used to determine the [Na/Ca] and [K/Ca] that can be obtained by mixtures of modern seawater and freshwater. These elemental ratios were then compared to those necessary to obtain the measured ratios within the Atar Group calcitized evaporites.

	Na		K		Ca		[Na/Ca]		[K/Ca]	
Mixing Ratio	mmol/Kg	ppm	mmol/Kg	ppm	mmol/Kg	ppm	mmol/Kg	ppm	mmol/Kg	ppm
Seawater	484.96	11154.00	10.62	414.00	10.40	416.00	15.42	26.81	0.97	1.00
95:5	460.72	10596.60	10.09	393.40	9.91	396.50	15.37	26.73	0.97	0.99
75:25	363.78	8367.00	7.97	311.00	7.96	318.25	15.12	26.29	0.95	0.98
50:50	242.61	5580.00	5.33	208.00	5.53	221.00	14.52	25.25	0.92	0.94
25:75	121.43	2793.00	2.69	105.00	3.09	123.50	13.00	22.62	0.83	0.85
5:95	24.50	563.40	0.58	22.60	1.14	45.50	7.12	12.38	0.48	0.50
Freshwater	0.26	6.00	0.05	2.00	0.65	26.00	0.13	0.23	0.08	0.08

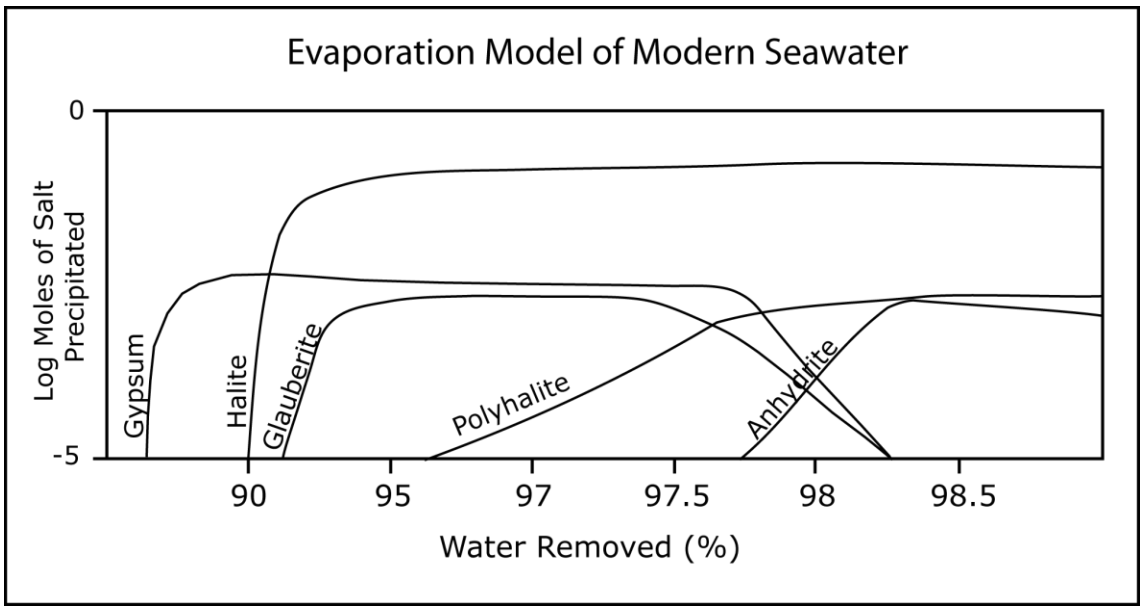

Figure 13. Evaporation sequence for modern seawater calculated via PHREEQC (Parkhurst and Appelo, 1999. Gypsum beings to precipitate out of solution when ~80% of modern seawater is evaporated from the system. Halite precipitation follows when 90% of seawater has been removed. Other sulfate and potash salts precipitate out of solution with anhydrite precipitating just after 97.5% of the water has been removed.

A second option to explain the general paucity of gypsum, particularly prior to the late Mesoproterozoic, is inhibition of gypsum precipitation by low marine sulfate concentrations (Kah et al., 2001). In this hypothesis, low pO_2 results in decreased concentration of sulfate delivery to marine systems. Coupled with oxygen depleted marine waters conducive to BSR (Ohmoto and Felder, 1987; Canfield and Thamdrub, 1994; Habicht and Canfield, 1996; Canfield et al., 2000; Bottrell and Newton, 2006; Laasko and Schrag, 2014), these conditions would result in potentially much lower marine sulfate concentrations. Lower sulfate concentrations would then result in a higher degree of evaporation necessary before gypsum saturation is reached (Kah et al., 2001). Although marine sulfate concentrations in the Precambrian are poorly constrained, estimates based on isotopic fractionation between SO_4 and H_2S (Habicht and Canfield, 2001) and on the rate of change of the isotopic concentrations suggest that marine sulfate concentrations in the Proterozoic may have gradually rose from values near 200-500 μM in the aftermath of the GOE (Habict et al., 2002; Shen et al., 2002; Kah et al., 2004) to no more than approximately 20.5 mM (15-25mM) in the latest Proterozoic (Brennan et al., 2004; Kah et al., 2004; see Bartley and Kah, 2011).

To better estimate sulfate concentrations of Proterozoic fluids, we can examine the concentration of CAS preserved within calcitized evaporites of the Atar Group. Published distribution coefficients for sulfate have been determined for the modern by Takano (1984) using the equation:

$$D^*_{SO_4} = \frac{\left({SO_4}^{2-}/{CO_3}^{2-}\right)_{rock}}{\left({SO_4}^{2-}/{HCO_3}^{-}\right)_{liquid}} \quad (3)$$

Unfortunately, this equation requires that bicarbonate concentration in marine fluids has remained constant through time. Although carbonate concentration is currently poorly constrained for the Proterozoic, it has been estimated vary substantially (Kasting, 1987; Bartley and Kah, 2004; Kah and Riding, 2007). Instead, the Berthelot-Nernst Distribution Law (equation 4; c.f. McIntire, 1963) was used to determine a first order partition coefficient from empirical measurement of modern carbonate minerals.

$$D_{SO_4} = \frac{(SO_4{}^{2-})_{rock}}{(SO_4{}^{2-})_{liquid}} \quad (4)$$

Modern seawater is 2804 ppm SO_4 (Fontes and Matray, 1993; Spear et al., 2014), and CAS in abiotic marine and fresh water calcites averages approximately 1500±500 ppm (1000-2000 ppm; Staudt and Schoonen, 1995). Using these values:

$$D_{SO_4} = \frac{(SO_4{}^{2-})_{rock}}{(SO_4{}^{2-})_{liquid}} = \frac{1500}{2804} = 0.535 \pm 0.178 \quad (5)$$

CAS concentrations in calcitized evaporites of the Atar Group range from 75 to 721 ppm, with an average of 310±166 ppm, with the three most elevated concentrations averaging approximately 645 ppm. We can compare these values to the low marine sulfate concentrations proposed for the Proterozoic oceans. Although data is sparse, CAS concentrations average ~50 ppm in the Paleoproterozoic (Gellaty and Lyons, 2005), ~100 ppm in the early Mesoproterozoic (Kah et al., 2004), ~200 ppm by the late Mesoproterozoic and early Neoproterozoic (Hurtgen et al., 2002; Kah et al., 2004), and ~325 ppm in the Paleozoic (Staudt et al., 1993)

Using the first order D_{SO_4} = 0.535±0.178, the values above were used to determine sulfate concentrations within calcites of those time periods. Sulfate concentrations appear to have changed from 101±36 ppm (1.1±0.4 mM) in the Paleoproterozoic, 203±71 ppm (2.1±0.7 mM) for the Mesoproterozoic, 405±143 mM (4.2±1.5 mM) for the Neoproterozoic, and as high as 652±232 ppm (6.9±2.4 mM) in the Paleozoic. These calculated values are consistent with the models performed by Kah et al. (2004) for Neoproterozoic seawater, as well as fluid inclusion data from Spear et al. (2014) which measured sulfate concentrations of ~3 mM for Neoproterozoic seawater. The calculated values for the Phanerozoic appear low and likely reflect the addition of biotically controlled CAS in the Phanerozoic, which tend to have much higher concentrations of CAS (Staudt and Schoonen, 1995).

Values calculated for the Proterozoic, however, suggest that non-evaporitic marine carbonates of the Atar Group should have CAS concentrations near 100 ppm. Measured concentrations of CAS in Atar Group calcitized evaporite samples (both TEE and TED samples) range from 75 to 721 ppm (average 312±166 pm) is therefore consistent with excess sulfate,

suggesting the retention of sulfate provided by dissolution of primary gypsum. We therefore used constraints for Precambrian seawater (Grotzinger, 1989; Grotzinger and Kastings, 1993; Kah et al., 2004; Spear et al., 2014) to model the evaporation sequence for the Precambrian (Fig. 14). Modern seawater parameters precipitate calcite, gypsum, halite, followed by anhydrite and potash salts. Precipitation within a high bicarbonate, low sulfate ocean during evaporation was modeled. Marine sulfate concentrations of 3 mM, consistent with estimates for the Mesoproterozoic, provide an evaporation sequence identical to the modern ocean (i.e., calcite, followed by gypsum, halite, and potash salts). Significantly more water, however, must be removed before precipitation of gypsum begins—gypsum begins evaporating at a concentration factor of 10, rather than 3.5, followed immediately by the onset of halite precipitation. This model is consistent with both fabric evidence (i.e., halite pseudomorphs) and trace element concentrations that suggest that precursor evaporites included gypsum+halite+potash phases.

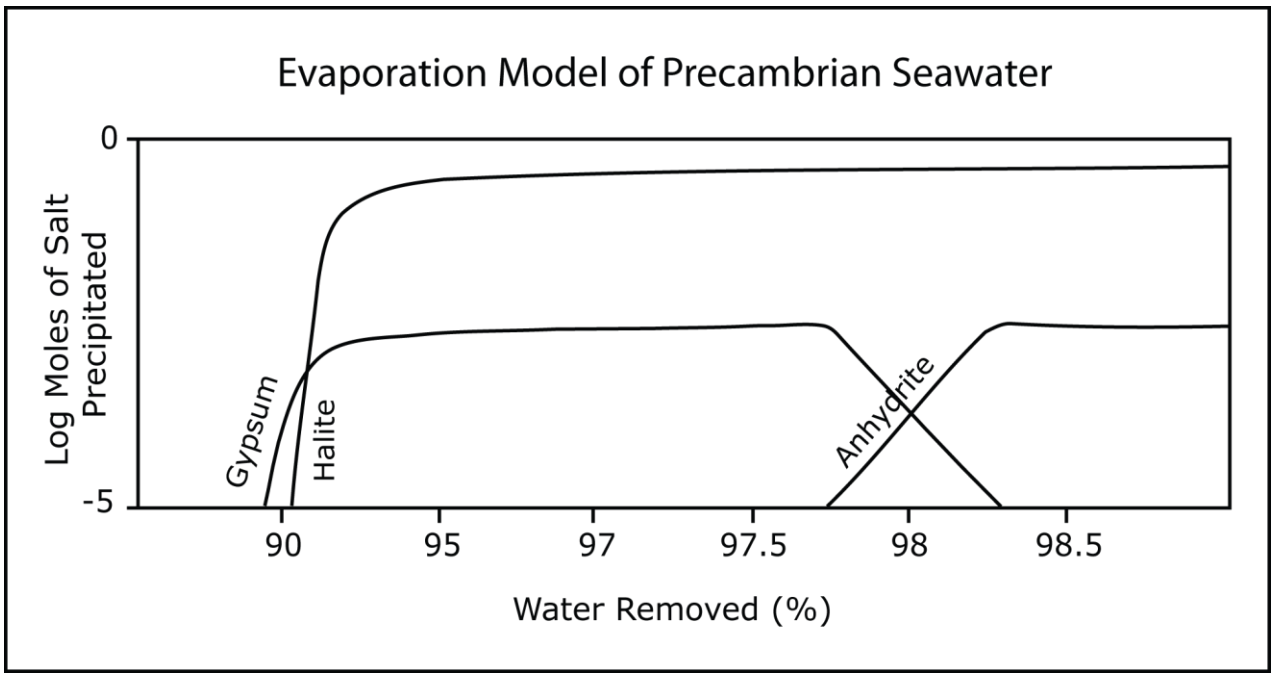

Figure 14. A model of the evaporation sequence of Precambrian seawater. Using element concentrations from Spear et al. (2014), and taking into account a low sulfate ocean, PHREEQC modeling shows that more water must be removed prior to the precipitation of gypsum; however, halite still precipitates after gypsum.

CHAPTER 6: CONCLUSIONS

Distinct white limestone beds of the Atar Group, in the Tauodeni Basin, Mauritania, Africa possess massive and nodular fabrics with microkarstic features and ptygmatic folds, indicative of an evaporite precursor—likely gypsum that underwent dehydration to anhydrite—that is presently preserved as calcite. Microscale fabrics are consistent with this interpretation and further suggest a complex interaction of different grain types and their diagenesis. Within intraformational breccias, for instance, a range of preserved microfabrics suggests a combination of sources that include both primary calcite and evaporite clasts. A few samples also contain halite pseudomorphs, suggesting that primary deposition may have been multi-mineralic. Combined, these fabric details suggest a complex evaporite precursor consisting of, minimally, gypsum+halite, deposited in environments that underwent sufficient evaporation to dehydrate gypsum to anhydrite.

Isotopic compositions of calcitized evaporite phases do not preserve evidence of primary, hypersaline waters, suggesting that water-rock interaction during calcitization was sufficient to overprint oxygen isotope compositions. Elevated concentrations of paleosalinity proxies such as sodium, potassium, and sulfate in a subset of samples, however, indicate at least some retention of a primary evaporitic chemistry.

Distribution coefficients related to trace element incorporation into calcite provide a means to explore potential fluids associated with deposition and diagenesis of these deposits. Concentrations of Na and K in the most trace element enriched samples are unable to be formed either through simple evaporation of seawater, or by the combination of seawater, evaporative seawater, and gypsum dissolution. Elevated Na and K concentrations in TEE samples are consistent with fabric evidence that requires the presence of halite, and suggests the presence of potash salts as well, in the original evaporite deposit. Although our data indicate that calcitization of these deposits occurred under open system conditions, fabric evidence and retention of elemental concentrations indicative of dissolution of halite±potash phases suggest that calcitization occurred primarily under low water-rock ratios.

Finally, a first-order distribution coefficient was determined in order to calculate the expected sulfate concentrations within the Mesoproterozoic ocean. This distribution coefficient (D_{SO4} =0.535±0.178) suggests marine sulfate concentrations of approximately 4.2 mM in the late Mesoproterozoic, which is consistent with both concentrations estimated via the rapidity of isotopic change in marine sulfate (Kah et al., 2004) and the composition of fluid inclusions

recovered from Neoproterozoic halite (Spear et al., 2014). At these sulfate concentrations, and consistent with fabric data presented here, a "modern" marine evaporation sequence will occur in which gypsum precipitated prior to halite. Low sulfate concentrations, however, require loss of nearly 90% of fluids (or a concentration factor of 10) prior to gypsum precipitation.

LIST OF REFERENCES

Aleali, M., Rahimpour-Bonab, H., Moussavi-Harami, R., and Jahani, D., 2013, Environmental and sequence stratigraphic implications of anhydrite textures: A case from the Lower Triassic of the Central Persian Gulf: Journal of Asian Earth Sciences, v. 75, no. 0, p. 110-125.

Alsharhan, A. S., and Sadd, J. L., 2000, Stylolites in Lower Cretaceous Carbonate Reservoirs, UAE: SEPM Special Publication v.69, p. 185-207.

Armenteros, I., 2010, Diagenesis of carbonates in continental settings, *in* Alonso-Zarza, A. M., and Tanner, L.H., ed., Carbonates in Continental Settings: Geochemistry, Diagenesis and Applications, Volume 62, Elsevier B.V.

Babel, M., 2004, Models for evaporite, selenite and gypsum microbialite deposition in ancient saline basins: Acta Geologica Polonica, v. 54, no. 2, p. 219-249.

Badiozamani, K., 1973, The Dorag dolomitization model--application to the Middle Ordovician of Wisconsin: Journal of Sedimentary Research, v. 43, no. 4.

Bathurst, R. G. C., 1980, Deep crustal diagenesis in limestones: Revista del Instituto de Investigaciones Geologicas de la Diputacion de Barcelona v. 34, p. 89-100.

Banner, J. L., 2004, Radiogenic isotopes: systematics and applications to earth surface processes and chemical stratigraphy: Earth-Science Reviews, v. 65, no. 3, p. 141-194.

Banner, J. L., and Hanson, G. N., 1990, Calculation of simultaneous isotopic and trace element variations during water-rock interaction with applications to carbonate diagenesis: Geochimica et Cosmochimica Acta, v. 54, no. 11, p. 3123-3137.

Bartley, J. K., and Kah, L. C., 2004, Marine carbon reservoir, Corg-Ccarb coupling, and the evolution of the Proterozoic carbon cycle: Geology, v. 32, no. 2, p. 129-132.

Bartley, J. K., Kah, L. C., McWilliams, J. L., and Stagner, A. F., 2007, Carbon isotope chemostratigraphy of the Middle Riphean type section (Avzyan Formation, Southern Urals, Russia): signal recovery in a fold-and-thrust belt: Chemical Geology, v. 237, no. 1, p. 211-232.

Bekker, A., and Holland, H. D., 2012, Oxygen overshoot and recovery during the early Paleoproterozoic: Earth and Planetary Science Letters, v. 317–318, no. 0, p. 295-304.

Bekker, A., Holland, H. D., Wang, P. L., Rumble, D., Stein, H. J., Hannah, J. L., Coetzee, L. L., and Beukes, N. J., 2004, Dating the rise of atmospheric oxygen: Nature, v. 427, no. 6970, p. 117-120.

Benan, C. A., and Deynoux, M., 1998, Facies analysis and sequence stratigraphy of Neoproterozoic platform deposits in Adrar of Mauritania, Taoudeni Basin, West Africa: Geologische Rundschau, v. 87, no. 3, p. 283-302.

Bertrand-Sarfati, J., and Moussine-Pouchkine, A., 1988, Is cratonic sedimentation consistent with available models? An example from the Upper Proterozoic of the West African craton: Sedimentary Geology, v. 58, no. 2–4, p. 255-276.

Bertrand-Sarfati, J., Moussine-Pouchkine, A., Amard, B., and Ahmed, A. A. K., 1995, First Ediacaran fauna found in western Africa and evidence for an Early Cambrian glaciation: Geology, v. 23, no. 2, p. 133-136.

Bishop, J. W., Sumner, D. Y., and Huerta, N. J., 2006, Molar tooth structures of the Neoarchean Monteville Formation, Transvaal Supergroup, South Africa. II: A wave-induced fluid flow model: Sedimentology, v. 53, no. 5, p. 1069-1082.

Blumenberg, M., Thiel, V., Riegel, W., Kah, L.C., Reitner, J., 2012, Black shale formation by microbial mats lacking sterane-producing eukaryotes, late Mesoproterozoic (1.1 Ga) Taoudeni Basin, Mauritania: Precambrian Research, v. 196-197, p. 113-127.

Bojanowski, M. J., Barczuk, A., and Wetzel, A., 2014, Deep-burial alteration of early-diagenetic carbonate concretions formed in Palaeozoic deep-marine greywackes and mudstones (Bardo Unit, Sudetes Mountains, Poland): Sedimentology, p. n/a-n/a.

Bottrell, S. H., and Newton, R. J., 2006, Reconstruction of changes in global sulfur cycling from marine sulfate isotopes: Earth-Science Reviews, v. 75, no. 1–4, p. 59-83.
Bowen, G. J., and Wilkinson, B., 2002, Spatial distribution of δ18O in meteoric precipitation: Geology, v. 30, no. 4, p. 315-318.
Brand, U., 2004, Carbon, oxygen and strontium isotopes in Paleozoic carbonate components: an evaluation of original seawater-chemistry proxies: Chemical Geology, v. 204, no. 1–2, p. 23-44.
Brand, U., and Veizer, J., 1980, Chemical diagenesis of a multicomponent carbonate system--1: Trace elements: Journal of Sedimentary Research, v. 50, no. 4.
-, 1981, Chemical diagenesis of a multicomponent carbonate system-2: stable isotopes: Journal of Sedimentary Research, v. 51, no. 3.
Brasier, A. T., Fallick, A. E., Prave, A. R., Melezhik, V. A., and Lepland, A., 2011, Coastal sabkha dolomites and calcitised sulphates preserving the Lomagundi-Jatuli carbon isotope signal: Precambrian Research, v. 189, no. 1–2, p. 193-211.
Brennan, S. T., Lowenstein, T. K., and Horita, J., 2004, Seawater chemistry and the advent of biocalcification: Geology, v. 32, no. 6, p. 473-476.
Brenneke, J., 2007, A Comparision of the stable oxygen and carbon isotope composition of early Cretaceous and late Jurassic carbonates from DSDP Sites 105 and 367.
Brocks, J. J., Love, G.D., Summons, R.E., Knoll, A.H., Logan, G.A., Bowden, S.A., 2005, Biomarker evidence for green and purple sulfur bacteria in a stratified Paleoproterozoic sea: Nature, v. 437, p. 866-870.
Busenberg, E., and Niel Plummer, L., 1985, Kinetic and thermodynamic factors controlling the distribution of SO32− and Na+ in calcites and selected aragonites: Geochimica et Cosmochimica Acta, v. 49, no. 3, p. 713-725.
Canfield, D. E., 2004, The evolution of the Earth surface sulfur reservoir: American Journal of Science, v. 304, no. 10, p. 839-861.
Canfield, D. E., Habicht, K. S., and Thamdrup, B., 2000, The Archean Sulfur Cycle and the Early History of Atmospheric Oxygen: Science, v. 288, no. 5466, p. 658-661.
Carpenter, S. J., and Lohmann, K. C., 1992, SrMg ratios of modern marine calcite: Empirical indicators of ocean chemistry and precipitation rate: Geochimica et Cosmochimica Acta, v. 56, no. 5, p. 1837-1849.
Chakrabarti, G., Shome, D., Kumar, S., Stephens III, G. M., and Kah, L. C., 2013, Carbonate platform development in a Paleoproterozoic extensional basin, Vempalle Formation, Cuddapah Basin, India: Journal of Asian Earth Sciences.
Clauer, N., Caby, R., Jeannette, D., and Trompette, R., 1982, Geochronology of sedimentary and metasedimentary Precambrian rocks of the West African craton: Precambrian Research, v. 18, no. 1–2, p. 53-71.
Clauer, N., and Deynoux, M., 1987, New information on the probable isotopic age of the late Proterozoic glaciation in West Africa: Precambrian research, v. 37, no. 2, p. 89-94.
Claypool, G. E., Holser, W. T., Kaplan, I. R., Sakai, H., and Zak, I., 1980, The age curves of sulfur and oxygen isotopes in marine sulfate and their mutual interpretation: Chemical Geology, v. 28, no. 0, p. 199-260.
Cook, N. D. J., and Ashley, P. M., 1992, Meta-evaporite sequence, exhalative chemical sediments and associated rocks in the Proterozoic Willyama Supergroup, South Australia: implications for metallogenesis: Precambrian Research, v. 56, no. 3–4, p. 211-226.
Dargam, R., and Depetris, P., 1996, Geochemistry of waters and brines from the Salinas Grandes basin, Córdoba, Argentina. II. Gypsum dissolution-calcite precipitation, and brine evolution: International Journal of Salt Lake Research, v. 5, no. 2, p. 81-101.

Dean, W. E., Davies, G. R., and Anderson, R. Y., 1975, Sedimentological significance of nodular and laminated anhydrite: Geology, v. 3, no. 7, p. 367-372.
Des Marais, D. J., 2001, Isotopic Evolution of the Biogeochemical Carbon Cycle During the Precambrian: Reviews in Mineralogy and Geochemistry, v. 43, no. 1, p. 555-578.
Dromgoole, E. L., and Walter, L. M., 1990, Iron and manganese incorporation into calcite: Effects of growth kinetics, temperature and solution chemistry: Chemical Geology, v. 81, no. 4, p. 311-336.
Duan, Y., Anbar, A. D., Arnold, G. L., Lyons, T. W., Gordon, G. W., and Kendall, B., 2010, Molybdenum isotope evidence for mild environmental oxygenation before the Great Oxidation Event: Geochimica et Cosmochimica Acta, v. 74, no. 23, p. 6655-6668.
El Tabakh, M., Grey, K., Pirajno, F., and Charlotte Schreiber, B., 1999, Pseudomorphs after evaporitic minerals interbedded with 2.2 Ga stromatolites of the Yerrida basin, Western Australia: Origin and significance: Geology, v. 27, no. 10, p. 871-874.
Eugster, H. P., and Hardie, L. A., 1975, Sedimentation in an ancient playa-lake complex: the Wilkins Peak Member of the Green River Formation of Wyoming: Geological Society of America Bulletin, v. 86, no. 3, p. 319-334.
Farquhar, J., Bao, H., Thiemens, M., 2000, Atmospheric Influence of Earth's Earliest Sulfur Cycle: Science, v. 289, p. 756-758.
Farquhar, J., and Wing, B. A., 2003, Multiple sulfur isotopes and the evolution of the atmosphere: Earth and Planetary Science Letters, v. 213, no. 1–2, p. 1-13.
Fernández-Díaz, L., Pina, C. M., Astilleros, J. M., and Sánchez-Pastor, N., 2009, The carbonatation of gypsum: Pathways and pseudomorph formation: American Mineralogist, v. 94, no. 8-9, p. 1223-1234.
Fontes, J. C., and Matray, J. M., 1993, Geochemistry and origin of formation brines from the Paris Basin, France: 1. Brines associated with Triassic salts: Chemical Geology, v. 109, no. 1–4, p. 149-175.
Frank, T., Kah, L., and Lyons, T., 2003, Changes in organic matter production and accumulation as a mechanism for isotopic evolution in the Mesoproterozoic ocean: Geological Magazine, v. 140, no. 04, p. 397-420.
Frei, R., Gaucher, Claudio, Poulton, Simon W., Canfield, Don E., 2009, Fluctuations in Precambrian atmospheric oxygenation recorded by chromium isotopes: Nature, v. 461, p. 250-253.
Fritz, P., and Katz, A., 1972, The sodium distribution of dolomite crystals: Chemical Geology, v. 10, no. 3, p. 237-244.
Furniss, G., Rittel, J. F., and Winston, D., 1998, Gas bubble and expansion crack origin of: Journal of Sedimentary Research, v. 68, no. 1.
Gandin, A., Wright, D.T., 2007, Evidence of vanished evaporites in Neoarchean carbonates of South Africa, *in* Schreiber, B. C., Lugli, S., and Babel, M., ed., Evaporites Through Time and Space, Volume 285, Geological Society, London, p. 285-308.
García-Ruiz, J. M., Villasuso, R., Ayora, C., Canals, A., and Otálora, F., 2007, Formation of natural gypsum megacrystals in Naica, Mexico: Geology, v. 35, no. 4, p. 327-330.
Gellatly, A. M., and Lyons, T. W., 2005, Trace sulfate in mid-Proterozoic carbonates and the sulfur isotope record of biospheric evolution: Geochimica et Cosmochimica Acta, v. 69, no. 15, p. 3813-3829.
Gill, B. C., Lyons, T. W., and Frank, T. D., 2008, Behavior of carbonate-associated sulfate during meteoric diagenesis and implications for the sulfur isotope paleoproxy: Geochimica et Cosmochimica Acta, v. 72, no. 19, p. 4699-4711.
Gilleaudeau, G. J., and Kah, L. C., 2013a, Oceanic molybdenum drawdown by epeiric sea expansion in the Mesoproterozoic: Chemical Geology, v. 356, p. 21-37.

Gilleaudeau, G., Kah, L.C., 2013b, Carbon isotope records in a Mesoproterozoic epicratontic sea: carbon cyclying in a low-oxygen world: Precambrian Research, v. 228, p. 85-101.
Girard, J.-P., Deynoux, M., and Nahon, D., 1989, Diagenesis of the upper Proterozoic siliciclastic sediments of the Taoudeni Basin (West Africa) and relation to diabase emplacement: Journal of Sedimentary Research, v. 59, no. 2.
Goodman, E. E., Kah, L.C, Trace sulfate concentrations as an indicator of depositional environment:examination of some possible calcitized evaporites from the Proterozoic Atar Group, Mauritania, *in* Proceedings Geological Society of America2004, Volume Abstracts with Programs 36, 37.
Grotzinger, J. P., 1989, Facies and evolution of Precambrian depositional systems: emergence of the modern platform archetype., *in* Crevello, P. D., Wilson, J.J., Sarg, J.F., Read, J.F., (Eds.), ed., Controls on Carbonate Platform and Basin Developement, Volume 44: Tulsa, OK, SEPM, p. 79-106.
Grotzinger, J. P., and Kasting, J. F., 1993, New Constraints on Precambrian Ocean Composition: The Journal of Geology, v. 101, no. 2, p. 235-243.
Grunau, H. R., 1987, A worldwide look at the cap-rock problem: Journal of Petroleum Geology, v. 10, no. 3, p. 245-265.
Guo, Q., Strauss, H., Kaufman, A. J., Schröder, S., Gutzmer, J., Wing, B., Baker, M. A., Bekker, A., Jin, Q., and Kim, S.-T., 2009, Reconstructing Earth's surface oxidation across the Archean-Proterozoic transition: Geology, v. 37, no. 5, p. 399-402.
Habicht, K. S., and Canfield, D. E., 2001, Isotope fractionation by sulfate-reducing natural populations and the isotopic composition of sulfide in marine sediments: Geology, v. 29, no. 6, p. 555-558.
Habicht, K. S., Gade, M., Thamdrup, B., Berg, P., and Canfield, D. E., 2002, Calibration of Sulfate Levels in the Archean Ocean: Science, v. 298, no. 5602, p. 2372-2374.
Heydari, E., and Moore, C. H., 1989, Burial diagenesis and thermochemical sulfate reduction, Smackover Formation, southeastern Mississippi salt basin: Geology, v. 17, no. 12, p. 1080-1084.
Hillier, S., 1993, Origin, diagenesis, and mineralogy of chlorite minerals in Devonian lacustrine mudrocks, Orcadian Basin, Scotland: Clays and Clay Minerals, v. 41, p. 240-240.
Horita, J., Zimmermann, H., and Holland, H. D., 2002, Chemical evolution of seawater during the Phanerozoic: Implications from the record of marine evaporites: Geochimica et Cosmochimica Acta, v. 66, no. 21, p. 3733-3756.
Hurtgen, M. T., Arthur, M. A., Suits, N. S., and Kaufman, A. J., 2002, The sulfur isotopic composition of Neoproterozoic seawater sulfate: implications for a snowball Earth?: Earth and Planetary Science Letters, v. 203, no. 1, p. 413-429.
Hussain, M., and Warren, J. K., 1989, Nodular and enterolithic gypsum: the “sabkha-tization” of Salt Flat playa, west Texas: Sedimentary Geology, v. 64, no. 1–3, p. 13-24.
Ichikuni, M., 1973, Partition of strontium between calcite and solution: Effect of substitution by manganese: Chemical Geology, v. 11, no. 4, p. 315-319.
Ishikawa, M., and Ichikuni, M., 1984, Uptake of sodium and potassium by calcite: Chemical geology, v. 42, no. 1, p. 137-146.
Jaworska, J. and Nowak. M., 2013, Anydrites from gypsum cap-rock of Zechstein salt diapirs: Geology, Geophyics and Environment, v. 39, no. 3, p. 223-250.
Johnston, D. T., 2011, Multiple sulfur isotopes and the evolution of Earth's surface sulfur cycle: Earth-Science Reviews, v. 106, no. 1–2, p. 161-183.
Kah, L. C., 2000, Preservation of depositional 18O signatures in Proterozoic dolostones: geochemical constraints on seawater chemistry and early diagenesis. , *in* Grotzinger, J. P., James, N.P., ed., Precambrian Carbonates, Volume 65: Tulsa, OK, SEPM, p. 345–360.

Kah, L. C., and Bartley, J. K., 2011, Protracted oxygenation of the Proterozoic biosphere: International Geology Review, v. 53, no. 11-12, p. 1424-1442.
Kah, L. C., Bartley, J. K., and Teal, D. A., 2012, Chemostratigraphy of the Late Mesoproterozoic Atar Group, Taoudeni Basin, Mauritania: Muted isotopic variability, facies correlation, and global isotopic trends: Precambrian Research, v. 200–203, no. 0, p. 82-103.
Kah, L. C., Lyons, T.W., Chesley, J.T., 2001, Geochemistry of a 1.2 Ga carbonate-evaporite succession, northern Baffin and Bylot Islands: implications for Mesoproterozoic marine evolution: Precambrian Research, v. 111, p. 203-234.
Kah, L. C., Lyons, T.W., Frank, T.D, 2004, Low marine sulphate and protracted oxygenation of the Proterozoic biosphere: Nature, v. 431, p. 834-838.
Kampschulte, A., and Strauss, H., 2004, The sulfur isotopic evolution of Phanerozoic seawater based on the analysis of structurally substituted sulfate in carbonates: Chemical Geology, v. 204, no. 3, p. 255-286.
Karhu, J. A., and Holland, H. D., 1996, Carbon isotopes and the rise of atmospheric oxygen: Geology, v. 24, no. 10, p. 867-870.
Kasprzyk, A., and OrtÍ, F., 1998, Palaeogeographic and burial controls on anhydrite genesis: the Badenian basin in the Carpathian Foredeep (southern Poland, western Ukraine): Sedimentology, v. 45, no. 5, p. 889-907.
Kaufman, A. J., Hayes, J., Knoll, A. H., and Germs, G. J., 1991, Isotopic compositions of carbonates and organic carbon from upper Proterozoic successions in Namibia: stratigraphic variation and the effects of diagenesis and metamorphism: Precambrian Research, v. 49, no. 3, p. 301-327.
Kaufman, A. J., Johnston, D. T., Farquhar, J., Masterson, A. L., Lyons, T. W., Bates, S., Anbar, A. D., Arnold, G. L., Garvin, J., and Buick, R., 2007, Late Archean Biospheric Oxygenation and Atmospheric Evolution: Science, v. 317, no. 5846, p. 1900-1903.
Kendall, A. C., 1984, Evaporites: Facies models, p. 259-296.
Kitano, Y., Okumura, M., and Idogaki, M., 1975, Incorporation of sodium, chloride and sulfate with calcium carbonate: Geochem. J, v. 9, p. 75-84.
Kump, L. R., 2008, The rise of atmospheric oxygen: Nature, v. 451, no. 7176, p. 277-278.
Kushnir, J., 1980, The coprecipitation of strontium, magnesium, sodium, potassium and chloride ions with gypsum. An experimental study: Geochimica et Cosmochimica Acta, v. 44, no. 10, p. 1471-1482.
-, 1982, The composition and origin of brines during the Messinian desiccation event in the Meditterranean Basin as deduced from concentrations of ions coprecipitated with gypsum and anhydrite: Chemical Geology, v. 35, no. 3, p. 333-350.
Laakso, T. A., and Schrag, D. P., 2014, Regulation of atmospheric oxygen during the Proterozoic: Earth and Planetary Science Letters, v. 388, p. 81-91.
Land, L. S., and Hoops, G. K., 1973, Sodium in carbonate sediments and rocks; a possible index to the salinity of diagenetic solutions: Journal of Sedimentary Research, v. 43, no. 3, p. 614-617.
Lehmann, M. F., Bernasconi, S. M., Barbieri, A., and McKenzie, J. A., 2002, Preservation of organic matter and alteration of its carbon and nitrogen isotope composition during simulated and in situ early sedimentary diagenesis: Geochimica et Cosmochimica Acta, v. 66, no. 20, p. 3573-3584.
Lorens, R. B., 1981, Sr, Cd, Mn and Co distribution coefficients in calcite as a function of calcite precipitation rate: Geochimica et Cosmochimica Acta, v. 45, no. 4, p. 553-561.
Lu, F. H., Meyers, W. J., and Schoonen, M. A., 1997, Minor and trace element analyses on gypsum: an experimental study: Chemical geology, v. 142, no. 1, p. 1-10.
Lyons, T. W., and Gill, B. C., 2010, Ancient Sulfur Cycling and Oxygenation of the Early Biosphere: Elements, v. 6, no. 2, p. 93-99.

Lyons, T. W., and Severmann, S., 2006, A critical look at iron paleoredox proxies: New insights from modern euxinic marine basins: Geochimica et Cosmochimica Acta, v. 70, no. 23, p. 5698-5722.
Machel, H. G., and Burton, E. A., 1991, Factors governing cathodoluminescence in calcite and dolomite, and their implications for studies of carbonate diagenesis.
Marshall, J. D., 1992, Climatic and oceanographic isotopic signals from the carbonate rock record and their preservation: Geological Magazine, v. 129, no. 2, p. 143-160.
Martini, J., 1990, An early proterozoic playa in the Pretoria group, Transvaal, South Africa: Precambrian research, v. 46, no. 4, p. 341-351.
Melezhik, V., Lepland, A., Romashkin, A., Rychanchik, D., Mesli, M., Finne, T., and Conze, R., the FAR-DEEP Scientists (2010) FAR-DEEP (Fennoscandian Arctic Russia–Drilling Early Earth Project) a remarkable opportunity for studying the great oxidation event: Sci Drill, v. 9, p. 23-29.
Melezhik, V. A., Fallick, A. E., Rychanchik, D. V., and Kuznetsov, A. B., 2005, Palaeoproterozoic evaporites in Fennoscandia: implications for seawater sulphate, the rise of atmospheric oxygen and local amplification of the δ13C excursion: Terra Nova, v. 17, no. 2, p. 141-148.
Meunier, A., 2010, Clays, Springer.
Meyers, W. J., Lu, F. H., and Zachariah, J. K., 1997, Dolomitization by mixed evaporative brines and freshwater, upper Miocene carbonates, Nijar, Spain: Journal of Sedimentary Research, v. 67, no. 5, p. 898-912.
Morse, J. W., and Bender, M. L., 1990, Partition coefficients in calcite: Examination of factors influencing the validity of experimental results and their application to natural systems: Chemical Geology, v. 82, p. 265-277.
Morse, J. W., and Mackenzie, F. T., 1990, Geochemistry of sedimentary carbonates, Elsevier.
Moussine-Pouchkine, A., and Bertrand-Sarfati, J., 1997, Tectonosedimentary subdivisions in the Neoproterozoic to Early Cambrian cover of the Taoudenni basin (Algeria-Mauritania-Mali): Journal of African Earth Sciences, v. 24, no. 4, p. 425-443.
Mucci, A., and Morse, J. W., 1983, The incorporation of Mg< sup> 2+</sup> and Sr< sup> 2+</sup> into calcite overgrowths: influences of growth rate and solution composition: Geochimica et Cosmochimica Acta, v. 47, no. 2, p. 217-233.
Murray, R. C., 1964, Origin and diagenesis of gypsum and anhydrite: Journal of Sedimentary Research, v. 34, no. 3, p. 512-523.
Okumura, M., and Kitano, Y., 1986, Coprecipitation of alkali metal ions with calcium carbonate: Geochimica et Cosmochimica Acta, v. 50, no. 1, p. 49-58.
Ono, S., Eigenbrode, J. L., Pavlov, A. A., Kharecha, P., Rumble III, D., Kasting, J. F., and Freeman, K. H., 2003, New insights into Archean sulfur cycle from mass-independent sulfur isotope records from the Hamersley Basin, Australia: Earth and Planetary Science Letters, v. 213, no. 1, p. 15-30.
Park, W. C., and Schot, E. H., 1968, Stylolites: their nature and origin: Journal of Sedimentary Research, v. 38, no. 1.
Parkhurst, D. L., and Appelo, C., 1999, User's guide to PHREEQC (Version 2): A computer program for speciation, batch-reaction, one-dimensional transport, and inverse geochemical calculations.
Pavlov, A., and Kasting, J., 2002, Mass-independent fractionation of sulfur isotopes in Archean sediments: strong evidence for an anoxic Archean atmosphere: Astrobiology, v. 2, no. 1, p. 27-41.
Pierre, C., and Rouchy, J. M., 1988, Carbonate replacements after sulfate evaporites in the middle Miocene of Egypt: Journal of Sedimentary Research, v. 58, no. 3.
Pingitore Jr, N. E., and Eastman, M. P., 1986, The coprecipitation of Sr< sup> 2+</sup> with calcite at 25° C and 1 atm: Geochimica et Cosmochimica Acta, v. 50, no. 10, p. 2195-2203.

Pingitore Jr, N. E., Meitzner, G., and Love, K. M., 1995, Identification of sulfate in natural carbonates by X-ray absorption spectroscopy: Geochimica et Cosmochimica Acta, v. 59, no. 12, p. 2477-2483.
Pingitore, N. E., 1982, The role of diffusion during carbonate diagenesis: Journal of Sedimentary Research, v. 52, no. 1, p. 27-39.
Pique, A., 2001, Geology of Northwest Africa, Berlin, Gebruder Borntraeger.
Pollock, M. D., Kah, L. C., and Bartley, J. K., 2006, Morphology of molar-tooth structures in Precambrian carbonates: influence of substrate rheology and implications for genesis: Journal of Sedimentary Research, v. 76, no. 2, p. 310-323.
Pomoni-Papaioannou, F., and Karakitsios, V., 2002, Facies analysis of the Trypali carbonate unit (Upper Triassic) in central-western Crete (Greece): an evaporite formation transformed into solution-collapse breccias: Sedimentology, v. 49, no. 5, p. 1113-1132.
Pope, M. C., and Grotzinger, J. P., 2003, Paleoproterozoic Stark Formation, Athapuscow Basin, Northwest Canada: Record of Cratonic-Scale Salinity Crisis: Journal of Sedimentary Research, v. 73, no. 2, p. 280-295.
Rimstidt, J. D., Balog, A., and Webb, J., 1998, Distribution of trace elements between carbonate minerals and aqueous solutions: Geochimica et Cosmochimica Acta, v. 62, no. 11, p. 1851-1863.
Rooney, A. B., Selby, D., Houzay, J.P., Renne, P.R., 2010, Re-Os geochronology of a Mesoproterozoic sedimentary succession, Taoudeni basin, Mauritania: Implications for basin-wide correlations and Re-Os organic-rich sediments systematics: Earth and Planetary Science Letters, no. 289, p. 486-496.
Rouchy, J., and Monty, C., 2000, Gypsum microbial sediments: Neogene and modern examples: Microbial Sediments: Berlin, Springer-Verlag, p. 209-216.
Rouchy, J. M., Taberner, C., and Peryt, T. M., 2001, Sedimentary and diagenetic transitions between carbonates and evaporites: Sedimentary Geology, v. 140, no. 1–2, p. 1-8.
Sanz-Rubio, E., Sánchez-Moral, S., Cañaveras, J., Calvo, J., and Rouchy, J., 2001, Calcitization of Mg–Ca carbonate and Ca sulphate deposits in a continental Tertiary basin (Calatayud Basin, NE Spain): Sedimentary Geology, v. 140, no. 1, p. 123-142.
Sarg, J., 2001, The sequence stratigraphy, sedimentology, and economic importance of evaporite–carbonate transitions: a review: Sedimentary Geology, v. 140, no. 1, p. 9-34.
Savard, M. M., Veizer, J., and Hinton, R., 1995, Cathodoluminescence at low Fe and Mn concentrations: a SIMS study of zones in natural calcites: Journal of Sedimentary Research, v. 65, no. 1.
Schlanger, S. O., 1964, Petrology of the limestones of Guam., Volume 260-BB, U.S. Geological Survery Professional Paperrs, p. 991-1038.
Schreiber, B. C., El Tabakh, Mohamed, 2000, Deposition and early alteration of evaporites: Sedimentalogy, v. 47, p. 215-236.
Schreiber, B. C., Friedman, G. M., Decima, A., and Schreiber, E., 1976, Depositional environments of Upper Miocene (Messinian) evaporite deposits of the Sicilian Basin*: Sedimentology, v. 23, no. 6, p. 729-760.
Scott, C., Lyons, T., Bekker, A., Shen, Y., Poulton, S., Chu, X., and Anbar, A., 2008, Tracing the stepwise oxygenation of the Proterozoic ocean: Nature, v. 452, no. 7186, p. 456-459.
Scott, C., and Lyons, T. W., 2012, Contrasting molybdenum cycling and isotopic properties in euxinic versus non-euxinic sediments and sedimentary rocks: refining the paleoproxies: Chemical Geology, v. 324, p. 19-27.
Shearman, D., 1987, Evaporites of coastal sabkhas.
Shen, Y., Canfield, D. E., and Knoll, A. H., 2002, Middle Proterozoic ocean chemistry: Evidence from the McArthur Basin, northern Australia: American Journal of Science, v. 302, no. 2, p. 81-109.

Simpson, E., Eriksson, K., Kuklis, C., Eriksson, P., Bumby, A., and van Jaarsveld, C., 2004, Saline pan deposits from the~ 1.8 Ga Makgabeng formation, Waterberg group, South Africa: Sedimentary Geology, v. 163, no. 3, p. 279-292.

Smoot, J. P., and Lowenstein, T. K., 1991, Depositional environments of non-marine evaporites: Developments in sedimentology, v. 50, p. 189-347.

Smosna, R., 1983, Diagenetic history of the Silurian Keefer sandstone in West Virginia and Kentucky: Journal of Sedimentary Research, v. 53, no. 4.

Sommer, S. E., 1972, Cathodoluminescence of carbonates, 2. Geological applications: Chemical Geology, v. 9, no. 1, p. 275-284.

Spear, N., Holland, H. D., Garcia-Veígas, J., Lowenstein, T. K., Giegengack, R., and Peters, H., 2014, Analyses of fluid inclusions in Neoproterozoic marine halite provide oldest measurement of seawater chemistry: Geology, v. 42, no. 2, p. 103-106.

Spencer, R. J., 2000, Sulfate Minerals in Evaporite Deposits, p. 173-192.

Spencer, R. J., Lowenstein, T.K., 1990, Evaporites, *in* McIlreath, I., Morrow, D.W., ed., Diagenesis, p. 141-163.

Stafford, K. W., Ulmer-Scholle, D., and Rosales-Lagarde, L., 2008, Hypogene calcitization: Evaporite diagenesis in the western Delaware Basin: Carbonates and evaporites, v. 23, no. 2, p. 89-103.

Staudt, W. J., Oswald, E. J., and Schoonen, M. A., 1993, Determination of sodium, chloride and sulfate in dolomites: a new technique to constrain the composition of dolomitizing fluids: Chemical Geology, v. 107, no. 1, p. 97-109.

Staudt, W. J., and Schoonen, M. A., 1995, Sulfate incorporation into sedimentary carbonates, *in* Proceedings ACS Symposium Series, v. 612, ACS Publications, p. 332-347.

Strauss, H., 2003, Sulphur isotopes and the early Archaean sulphur cycle: Precambrian Research, v. 126, no. 3, p. 349-361.

Takano, B., 1985, Geochemical implications of sulfate in sedimentary carbonates: Chemical Geology, v. 49, no. 4, p. 393-403.

Tucker, M., 2001, Sedimentary Petrology.p.272 , Blackwell Publishing.

Turner, E. C., and Kamber, B. S., 2012, Arctic Bay Formation, Borden Basin, Nunavut (Canada): Basin evolution, black shale, and dissolved metal systematics in the Mesoproterozoic ocean: Precambrian Research, v. 208, p. 1-18.

Ulmer-Scholle, D. S., Scholle, Peter A, 1994, Replacement of evaporites within the Permian Park City Formation, Bighorn Basin, Wyoming, USA: Sedimentology, v. 41, no. 6, p. 1203-1222.

Veizer, J., 1978, Secular variations in the composition of sedimentary carbonate rocks, II. Fe, Mn, Ca, Mg, Si and minor constituents: Precambrian Research, v. 6, no. 3–4, p. 381-413.

Veizer, J., 1983, Trace elements and isotopes in sedimentary carbonates: Reviews in Mineralogy and Geochemistry, v. 11, no. 1, p. 265-299.

Veizer, J., Lemieux, J., Jones, B., Gibling, M. R., and Savelle, J., 1977, Sodium: paleosalinity indicator in ancient carbonate rocks: Geology, v. 5, no. 3, p. 177-179.

Villeneuve, M., and Cornée, J., 1994, Structure, evolution and palaeogeography of the West African craton and bordering belts during the Neoproterozoic: Precambrian Research, v. 69, no. 1, p. 307-326.

Warren, J., 2000, Evaporites, brines and base metals: Low-temperature ore emplacement controlled by evaporite diagenesis: Australian Journal of Earth Sciences, v. 47, no. 2, p. 179-208.

Warren, J. K., 2006, Evaporites: Sediments, Resources and Hydrocarbons, Springer, 943 p.:

Warren, J. K., 2010, Evaporites through time: Tectonic, climatic and eustatic controls in marine and nonmarine deposits: Earth-Science Reviews, v. 98, no. 3–4, p. 217-268.

Warren, J. K., and Kendall, C. G. S. C., 1985, Comparison of sequences formed in marine sabkha (subaerial) and salina (subaqueous) settings--modern and ancient: AAPG Bulletin, v. 69, no. 6, p. 1013-1023.

West, I., 1973, Vanished Evaporites--Significance of Strontium Minerals: Journal of Sedimentary Research, v. 43, no. 1.

Whelan, J. F., Rye, R. O., Delorraine, W. F., and Ohmoto, H., 1990, Isotopic geochemistry of the mid-Proterozoic evaporite basin; Balmat, New York: American Journal of Science, v. 290, no. 4, p. 396-424.

White, A. F., 1977, Sodium and potassium coprecipitation in aragonite: Geochimica et Cosmochimica Acta, v. 41, no. 5, p. 613-625.

Wigley, T., 1973, Chemical evolution of the system calcite-gypsum-water: Canadian Journal of Earth Sciences, v. 10, no. 2, p. 306-315.

Wit, J. C., de Nooijer, L., Wolthers, M., and Reichart, G.-J., 2013, A novel salinity proxy based on Na incorporation into foraminiferal calcite: Biogeosciences, v. 10, no. 10.

APPENDICES

APPENDIX 1

Sample	Formation	Unit	Category	Meters	d13/12C	d18/16O	Ca (ppm)	Mg (ppm)	Fe (ppm)	Sr (ppm)	Mn (ppm)	Na (ppm)	K (ppm)	Notes
R1-D1	Tourist	I-5	Non-evaporite	219.90	-3.14	-7.49	385672.99	4521.10	8272.68	214.34	763.16			(clayey-r)
R1-D3-1	Tourist	I-5	Non-evaporite	217.40	-3.18	-7.28	392977.94	2969.65	2861.17	142.01	845.80			
R1-D3-2	Tourist	I-5	Non-evaporite	217.40	-3.02	-7.81	388276.80	4071.88	6030.40	210.68	958.99			(clayey-r)
R1-D4-1	Tourist	I-5	Non-evaporite	215.55	-3.69	-7.97	304821.35	19301.12	68861.12	897.80	1199.49			(clayey-r)
R1-D4-2	Tourist	I-5	Non-evaporite	215.55	-3.12	-8.02	389325.00	3879.70	5179.37	192.36	1016.46			
R1-D5-1	Tourist	I-5	Non-evaporite	214.20	-3.12	-7.94	374018.63	2804.33	21596.41	265.31	1116.88			(clayey)
R1-D5-2	Tourist	I-5	Non-evaporite	214.20	-3.02	-8.00	377503.55	6879.86	13218.44	250.29	1042.28			(clayey-r)
R1-D7-1	Tourist	I-5	Non-evaporite	211.00	-3.14	-7.68	376195.37	4562.70	17422.99	255.33	973.55			(clayey-r)
R1-D7-2	Tourist	I-5	Non-evaporite	211.00	-2.45	-7.15	393665.73	1998.97	3367.97	141.30	832.24			
R1-D8-1	Tourist	I-5	Non-evaporite	209.70	-2.33	-6.97	393792.92	2813.28	2428.46	137.40	659.42			
R1-D8-2	Tourist	I-5	Non-evaporite	209.70	-2.56	-7.04	393878.48	2874.43	2303.82	125.48	636.27			(clayey-r)
R1-D9	Tourist	I-5	Non-evaporite	208.20	-2.56	-7.34								(clayey-r)
R1-D10	Tourist	I-5	Non-evaporite	206.65	-2.70	-7.04	392887.30	2185.18	4066.18	157.00	669.61			(clayey-r)
R1-D11	Tourist	I-5	Non-evaporite	205.10	-2.21	-7.04	392792.70	2476.79	3845.98	154.64	632.27			(clayey-r)
R1-D12	Tourist	I-5	Non-evaporite	203.60	-1.97	-7.38	386551.99	4218.98	7821.44	186.64	733.57			(clayey-r)
R1-D13	Tourist	I-5	Non-evaporite	202.20	-2.14	-7.35	389731.99	3224.68	5909.03	204.43	665.78			(clayey-r)
R1-D13-1	Tourist	I-5	Non-evaporite	202.20	-2.18	-7.38	387018.05	3483.88	8245.68	192.48	734.28			(clayey-r)
R1-D13-2	Tourist	I-5	Non-evaporite	202.20	-2.04	-7.25	389223.47	3769.36	5774.50	161.24	688.08			
R1-D14	Tourist	I-5	Non-evaporite	200.60	-2.03	-7.37	387386.42	3742.88	7480.17	169.31	839.78			(clayey-r)
R1-D15	Tourist	I-5	Non-evaporite	199.00										No 15 in inventory
R1-D15-1	Tourist	I-5	Non-evaporite	199.00	-2.08	-7.27								(clayey-r)
R1-D15-2	Tourist	I-5	Non-evaporite	199.00	-1.60	-7.37								(clayey)
R1-D24	Tourist	I-5	Non-evaporite	188.45	-0.06	-6.36	384652.76	5354.60	7766.60	335.05	1149.38	2124.52	406.31	milled chips
R1-D25	Aguelt El Mabha	I-5	Non-evaporite	187.45	-0.01	-5.45	389944.64	2907.77	4942.33	1844.04	166.23	571.06	1010.55	milled chips
R1-D26	Aguelt El Mabha	I-5	Non-evaporite	185.60	-0.47	-7.00	386767.98	4060.99	7395.74	765.50	557.47	380.12	676.12	milled chips
R1-D27	Aguelt El Mabha	I-5	Non-evaporite	184.10	-0.64	-7.04	392069.45	2929.08	3343.44	1007.79	454.07			
R1-D28	Aguelt El Mabha	I-5	Non-evaporite	183.90	-0.67	-6.80	386279.11	3044.08	8901.35	970.58	574.07	442.73	719.47	milled chips
R1-D29	Aguelt El Mabha	I-5	Non-evaporite		-0.41	-6.49	389835.78	2427.72	6629.19	566.50	449.79	222.11	280.50	
R1-D29-1	Aguelt El Mabha	I-5	Non-evaporite	183.40	-0.70	-6.08	389121.10	2765.69	6672.86	776.36	498.56			milled chips
R1-D30-1	Aguelt El Mabha	I-5	Non-evaporite	181.90	-0.61	-6.45								
R1-D30-2	Aguelt El Mabha	I-5	Non-evaporite	181.90	-0.60	-6.70	392844.94	1232.57	4636.61	1091.51	364.67			
R1-D31	Aguelt El Mabha	I-5	Non-evaporite	179.00	-0.46	-6.37								
R1-D32	Aguelt El Mabha	I-5	Non-evaporite	177.60	-0.43	-7.06	389040.50	2801.49	6452.16	865.45	667.07	417.26	882.41	milled chips
R1-D33	Aguelt El Mabha	I-5	Non-evaporite	176.25	-0.06	-6.08	388615.25	1643.42	6981.34	2557.43	280.55			
R1-D34	Aguelt El Mabha	I-5	Non-evaporite	174.60	-0.16	-6.04	377462.31	5059.61	14608.03	1877.66	294.45			(clayey)
R1-D35	Aguelt El Mabha	I-5	Non-evaporite	173.00	-0.97	-6.99	385566.00	3171.50	9062.06	1158.09	782.36			
R1-D36	Aguelt El Mabha	I-5	Non-evaporite	171.45	-0.25	-6.71								
R1-D37A	Aguelt El Mabha	I-5	Non-evaporite	170.15	-0.44	-5.94	390327.95	2024.71	5444.30	1443.80	756.20			
R1-D37B-1	Aguelt El Mabha	I-5	Non-evaporite	170.15	-0.69	-6.76	367110.69	4839.04	24856.40	1663.44	851.34			(clayey)
R1-D37B-2	Aguelt El Mabha	I-5	Non-evaporite	170.15	-0.64	-6.80	387272.01	2057.93	8370.10	1558.80	727.39			
R1-D38-1	Aguelt El Mabha	I-5	Non-evaporite	168.50	-0.52	-6.27	376099.42	4903.53	15080.42	2727.87	521.81			(clayey)
R1-D38-2	Aguelt El Mabha	I-5	Non-evaporite	168.50	-0.63	-7.18	387303.16	3031.39	7166.19	1481.53	791.46			
R1-D39-1	Aguelt El Mabha	I-5	Non-evaporite	167.20	-0.13	-6.30	385724.83	1282.30	9744.88	3053.76	348.73			(clayey)
R1-D39-2	Aguelt El Mabha	I-5	Non-evaporite	167.20	-0.18	-6.24	386499.46	2029.35	8219.30	2754.07	489.42			
R1-D40	Aguelt El Mabha	I-5	Non-evaporite	165.50	-0.81	-7.19	381308.37	3390.02	12607.99	1368.86	1008.54			(clayey)
R1-D41-1	Aguelt El Mabha	I-5	Non-evaporite	164.10			380611.80	4642.67	11694.81	1802.50	652.30			(clayey)
R1-D41-2	Aguelt El Mabha	I-5	Non-evaporite	164.10	-0.81	-6.94								
R1-D42	Aguelt El Mabha	I-5	Non-evaporite	163.25	-0.34	-6.71	378845.94	2877.97	15549.65	1915.91	603.73			
R1-D43	Aguelt El Mabha	I-5	Non-evaporite	161.75	-0.69	-6.40	390223.76	2638.05	4947.91	1118.17	936.03	277.81	468.98	milled chips
R1-D44	Aguelt El Mabha	I-5	Non-evaporite	160.25	-0.81	-6.16	362026.54	6832.25	27605.36	1141.10	1234.39			
R1-D45	Aguelt El Mabha	I-5	Non-evaporite	158.70	-0.89	-6.14	377697.86	3250.12	12590.52	1676.02	1124.30	1297.19	1626.83	milled chips
R1-D47-1	Aguelt El Mabha	I-5	Non-evaporite	155.65	-0.91	-6.98	378352.00	4512.67	14193.65	889.38	1479.28			(clayey)
R1-D47-2	Aguelt El Mabha	I-5	Non-evaporite	155.65	-0.91	-6.15	383516.78	4517.97	9288.71	800.25	1315.67			
R1-D48	Aguelt El Mabha	I-5	Non-evaporite	154.15	-0.52	-6.90	363339.59	5477.29	25878.21	1819.65	2646.05			(clayey)
R1-D49	Aguelt El Mabha	I-5	Non-evaporite	152.40	-0.31	-6.47	385994.14	2721.58	7449.21	1154.74	2519.69			
R1-D50-1	Aguelt El Mabha	I-5	Non-evaporite	150.90	-0.39	-6.69	388322.40	3570.23	5596.60	1047.04	1121.83			
R1-D50-2	Aguelt El Mabha	I-5	Non-evaporite	150.90	-0.39	-6.14	389920.78	3026.72	4974.24	1061.87	795.57			
R1-D51A-1	Aguelt El Mabha	I-5	Non-evaporite	149.30	-0.66	-7.37	370558.61	6536.38	19459.24	869.50	1520.19			(clayey)
R1-D51A-2	Aguelt El Mabha	I-5	Non-evaporite	149.30	-0.47	-5.82	388837.61	3799.11	5257.05	813.35	902.23			
R1-D51B-1	Aguelt El Mabha	I-5	Non-evaporite	149.30	-0.74	-7.55	378866.87	4814.30	13146.52	813.62	1719.71			(clayey)
R1-D51B-2	Aguelt El Mabha	I-5	Non-evaporite	149.30	-0.39	-5.99	388519.43	3935.55	5238.82	843.13	1042.07			
R1-D52	Aguelt El Mabha	I-5	Non-evaporite	147.90	-0.30	-6.58	389106.13	2835.68	5647.82	1615.95	613.74			
R1-D53	Aguelt El Mabha	I-5	Non-evaporite	146.40	-0.46	-6.01	385558.95	1964.04	9516.59	2476.17	489.09			
R1-D54-1	Aguelt El Mabha	I-5	Non-evaporite	144.90	-0.84	-6.12	383743.00	3638.73	9377.66	2511.08	363.28			(clayey)
R1-D54-2	Aguelt El Mabha	I-5	Non-evaporite	144.90	-0.22	-6.68	391776.55	2177.00	3799.44	1589.33	623.38			
R1-D55	Aguelt El Mabha	I-5	Non-evaporite	143.40	-0.41	-6.41	373135.01	5624.07	18208.11	1546.36	647.43			(clayey)
R1-D56A	Aguelt El Mabha	I-5	Non-evaporite	141.90	-0.25	-7.18	364287.58	5766.36	27021.64	1169.05	852.37			
R1-D56B	Aguelt El Mabha	I-5	Non-evaporite	141.90	-0.60	-6.59	373098.62	4571.72	19734.38	1138.65	856.02			(clayey)
R1-D57-1	Aguelt El Mabha	I-5	Non-evaporite	140.30	-0.41	-6.51	390481.21	1683.56	5355.63	1543.26	1007.36			
R1-D57-2	Aguelt El Mabha	I-5	Non-evaporite	140.30	-0.43	-7.26	388975.48	2413.51	6000.42	1341.19	1180.32			
R1-D58-1	Aguelt El Mabha	I-5	Non-evaporite	139.00	-0.08	-6.40	376720.49	4135.36	16330.08	1778.22	543.17			(clayey)
R1-D58-2	Aguelt El Mabha	I-5	Non-evaporite	139.00	-0.20	-6.14	387187.31	2609.93	7990.46	1495.85	582.02			
R1-D59	Aguelt El Mabha	I-5	Non-evaporite	137.80	-2.20	-5.50	389672.32	3554.55	4842.23	890.84	704.27			(clayey)
R1-D60	Aguelt El Mabha	I-5	Non-evaporite	137.10	-1.83	-6.76	383456.09	3788.81	9285.22	831.33	2238.60			milled chips
R1-D61	Aguelt El Mabha	I-5	Non-evaporite	135.90	-3.38	-8.18								milled chips
R1-D63	Aguelt El Mabha	I-5	Non-evaporite	133.20	-5.26	-10.56	356532.73	7020.74	27951.65	607.13	6658.11			milled chips
R1-D64-1	Aguelt El Mabha	I-5	Non-evaporite	131.10	-3.68	-8.89	378195.06	2102.67	13838.88	1282.14	4546.71			
R1-D64-2	Aguelt El Mabha	I-5	Non-evaporite	131.10	-3.74	-9.25	364197.95	2836.59	26892.74	1086.56	4763.13			(clayey)
R1-D65	Aguelt El Mabha	I-5	Non-evaporite	130.10	-6.83	-10.52	345134.90	9132.60	36749.64	781.90	6398.85			milled chips
R1-D67B-1	Aguelt El Mabha	I-5	Non-evaporite	126.90	-6.33	-8.34	354045.92	6602.87	33363.07	623.29	4223.32			(clayey)
R1-D67B-2	Aguelt El Mabha	I-5	Non-evaporite	126.90	-2.11	-7.61	381519.39	1217.40	13188.85	1539.08	2701.06			
R1-D68-1	Aguelt El Mabha	I-5	Non-evaporite	125.20	-6.95	-10.54								
R1-D68-2	Aguelt El Mabha	I-5	Non-evaporite	125.20	-7.66	-10.28	348534.64	5372.13	30861.29	603.07	13761.03			(clayey)
R1-D69A-1	Aguelt El Mabha	I-5	Non-evaporite	124.70	-0.35	-7.55	382610.85	4884.66	10416.04	1228.58	215.86			(clayey)
R1-D69A-2	Aguelt El Mabha	I-5	Non-evaporite	124.70	-0.67	-7.05	391781.29	3414.28	3501.21	813.79	188.06			
R1-D69B-1	Aguelt El Mabha	I-5	Non-evaporite	124.70	-4.11	-7.72	366162.93	5567.54	24929.75	598.71	1890.85			(clayey)
R1-D69B-2	Aguelt El Mabha	I-5	Non-evaporite	124.70	-2.81	-7.52	375346.14	5023.41	16573.87	405.03	1955.38			
R1-D70-1	Aguelt El Mabha	I-5	Non-evaporite	122.20	-4.24	-7.62	362944.33	3080.71	31258.97	623.66	1810.13			(clayey)
R1-D70-2	Aguelt El Mabha	I-5	Non-evaporite	122.20	-3.47	-8.33	367669.69	2166.73	27141.93	549.18	2409.72			
R1-D71	Aguelt El Mabha	I-5	Non-evaporite	121.10	-2.73	-7.79	363976.37	3667.70	28515.57	612.49	2811.33	2322.09	4684.50	milled chips
R1-D72	Aguelt El Mabha	I-5	Non-evaporite	119.70	-3.28	-8.23	351849.59	6499.08	36602.58	867.33	3055.00	3434.13	6169.40	milled chips
R1-D73	Aguelt El Mabha	I-5	Non-evaporite	118.40	-3.21	-7.69	376436.82	3951.09	15934.79	853.77	2371.54	3028.80	4825.76	milled chips
R1-D75	Aguelt El Mabha	I-5	Non-evaporite	116.25	-3.43	-8.22	378807.38	2690.05	14231.20	980.18	3126.28	785.45	1013.50	milled chips
R1-D76	Aguelt El Mabha	I-5	Non-evaporite	114.75	-5.73	-10.77	379526.40	2725.51	10456.89	1104.69	6014.84	2920.47	5348.28	milled chips
R1-D79	Aguelt El Mabha	I-5	Non-evaporite	110.70	-3.00	-9.20	331204.76	11139.76	51206.00	1518.54	2522.23	9560.24	13089.75	milled chips
R1-D79-1	Aguelt El Mabha	I-5	Non-evaporite	110.70	-2.15	-7.28	367219.20	6273.58	22986.19	728.92	1782.98			(clayey)
R1-D79-2	Aguelt El Mabha	I-5	Non-evaporite	110.70	-2.77	-8.38	378557.77	2766.95	15250.16	799.08	2443.55			
R1-D81-1	Aguelt El Mabha	I-5	Non-evaporite	107.60	-1.76	-7.30	382160.33	2106.57	13556.15	828.45	1317.98			(clayey)
R1-D81-2	Aguelt El Mabha	I-5	Non-evaporite	107.60	-1.20	-6.95	386395.44	3213.49	7930.93	999.72	1192.74			
R1-D83	Aguelt El Mabha	I-5	Non-evaporite	105.15	-1.29	-7.32	396254.24	1506.67	1617.08	208.67	527.43			
R1-D84	Aguelt El Mabha	I-5	Non-evaporite	103.70	-0.87	-6.72	393293.91	2076.83	3506.73	524.92	586.67			
R1-D85	Gouamir	I-6	Non-evaporite	102.10	-0.89	-6.99	388553.60	3952.66	5723.81	900.36	444.91	149.85	256.50	
R1-D85	Gouamir	I-6	Non-evaporite	102.10	-0.80	-7.25	390547.21	2937.47	5026.39	866.23	422.25			milled chips
R1-D87A-1	Gouamir	I-6	Non-evaporite	99.50	-1.06	-7.04	386172.72	3839.71	8231.27	917.93	433.14			(clayey)
R1-D87A-2	Gouamir	I-6	Non-evaporite	99.50	-0.28	-6.26	392305.19	3317.13	2650.31	1181.26	266.68			
R1-D87B-1	Gouamir	I-6	Non-evaporite	99.50	-1.13	-7.39	386649.83	3709.02	7939.05	865.69	460.81			(clayey)
R1-D87B-2	Gouamir	I-6	Non-evaporite	99.50	-0.52	-6.63	391836.42	3474.77	2947.04	1096.46	330.99			
R1-D88	Gouamir	I-6	Non-evaporite	97.80	-0.79	-7.15	392396.48	2054.36	4688.34	461.10	392.60			
R1-D89	Gouamir	I-6	Non-evaporite	96.45	-1.11	-7.17	388450.94	5288.72	4442.49	813.19	288.91	239.17	472.30	
R1-D89	Gouamir	I-6	Non-evaporite	96.45	-1.14	-7.39								milled chips
R1-D90	Gouamir	I-6	Non-evaporite	94.95	-0.98	-7.24	385941.21	4284.36	5623.44	920.3235255	434.01	691.88	1265.99	milled chips
R1-D92-1	Gouamir	I-6	Non-evaporite	92.00	-0.70	-7.46	384804.49	5382.78	7815.58	831.64	418.17			(clayey)
R1-D92-2	Gouamir	I-6	Non-evaporite	92.00	-0.42	-7.01	382341.56	7955.43	7090.03	867.60	421.40			

Sample	Formation	Unit	Category	Meters	d13/12C	d18/16O	Ca (ppm)	Mg (ppm)	Fe (ppm)	Sr (ppm)	Mn (ppm)	Na (ppm)	K (ppm)	Notes
R1-D95-1	Gouamir	I-6	Non-evaporite	88.40	-0.85	-7.46	381861.84	4296.68	11920.47	922.22	482.87			(clayey)
R1-D95-2	Gouamir	I-6	Non-evaporite	88.40	-1.28	-6.88	389866.26	2671.99	6236.52	723.17	358.09			
R1-D97	Gouamir	I-6	Non-evaporite	86.85	-0.85	-7.30	382770.31	7168.63	7702.70	655.79	554.39			milled chips
R1-D98	Gouamir	I-6	Non-evaporite	85.40	-1.23	-7.82	383250.13	5060.81	9348.99	836.64	822.34			milled chips
R1-D100	Gouamir	I-6	Non-evaporite	83.00	-1.10	-7.23								
R1-D100	Gouamir	I-6	Non-evaporite	83.00	-1.04	-7.40	384553.42	5547.52	7740.39	745.27	629.06	657.49	1148.42	milled chips
R1-D102-1	Gouamir	I-6	Non-evaporite	80.40	-1.04	-6.74	390603.43	2650.23	5274.27	697.95	635.96			
R1-D102-2	Gouamir	I-6	Non-evaporite	80.40	-1.34	-7.58	380762.83	2896.28	14577.97	805.75	749.53			(clayey)
R1-D103	Gouamir	I-6	Non-evaporite	79.05	-0.80	-7.07	387132.21	3220.99	7821.50	996.52	560.80			
R1-D103	Gouamir	I-6	Non-evaporite	79.05	-0.89	-7.40	381630.94	3580.72	13059.92	719.11	651.47	287.07	534.78	milled chips
R1-D104-1	Gouamir	I-6	Non-evaporite	77.50	-0.70	-7.73								(clayey)
R1-D104-2	Gouamir	I-6	Non-evaporite	77.50	-0.53	-6.84	394210.26	1350.98	3235.20	956.85	392.52			
R1-D105	Gouamir	I-6	Non-evaporite	76.00	-1.24	-6.94	388013.33	3472.45	6548.85	1043.58	600.60	490.60	1217.34	milled chips
R1-D106-1	Gouamir	I-6	Non-evaporite	75.50	-1.38	-7.18	376560.86	5519.91	15487.87	771.79	855.55			
R1-D106-2	Gouamir	I-6	Non-evaporite	75.50	-0.76	-8.20	338898.26	17930.49	37790.45	457.64	884.49			(clayey)
R1-D108-1	Gouamir	I-6	Non-evaporite	71.50	-0.42	-7.44	378349.92	2751.63	17152.79	1202.18	364.08			(clayey)
R1-D108-2	Gouamir	I-6	Non-evaporite	71.50	-0.59	-6.46	393332.68	3053.49	2001.21	1210.61	181.14			
R1-D110	Gouamir	I-6	Non-evaporite	68.60	-0.64	-7.51	384763.48	6481.03	6754.68	675.00	336.98			(clayey)
R1-D111	Gouamir	I-6	Non-evaporite	67.30	-0.93	-7.15	392018.47	3026.68	3632.23	914.04	191.28			
R1-D112-1	Gouamir	I-6	Non-evaporite	65.60	-0.81	-7.13								(clayey)
R1-D112-2	Gouamir	I-6	Non-evaporite	65.60	-1.00	-6.66	395472.15	1905.32	1652.03	879.06	119.64			
R1-D113	Gouamir	I-6	Non-evaporite	64.00	-0.97	-7.63	390931.17	3136.28	4865.66	558.57	265.50			
R1-D114	Gouamir	I-6	Non-evaporite	62.50	-0.84	-6.77	375048.95	1650.87	22421.40	802.91	139.25			
R1-D115	Gouamir	I-6	Non-evaporite				390732.09	3556.81	4703.07	467.59	206.26			
R1-D116	Gouamir	I-6	Non-evaporite	59.55	-0.99	-6.73	394060.24	1396.81	3892.10	656.05	130.65			
R1-D117	Gouamir	I-6	Non-evaporite	58.00	-0.98	-6.98	395246.21	1666.52	2628.94	358.95	178.44			
R1-D118-1	Gouamir	I-6	Non-evaporite	56.50	-0.45	-7.74	392075.16	2951.83	3754.67	867.95	149.34			
R1-D118-2	Gouamir	I-6	Non-evaporite	56.50	-0.40	-7.67	394947.71	1061.83	3236.22	805.77	156.73			
R1-D119-1	Gouamir	I-6	Non-evaporite	55.10	-1.38	-8.87	386736.39	2744.18	9565.94	425.96	363.09			(clayey)
R1-D119-2	Gouamir	I-6	Non-evaporite	55.10	-1.16	-7.33								
R1-D121	Gouamir	I-6	Non-evaporite	53.20	-0.54	-7.88	395579.67	1477.28	2401.80	444.16	216.91			
R1-D122	Gouamir	I-6	Non-evaporite	51.70	-1.18	-7.44	388692.39	6926.11	2520.42	530.37	259.43			
R1-D123	Gouamir	I-6	Non-evaporite	50.20	-1.33	-7.17	395131.89	1828.35	2211.56	635.74	236.77			
R1-D124-1	Gouamir	I-6	Non-evaporite	48.70	-0.89	-7.36	393700.66	2705.01	2857.65	320.68	270.59			
R1-D124-2	Gouamir	I-6	Non-evaporite	48.70	-0.67	-7.42	396849.59	1235.72	1519.20	334.83	232.96			
R1-D125	Gouamir	I-6	Non-evaporite	47.30	-0.78	-7.55	396400.80	1350.69	1775.65	311.64	308.69			
R1-D134-1	Gouamir	I-6	Non-evaporite	36.45	-0.57	-7.88	388071.79	4455.60	5870.87	875.02	191.39			(clayey)
R1-D134-2	Gouamir	I-6	Non-evaporite	36.45	-0.02	-7.27	396155.98	1638.43	1547.13	570.47	173.87			
R1-D145	Gouamir	I-6	Non-evaporite	29.80	-0.35	-7.68	391086.56	2591.65	5285.01	391.84	520.15			
R1-D145-1	Gouamir	I-6	Non-evaporite	29.80	-0.93	-7.90	367183.76	8679.78	21581.24	374.85	616.92			(clayey)
R1-D145-2	Gouamir	I-6	Non-evaporite	29.80	-0.70	-8.44	389804.18	2106.69	7210.39	319.23	538.08			
R1-D146	Gouamir	I-6	Non-evaporite	29.30	-0.24	-8.49	386347.58	6979.75	4608.61	219.17	752.73			
R1-D127	Gouamir	I-6	Eavporite		-0.63	-7.16	392683.58	4440.40	1638.86	324.46	250.22	159.90	161.33	
R1-D128	Gouamir	I-6	Eavporite		-0.61	-7.04	384414.88	9977.07	2728.39	533.74	257.55	285.99	226.81	
R1-D129	Gouamir	I-6	Eavporite		-0.59	-7.49	390808.82	2255.43	1243.80	282.56	223.12	5022.67	117.36	
R1-D130	Gouamir	I-6	Eavporite		-0.64	-7.11	395596.12	1889.56	1056.96	280.83	269.42	816.78	252.32	milled chips
R1-D131	Gouamir	I-6	Eavporite		-0.41	-7.05	357604.96	28913.89	5480.21	170.21	415.44	1067.76	158.35	milled chips
R1-D132	Gouamir	I-6	Eavporite				382561.78	11155.26	3009.79	186.09	259.89	725.17	250.62	milled chips
R1-D133	Gouamir	I-6	Eavporite		-0.16	-7.64	382611.48	10732.60	3569.34	234.34	258.17	477.45	355.73	milled chips
R1-D135	Gouamir	I-6	Evaporite				393201.63	2036.47	3252.38	558.13	199.07	512.80	284.32	milled chips
R1-D136	Gouamir	I-6	Eavporite		-0.35	-8.38	385342.02	3190.98	1867.80	659.81	203.98	8278.60	158.55	milled chips
R1-D137	Gouamir	I-6	Eavporite		-0.46	-7.92	378626.31	10149.87	3266.66	230.03	245.78	5580.65	129.68	
R1-D138	Gouamir	I-6	Eavporite		-0.41	-7.43	393092.22	3154.95	1695.18	443.11	206.32	1093.57	200.81	
R1-D139	Gouamir	I-6	Eavporite		-0.45	-7.8	373352.37	16710.15	5284.36	263.07	329.30	789.16	128.89	
R1-D140	Gouamir	I-6	Eavporite		-0.55	-7.67	396013.49	2019.43	1418.77	215.59	234.35	153.60	130.43	
R1-D141	Gouamir	I-6	Eavporite		-0.34	-8.5	373370.44	16861.11	5444.71	261.56	334.80	435.08	111.61	
R1-D142	Gouamir	I-6	Eavporite		-0.47	-7.43	396586.49	1604.23	1361.16	253.52	284.41	107.51	130.65	
R1-D143	Gouamir	I-6	Eavporite		-0.34	-8.45	392403.39	3833.04	2217.39	262.15	295.46	705.61	136.17	
R1-D144	Gouamir	I-6	Eavporite		-0.28	-8.17	387963.10	5786.08	3734.74	288.95	387.83	1158.33	151.86	milled chips
R1-D148	Gouamir	I-6	Eavporite		-0.29	-7.16	386973.21	2401.24	4146.07	430.02	529.91	4206.82	769.76	
R1-D149	Gouamir	I-6	Eavporite		-0.26	-6.8	394401.96	1673.39	2970.91	289.52	439.24	323.93	326.37	
R1-D150	Gouamir	I-6	Eavporite		-0.25	-7.5	374741.32	8868.19	6655.25	328.06	619.81	7000.97	472.68	
R1-D151	Gouamir	I-6	Eavporite		-0.21	-7.57	390912.67	2110.56	3425.84	464.27	426.71	1828.15	466.69	
R1-D152	Gouamir	I-6	Eavporite		-0.02	-8.16	386914.49	6064.89	4657.08	431.80	497.49	816.33	127.20	
R1-D154	Gouamir	I-6	Eavporite		-0.25	-7.93	391668.46	2716.55	3678.84	435.51	488.94	502.51	225.20	
R1-D155	Gouamir	I-6	Eavporite		-0.18	-7.72	390398.31	2727.45	4051.44	538.27	493.37	1384.61	570.20	milled chips
R1-D156	Gouamir	I-6	Eavporite		-0.31	-7.27	370623.99	15067.90	10403.28	304.97	809.93	261.67	214.72	milled chips
R1-D157	Gouamir	I-6	Eavporite		-0.43	-6.86	386760.08	2377.27	3155.27	264.37	490.44	6633.30	498.81	
R1-D158	Gouamir	I-6	Eavporite		-0.27	-7.31	382123.31	8673.01	6521.82	309.46	575.95	456.96	328.61	
R1-D159	Gouamir	I-6	Eavporite				377072.78	11071.25	8302.83	325.63	659.31	1110.09	201.23	
R1-D161	Gouamir	I-6	Eavporite		-1.33	-11.71	365164.47	17578.63	11896.50	274.76	737.47	795.11	245.86	
R1-D162	Gouamir	I-6	Eavporite		-0.29	-7.47	375954.05	11710.39	8640.91	342.41	584.72	793.89	245.48	milled chips
R1-D165	Gouamir	I-6	Eavporite		-0.09	-8.42	387740.52	4957.16	5095.48	150.36	661.81	480.99	426.53	milled chips
R2-D2-2			Evaporite		-0.68	-8.43	276694.3479	75292.95471	24233.3523	59.59342691	602.1162835	711.77	105.11	
R2-D2-3			Evaporite		-0.89	-9.5	368970.5779	20142.26374	5891.11642	80.64246588	195.6229857	595.42	46.94	
R2-D2-4			Evaporite		-0.98	-9.21	372805.3973	18161.80542	4645.25959	113.0310167	162.9178772	259.39	211.75	
R2-D2-5			Evaporite		-0.73	-8.27	364168.1036	25123.70724	4773.8797	103.8252808	166.2764158	152.56	156.31	
R2-D2-7			Evaporite		-0.38	-10.08	339580.4415	43661.92062	5856.34123	79.75997399	184.4970132	164.49	60.73	
R2-D2-10			Evaporite				318193.0345	59649.11891	6234.93554	84.66455252	175.7388486	166.60	53.57	
R2-D2-12			Evaporite		-0.84	-10.16	395124.4147	3178.726715	831.671359	216.9418835	67.34910713	262.26	95.20	
R2-D2-13			Evaporite		-0.44	-7.97	305519.9401	59504.25519	8474.32229	77.97436152	243.2779405	9789.47	137.44	
R2-D2-6			Non-evaporite				373329.8061	14818.46341	2712.4766	177.4057274	111.6603397	5681.39	166.97	
R2-D2-8			Non-evaporite				323353.9658	41819.16931	6352.26451	106.1883181	204.0442305	17147.63	211.91	
R2-D2-19			Non-evaporite				386744.8406	9347.707844	1191.75971	105.5800063	87.2776292	738.70	198.07	

APPENDIX 2

Calculate the amount of Ca and SO4 in a hypothetical gypsum

1 mole of Ca for every 1 mole of SO4

	Atomic Weight		X g/136g	into mg
CaSO4	136	Ca	0.29	294.12
		SO4	0.71	705.88

Because the Atar Group samples are Carbonate, need to know how much CO3 is in a carbonate

CaCO3	100	Ca	0.4	400
		CO3	0.6	600

Using the [trace element] found in the literature (Fontes and Matary, 1993); Calculate the elemental ratios for [X/Ca] liquid

Modern Seawater (Gyp Saturated)		
Element	mmol/kg	mol/kg
Na	1714.00	0.49
K	39.20	0.01
Mg	194.00	0.06
Sr	0.26	0.00
SO4	110.00	0.03
Ca	40.10	0.01

Elemental Ratios	
Element	(mol/kg)/(mol/kg)
Na/Ca	42.74
K/Ca	0.98
Mg/Ca	4.84
Sr/Ca	0.01
SO4/Ca	2.74

Use the Dx (found in the literature) to determine the [X/Ca]rock in a modern gypsum

Distribution Coefficients for Gypsum		
Dx	Low Estimate (mol/m	High Estimate (mol/mol)
Na/Ca	0.000010	0.000310
K/Ca	0.000010	0.000340
Mg/Ca	0.000001	0.000043
Sr/Ca	0.150000	0.680000

Calculate [X/Ca] in gypsum:

[X/Ca] in gyp	[(mol/kg)/(m	[(g/kg)/(g/kg	[(mg/kg)/(mg/k	Amount of X	ppm
Na/Ca	0.01325	0.00762	0.00762	Na	2240.0
K/Ca	0.00033	0.00032	0.00032	K	95.3
Mg/Ca	0.00021	0.00012	0.00012	Mg	36.7
Sr/Ca	0.00441	0.00959	0.00959	Sr	2819.3
SO4/Ca	No published Dx			SO4	n/a

** I used the high Dx value to obtain the maximum [element] in a hypothetical gypusm

Calcite Distribution Coefficient		
Dx	Low Estimat	High Estimate (mol/mol)
Na/Ca		0.00015
K/Ca		0.0003
Mg/Ca	0.019	0.21
Sr/Ca	0.02	0.24
SO4/Ca		0.00018

Calculate to water-rock ratios for various waters:

Measured Values

Sodium Concentrations		
Trace Element Depleted Samples (N=32		
	[Na] ppm	[Na/Ca]
Average	707.79	0.0019
High	1825.56	0.0049
Low	159.78	0.0004
Standard Devi	396.77	0.0148
Trace Element Enriched Samples (N=6)		
	[Na] ppm	[Na/Ca]
Average	6636.99	0.0092
High	9775.66	0.0215
Low	4199.48	0.0007
Standard Devi	2113.01	0.0085

Potassium Concentrations		
Trace Element Depleted Samples (N=32		
	[K] ppm	[K/Cl]
Average	172.96	0.00046
High	768.42	0.00199
Low	46.91	0.00013
Standard Devi	142.31	0.00037
Trace Element Enriched Samples (N=6)		
	[K] ppm	[K/Ca]
Average	533.33	0.0014
High	768.41	0.002
Low	426.53	0.0011
Standard Devi	124.54	0.0003

For Modern SW

	In liquid (ppm/ppm) Using the high Dx values in gypsum																					
Element	[X] mod SW	[X]gypsum	0.1:1	0.25:1	0.50:1	0.75:1	1:1	1:2	1:3	1:4	1:5	1:10	1:20	1:30	1:40	1:50	1:60	1:70	1:80	1:90	1:100
Na	11154.26	2239.975736	33554.0	20114.2	15634.2	14133.4	13394.2	12274.2	11900.9	11714.3	11602.3	11378.3	11266.3	11228.9	11210.3	11199.1	11191.6	11186.3	11182.3	11179.1	11176.7
K	414.44	95.27359601	1367.2	795.5	605.0	541.2	509.7	462.1	446.2	438.3	433.5	424.0	419.2	417.6	416.8	416.3	416.0	415.8	415.6	415.5	415.4
Mg	1339.2	36.6964788	1706.2	1486.0	1412.6	1388.0	1375.9	1357.5	1351.4	1348.4	1346.5	1342.9	1341.0	1340.4	1340.1	1339.9	1339.8	1339.7	1339.7	1339.6	1339.6
Sr	8.29	2819.320698	28201.5	11285.6	5646.9	3758.0	2827.6	1418.0	948.1	713.1	572.2	290.2	149.3	102.3	78.8	64.7	55.3	48.6	43.5	39.6	36.5
SO4	2804.42	705882	7061624.4	2826332.4	1414568.4	941627.5	708686.4	355745.4	238098.4	179274.9	143980.8	73392.6	38098.5	26333.8	20451.5	16922.1	14569.1	12888.4	11627.9	10647.6	9863.2
Ca	424.82	294118	2941604.8	1176896.8	588660.8	391601.8	294542.8	147483.8	98464.2	73954.3	59248.4	29836.6	15130.7	10228.8	7777.8	6307.2	5326.8	4626.5	4101.3	3692.8	3366.0

[X/Ca] in liquid (PPM/PPM)																			
Ratios	0.1:1	0.25:1	0.5:1	0.75:1	1:1	2:1	3:1	4:1	5:1	10:1	20:1	30:1	40:1	50:1	60:1	70:1	80:1	90:1	100:1
Na/Ca	0.011407	0.017091	0.026559	0.036091	0.045475	0.08322437	0.120865494	0.158399	0.19582387	0.381352096	0.744595022	1.097780491	1.4413205	1.77560487	2.101002655	2.41786358	2.72651923	3.027284268	3.320457444
K/Ca	0.000465	0.000676	0.001028	0.001382	0.001731	0.00313307	0.004531577	0.005926	0.00731656	0.014209631	0.027705468	0.040827633	0.0535914	0.06601135	0.078101099	0.08987367	0.10134139	0.112515935	0.123408418
Mg/Ca	0.000580	0.001263	0.002400	0.003544	0.004671	0.00920473	0.013725118	0.018233	0.02272701	0.045007432	0.088629941	0.131044632	0.172301	0.2124458	0.251523421	0.28957583	0.32664285	0.362762279	0.397969984
Sr/Ca	0.009587	0.009589	0.009593	0.009596	0.009600	0.00961428	0.009628515	0.009643	0.00965687	0.009727042	0.009864437	0.009998027	0.010128	0.01025441	0.010377491	0.01049734	0.01061409	0.010727851	0.010838742
SO4/Ca	2.400603	2.401512	2.403028	2.404554	2.406056	2.41209795	2.418122859	2.424130	2.43012084	2.459816829	2.517958167	2.57448969	2.6294773	2.68298352	2.735067295	2.78578464	2.83518864	2.883329652	2.930255496

[X/Ca] in liquid (mol/kg)/(mol/kg)																			
Ratios	0.1:1	0.25:1	0.5:1	0.75:1	1:1	2:1	3:1	4:1	5:1	10:1	20:1	30:1	40:1	50:1	60:1	70:1	80:1	90:1	100:1
Na/Ca	0.019838	0.029723	0.046189	0.062768	0.079086372	0.14473803	0.21020086	0.275476	0.34056326	0.663221036	1.294947864	1.909183463	2.5066444	3.08800847	3.653917661	4.20498013	4.74177258	5.264842206	5.774708599
K/Ca	0.00048	0.00069	0.00105	0.00142	0.001774897	0.0032134	0.004647771	0.00608	0.00750417	0.01457398	0.028415865	0.041874495	0.0549656	0.06770395	0.080103691	0.09217812	0.10393988	0.115400959	0.126572737
Mg/Ca	0.00097	0.00210	0.00400	0.00591	0.007785492	0.01534121	0.022875197	0.03039	0.03787835	0.075012387	0.147716569	0.21840772	0.2871683	0.35407634	0.419205702	0.48262638	0.54440476	0.604603799	0.663283306
Sr/Ca	0.00441	0.00441	0.00441	0.00441	0.004413793	0.00442036	0.004426903	0.00443	0.00443994	0.004472203	0.004535373	0.004596794	0.0046565	0.00471467	0.00477126	0.00482636	0.00488004	0.004932345	0.00498333
SO4/Ca	1.00025	1.00063	1.00126	1.00190	1.002523193	1.00504081	1.007551191	1.01005	1.01255035	1.024923679	1.049149236	1.072704038	1.0956156	1.1179098	1.139611373	1.1607436	1.1813286	1.201387355	1.22093979

[X/Ca] (mol/mol) in calcite from dissolving gypsum + water (used high distribution coefficients)																			
Ratios	0.1:1	0.25:1	0.5:1	0.75:1	1:1	2:1	3:1	4:1	5:1	10:1	20:1	30:1	40:1	50:1	60:1	70:1	80:1	90:1	100:1
Na/Ca	0.000003	0.000004	0.000007	0.000009	0.000012	0.000022	0.000032	0.000041	0.000051	0.000099	0.000194	0.000286	0.000376	0.000463	0.000548	0.000631	0.000711	0.000790	0.000866
K/Ca	0.000000	0.000000	0.000000	0.000000	0.000001	0.000001	0.000001	0.000002	0.000002	0.000004	0.000009	0.000013	0.000016	0.000020	0.000024	0.000028	0.000031	0.000035	0.000038
Mg/Ca	0.000203	0.000442	0.000840	0.001241	0.001635	0.003222	0.004804	0.006381	0.007954	0.015753	0.031020	0.045866	0.060305	0.074356	0.088033	0.101352	0.114325	0.126967	0.139289
Sr/Ca	0.001058	0.001058	0.001059	0.001059	0.001059	0.001061	0.001062	0.001064	0.001066	0.001073	0.001088	0.001103	0.001118	0.001132	0.001145	0.001158	0.001171	0.001184	0.001196
SO4/Ca	0.000180	0.000180	0.000180	0.000180	0.000180	0.000181	0.000181	0.000182	0.000182	0.000184	0.000189	0.000193	0.000197	0.000201	0.000205	0.000209	0.000213	0.000216	0.000220

[X/Ca] (ppm/ppm) in calcite from dissolving gypsum + water (used high distribution coefficients)																			
Ratios	0.1:1	0.25:1	0.5:1	0.75:1	1:1	2:1	3:1	4:1	5:1	10:1	20:1	30:1	40:1	50:1	60:1	70:1	80:1	90:1	100:1
Na/Ca	0.0000017110	0.0000026	0.0000040	0.0000054	0.000007	0.000012	0.000018	0.000024	0.000029	0.000057	0.000112	0.000165	0.000216	0.000266	0.000315	0.000363	0.000409	0.000454	0.000498
K/Ca	0.0000001394	0.0000002	0.0000003	0.0000004	0.000001	0.000001	0.000001	0.000002	0.000002	0.000004	0.000008	0.000012	0.000016	0.000020	0.000023	0.000027	0.000030	0.000034	0.000037
Mg/Ca	0.0001218024	0.0006349	0.0006351	0.0006354	0.000636	0.000637	0.000637	0.000638	0.000639	0.000644	0.000653	0.000662	0.000671	0.000679	0.000687	0.000695	0.000703	0.000710	0.000718
Sr/Ca	0.0023009071	0.0023014	0.0023023	0.0023031	0.002304	0.002307	0.002311	0.002314	0.002318	0.002334	0.002367	0.002400	0.002431	0.002461	0.002491	0.002519	0.002547	0.002575	0.002601
SO4/Ca	0.0004321085	0.0004323	0.0004325	0.0004328	0.000433	0.000434	0.000435	0.000436	0.000437	0.000443	0.000453	0.000463	0.000473	0.000483	0.000492	0.000501	0.000510	0.000519	0.000527

For Fresh Water:

	In liquid (ppm/ppm) Using the high Dx values in gypsum																				
Element	[X] mod FW	[X]gypsum	0.1:1	0.25:1	0.50:1	0.75:1	1:1	1:2	1:3	1:4	1:5	1:10	1:20	1:30	1:40	1:50	1:60	1:70	1:80	1:90	1:100
Na	6.1	2239.975736	22405.9	8966.0	4486.1	2985.3	2246.1	1126.1	752.8	566.1	454.1	230.1	118.1	80.8	62.1	50.9	43.4	38.1	34.1	31.0	28.5
K	2	95.27359601	954.7	383.1	192.5	128.7	97.3	49.6	33.8	25.8	21.1	11.5	6.8	5.2	4.4	3.9	3.6	3.4	3.2	3.1	3.0
Mg	12.2	36.6964788	379.2	159.0	85.6	61.0	48.9	30.5	24.4	21.4	19.5	15.9	14.0	13.4	13.1	12.9	12.8	12.7	12.7	12.6	12.6
Sr	0.11	2819.320698	28193.3	11277.4	5638.8	3749.8	2819.4	1409.8	939.9	704.9	564.0	282.0	141.1	94.1	70.6	56.5	47.1	40.4	35.4	31.4	28.3
SO4	2804.42	705882	7061624.4	2826332.4	1414568.4	941627.5	708686.4	355745.4	238098.4	179274.9	143980.8	73392.6	38098.5	26333.8	20451.5	16922.1	14569.1	12888.4	11627.9	10647.6	9863.2
Ca	424.82	294118	2941604.8	1176896.8	588660.8	391601.8	294542.8	147483.8	98464.2	73954.3	59248.4	29836.6	15130.7	10228.8	7777.8	6307.2	5326.8	4626.5	4101.3	3692.8	3366.0

[X/Ca] in liquid (PPM/PPM)																			
Ratios	0.1:1	0.25:1	0.5:1	0.75:1	1:1	2:1	3:1	4:1	5:1	10:1	20:1	30:1	40:1	50:1	60:1	70:1	80:1	90:1	100:1
Na/Ca	0.007617	0.007618	0.007621	0.007623	0.007626	0.00763533	0.007645001	0.007655	0.00766426	0.007711918	0.007805232	0.007895963	0.0079842	0.00807009	0.008153683	0.00823508	0.00831437	0.008391637	0.008466951
K/Ca	0.000325	0.000326	0.000327	0.000329	0.000330	0.00033656	0.000342844	0.000349	0.00035536	0.000386349	0.000447016	0.000506004	0.0005634	0.00061921	0.000673557	0.00072648	0.00077803	0.00082826	0.000877224
Mg/Ca	0.000129	0.000135	0.000145	0.000156	0.000166	0.00020713	0.000248133	0.000289	0.00032979	0.000531885	0.000927571	0.001312302	0.0016865	0.00205067	0.002405129	0.00275029	0.00308651	0.003414143	0.003733501
Sr/Ca	0.009584	0.009582	0.009579	0.009576	0.009572	0.00955881	0.009545439	0.009532	0.0095188	0.009452883	0.009323815	0.009198321	0.0090763	0.00895748	0.008841856	0.00872927	0.0086196	0.008512729	0.008408558
SO4/Ca	2.400603	2.401512	2.403028	2.404554	2.406056	2.41209795	2.418122859	2.424130	2.43012084	2.459816829	2.517958167	2.57448969	2.6294773	2.68298352	2.735067295	2.78578464	2.83518864	2.883329652	2.930255496

[X/Ca] in liquid (mol/kg)/(mol/kg)																			
Ratios	0.1:1	0.25:1	0.5:1	0.75:1	1:1	2:1	3:1	4:1	5:1	10:1	20:1	30:1	40:1	50:1	60:1	70:1	80:1	90:1	100:1
Na/Ca	0.013247	0.013249	0.013254	0.013258	0.013261972	0.01327884	0.013295654	0.013312	0.01332914	0.013412032	0.013574317	0.01373211	0.0138856	0.01403494	0.014180318	0.01432188	0.01445978	0.014594152	0.014725132
K/Ca	0.00033	0.00033	0.00034	0.00034	0.000338721	0.00034519	0.000351635	0.00036	0.00036448	0.000396256	0.000458478	0.000518978	0.0005778	0.00063509	0.000690827	0.0007451	0.00079798	0.000849497	0.000899717
Mg/Ca	0.00021	0.00023	0.00024	0.00026	0.00027668	0.00034522	0.000413554	0.00048	0.00054964	0.000886475	0.001545952	0.0021871	0.0028109	0.00341778	0.004008548	0.00458382	0.00514419	0.005690238	0.006222502
Sr/Ca	0.00441	0.00441	0.00440	0.00440	0.004401024	0.00439486	0.004388708	0.00438	0.00437646	0.004346153	0.004286812	0.004229113	0.004173	0.00411838	0.004065221	0.00401346	0.00396303	0.003913898	0.003866004
SO4/Ca	1.00025	1.00063	1.00126	1.00190	1.002523193	1.00504081	1.007551191	1.01005	1.01255035	1.024923679	1.049149236	1.072704038	1.0956156	1.1179098	1.139611373	1.1607436	1.1813286	1.201387355	1.22093979

[X/Ca] (mol/mol) in calcite from dissolving gypsum + water (used high distribution coefficients)																			
Ratios	0.1:1	0.25:1	0.5:1	0.75:1	1:1	2:1	3:1	4:1	5:1	10:1	20:1	30:1	40:1	50:1	60:1	70:1	80:1	90:1	100:1
Na/Ca	0.000002	0.000002	0.000002	0.000002	0.000002	0.000002	0.000002	0.000002	0.000002	0.000002	0.000002	0.000002	0.000002	0.000002	0.000002	0.000002	0.000002	0.000002	0.000002
K/Ca	0.000000	0.000000	0.000000	0.000000	0.000000	0.000000	0.000000	0.000000	0.000000	0.000000	0.000000	0.000000	0.000000	0.000000	0.000000	0.000000	0.000000	0.000000	0.000000
Mg/Ca	0.000045	0.000047	0.000051	0.000055	0.000058	0.000072	0.000087	0.000101	0.000115	0.000186	0.000325	0.000459	0.000590	0.000718	0.000842	0.000963	0.001080	0.001195	0.001307
Sr/Ca	0.001058	0.001057	0.001057	0.001057	0.001056	0.001055	0.001053	0.001052	0.001050	0.001043	0.001029	0.001015	0.001002	0.000988	0.000976	0.000963	0.000951	0.000939	0.000928
SO4/Ca	0.000180	0.000180	0.000180	0.000180	0.000180	0.000181	0.000181	0.000182	0.000182	0.000184	0.000189	0.000193	0.000197	0.000201	0.000205	0.000209	0.000213	0.000216	0.000220

[X/Ca] (ppm/ppm) in calcite from dissolving gypsum + water (used high distribution coefficients)																			
Ratios	0.1:1	0.25:1	0.5:1	0.75:1	1:1	2:1	3:1	4:1	5:1	10:1	20:1	30:1	40:1	50:1	60:1	70:1	80:1	90:1	100:1
Na/Ca	0.0000011425	0.0000011	0.0000011	0.0000011	0.000001	0.000001	0.000001	0.000001	0.000001	0.000001	0.000001	0.000001	0.000001	0.000001	0.000001	0.000001	0.000001	0.000001	0.000001
K/Ca	0.0000000974	0.0000001	0.0000001	0.0000001	0.000000	0.000000	0.000000	0.000000	0.000000	0.000000	0.000000	0.000000	0.000000	0.000000	0.000000	0.000000	0.000000	0.000000	0.000000
Mg/Ca	0.0000270684	0.0006344	0.0006342	0.0006340	0.000634	0.000633	0.000632	0.000631	0.000630	0.000626	0.000617	0.000609	0.000601	0.000593	0.000585	0.000578	0.000571	0.000564	0.000557
Sr/Ca	0.0023002397	0.0022998	0.0022989	0.0022981	0.002297	0.002294	0.002291	0.002288	0.002285	0.002269	0.002238	0.002208	0.002178	0.002150	0.002122	0.002095	0.002069	0.002043	0.002018
SO4/Ca	0.0004321085	0.0004323	0.0004325	0.0004328	0.000433	0.000434	0.000435	0.000436	0.000437	0.000443	0.000453	0.000463	0.000473	0.000483	0.000492	0.000501	0.000510	0.000519	0.000527

For SW at Gypsum Saturation

	In liquid (ppm/ppm) Using the high Dx values in gypsum																				
Element	[X] mod SW gyp	[X]gypsum	0.1:1	0.25:1	0.50:1	0.75:1	1:1	1:2	1:3	1:4	1:5	1:10	1:20	1:30	1:40	1:50	1:60	1:70	1:80	1:90	1:100
Na	39403.2	2239.975736	61803.0	48363.1	43883.2	42382.4	41643.2	40523.2	40149.9	39963.2	39851.2	39627.2	39515.2	39477.9	39459.2	39448.0	39440.5	39435.2	39431.2	39428.1	39425.6
K	1532.6	95.27359601	2485.3	1913.7	1723.1	1659.3	1627.9	1580.2	1564.4	1556.4	1551.7	1542.1	1537.4	1535.8	1535.0	1534.5	1534.2	1534.0	1533.8	1533.7	1533.6
Mg	4715.2	36.6964788	5082.2	4862.0	4788.6	4764.0	4751.9	4733.5	4727.4	4724.4	4722.5	4718.9	4717.0	4716.4	4716.1	4715.9	4715.8	4715.7	4715.7	4715.6	4715.6
Sr	23.1	2819.320698	28216.3	11300.4	5661.7	3772.8	2842.4	1432.8	962.9	727.9	587.0	305.0	164.1	117.1	93.6	79.5	70.1	63.4	58.3	54.4	51.3
SO4	10564.6	705882	7069384.6	2834092.6	1422328.6	949387.7	716446.6	363505.6	245858.6	187035.1	151741.0	81152.8	45858.7	34094.0	28211.7	24682.2	22329.3	20648.6	19388.1	18407.7	17623.4
Ca	1607.1	294118	2942787.1	1178079.1	589843.1	392784.0	295725.1	148666.1	99646.4	75136.6	60430.7	31018.9	16313.0	11411.0	8960.1	7489.5	6509.1	5808.8	5283.6	4875.1	4548.3

[X/Ca] in liquid (PPM/PPM)																			
Ratios	0.1:1	0.25:1	0.5:1	0.75:1	1:1	2:1	3:1	4:1	5:1	10:1	20:1	30:1	40:1	50:1	60:1	70:1	80:1	90:1	100:1
Na/Ca	0.021002	0.041053	0.074398	0.107902	0.140817	0.27257854	0.402923188	0.531874	0.65945281	1.277517822	2.422313418	3.459622341	4.4039039	5.26713535	6.059322319	6.78888869	7.46297719	8.087684016	8.668243766
K/Ca	0.000845	0.001624	0.002921	0.004224	0.005505	0.01062944	0.015699085	0.020715	0.0256766	0.049715733	0.094241628	0.134586916	0.171314	0.20488867	0.235700135	0.26407603	0.29029415	0.314591616	0.337172016
Mg/Ca	0.001727	0.004127	0.008118	0.012129	0.016069	0.03184013	0.047442061	0.062877	0.07814802	0.152128852	0.289158023	0.413321307	0.5263495	0.6296761	0.724498895	0.81182617	0.89251287	0.967288719	1.03678027
Sr/Ca	0.009588	0.009592	0.009599	0.009605	0.009612	0.00963744	0.0096629	0.009688	0.00971301	0.009833749	0.01005738	0.010260014	0.0104445	0.0106131	0.010767854	0.01091037	0.01104205	0.011164086	0.011277495
SO4/Ca	2.402275	2.405690	2.411368	2.417073	2.422678	2.44511425	2.467309584	2.489268	2.51099193	2.616237197	2.811175136	2.987810043	3.1486041	3.29559675	3.430491827	3.55472376	3.66950881	3.775885057	3.874743859

[X/Ca] in liquid (mol/kg)/(mol/kg)																			
Ratios	0.1:1	0.25:1	0.5:1	0.75:1	1:1	2:1	3:1	4:1	5:1	10:1	20:1	30:1	40:1	50:1	60:1	70:1	80:1	90:1	100:1
Na/Ca	0.036524	0.071396	0.129388	0.187656	0.24489945	0.47404963	0.700735979	0.924998	1.14687446	2.221770125	4.212718988	6.016734507	7.6589634	9.16023539	10.53795186	11.8067629	12.9790908	14.06553742	15.07520655
K/Ca	0.00087	0.00167	0.00300	0.00433	0.005645831	0.01090199	0.016101626	0.02125	0.02633497	0.050990496	0.09665808	0.138037863	0.1757066	0.21014222	0.241743728	0.27084721	0.29773759	0.322658068	0.345817452
Mg/Ca	0.00288	0.00688	0.01353	0.02021	0.026781046	0.05306689	0.079070102	0.10480	0.13024669	0.253548087	0.481930038	0.688868846	0.8772491	1.04946016	1.207498158	1.35304361	1.48752146	1.612147865	1.727967116
Sr/Ca	0.00441	0.00441	0.00441	0.00442	0.004419172	0.00443101	0.004442713	0.00445	0.00446575	0.004521264	0.004624083	0.004717248	0.0048021	0.00487959	0.004950737	0.00501626	0.00507681	0.005132913	0.005185055
SO4/Ca	1.00095	1.00237	1.00474	1.00711	1.009449034	1.01879761	1.02804566	1.03719	1.04624664	1.090098832	1.171322973	1.244920851	1.3119184	1.37316531	1.429371594	1.4811349	1.528962	1.57328544	1.614476608

[X/Ca] (mol/mol) in calcite from dissolving gypsum + water (used high distribution coefficients)																			
Ratios	0.1:1	0.25:1	0.5:1	0.75:1	1:1	2:1	3:1	4:1	5:1	10:1	20:1	30:1	40:1	50:1	60:1	70:1	80:1	90:1	100:1
Na/Ca	0.000005	0.000011	0.000019	0.000028	0.000037	0.000071	0.000105	0.000139	0.000172	0.000333	0.000632	0.000903	0.001149	0.001374	0.001581	0.001771	0.001947	0.002110	0.002261
K/Ca	0.000000	0.000000	0.000001	0.000001	0.000002	0.000003	0.000005	0.000006	0.000008	0.000015	0.000029	0.000041	0.000053	0.000063	0.000073	0.000081	0.000089	0.000097	0.000104
Mg/Ca	0.000604	0.001444	0.002841	0.004245	0.005624	0.011144	0.016605	0.022007	0.027352	0.053245	0.101205	0.144662	0.184222	0.220387	0.253575	0.284139	0.312380	0.338551	0.362873
Sr/Ca	0.001058	0.001058	0.001059	0.001060	0.001061	0.001063	0.001066	0.001069	0.001072	0.001085	0.001110	0.001132	0.001152	0.001171	0.001188	0.001204	0.001218	0.001232	0.001244
SO4/Ca	0.000180	0.000180	0.000181	0.000181	0.000182	0.000183	0.000185	0.000187	0.000188	0.000196	0.000211	0.000224	0.000236	0.000247	0.000257	0.000267	0.000275	0.000283	0.000291

[X/Ca] (ppm/ppm) in calcite from dissolving gypsum + water (used high distribution coefficients)																			
Ratios	0.1:1	0.25:1	0.5:1	0.75:1	1:1	2:1	3:1	4:1	5:1	10:1	20:1	30:1	40:1	50:1	60:1	70:1	80:1	90:1	100:1
Na/Ca	0.0000031502	0.0000062	0.0000112	0.0000162	0.000021	0.000041	0.000060	0.000080	0.000099	0.000192	0.000363	0.000519	0.000661	0.000790	0.000909	0.001018	0.001119	0.001213	0.001300
K/Ca	0.0000002534	0.0000005	0.0000009	0.0000013	0.000002	0.000003	0.000005	0.000006	0.000008	0.000015	0.000028	0.000040	0.000051	0.000061	0.000071	0.000079	0.000087	0.000094	0.000101
Mg/Ca	0.0003626680	0.0006351	0.0006355	0.0006359	0.000636	0.000638	0.000640	0.000641	0.000643	0.000651	0.000666	0.000679	0.000691	0.000703	0.000713	0.000722	0.000731	0.000739	0.000747
Sr/Ca	0.0023011905	0.0023021	0.0023037	0.0023053	0.002307	0.002313	0.002319	0.002325	0.002331	0.002360	0.002414	0.002462	0.002507	0.002547	0.002584	0.002618	0.002650	0.002679	0.002707
SO4/Ca	0.0004324095	0.0004330	0.0004340	0.0004351	0.000436	0.000440	0.000444	0.000448	0.000452	0.000471	0.000506	0.000538	0.000567	0.000593	0.000617	0.000640	0.000661	0.000680	0.000697

For SW at cf 7

	In liquid (ppm/ppm) Using the high Dx values in gypsum																					
Element	[X] mod SW cf 7	[X]gypsum	0.1:1	0.25:1	0.50:1	0.75:1	1:1	1:2	1:3	1:4	1:5	1:10	1:20	1:30	1:40	1:50	1:60	1:70	1:80	1:90	1:100
Na	89309.00	2239.975736	111708.8	98268.9	93789.0	92288.2	91549.0	90429.0	90055.7	89869.0	89757.0	89533.0	89421.0	89383.7	89365.0	89353.8	89346.3	89341.0	89337.0	89333.9	89331.4
K	3307.98	95.27359601	4260.7	3689.1	3498.5	3434.7	3403.3	3355.6	3339.7	3331.8	3327.0	3317.5	3312.7	3311.2	3310.4	3309.9	3309.6	3309.3	3309.2	3309.0	3308.9
Mg	10579.20	36.6964788	10946.2	10726.0	10652.6	10628.0	10615.9	10597.5	10591.4	10588.4	10586.5	10582.9	10581.0	10580.4	10580.1	10579.9	10579.8	10579.7	10579.7	10579.6	10579.6
Sr	N/A	2819.320698																			
SO4	22425.60	705882	7081245.6	2845953.6	1434189.6	961248.7	728307.6	375366.6	257719.6	198896.1	163602.0	93013.8	57719.7	45955.0	40072.7	36543.2	34190.3	32509.6	31249.1	30268.7	29484.4
Ca	3392.80	294118	2944572.8	1179864.8	591628.8	394569.7	297510.8	150451.8	101432.1	76922.3	62216.4	32804.6	18098.7	13196.7	10745.8	9275.2	8294.8	7594.5	7069.3	6660.8	6334.0

[X/Ca] in liquid (PPM/PPM)																		
Ratios	0.1:1	0.25:1	0.5:1	0.75:1	1:1	2:1	3:1	4:1	5:1	10:1	20:1	30:1	40:1	50:1	60:1	70:1	80:1	90:1	100:1
Na/Ca	0.037937	0.083288	0.158527	0.233896	0.307716	0.60104956	0.887841512	1.168309	1.44265813	2.729281795	4.940741533	6.773166025	8.316311	9.63366664	10.77141004	11.7639302	12.6373638	13.4119305	14.10351781
K/Ca	0.001447	0.003127	0.005913	0.008705	0.011439	0.0223036	0.032925837	0.043314	0.0534752	0.101129334	0.183037659	0.250907229	0.3080624	0.35685481	0.398994695	0.43575578	0.46810612	0.496794625	0.522409723
Mg/Ca	0.003717	0.009091	0.018006	0.026936	0.035682	0.07043816	0.104418904	0.137650	0.17015673	0.322603222	0.584629549	0.801745625	0.9845862	1.14067401	1.275480316	1.39307975	1.49656913	1.588344198	1.670287397
Sr/Ca																			
SO4/Ca	2.404847	2.412101	2.424138	2.436195	2.448004	2.49492927	2.540808238	2.585675	2.62956391	2.835388939	3.189162758	3.482301176	3.7291627	3.939904	4.12191221	4.28068862	4.4204144	4.544324153	4.654959441

[X/Ca] in liquid (mol/kg)/(mol/kg)																		
Ratios	0.1:1	0.25:1	0.5:1	0.75:1	1:1	2:1	3:1	4:1	5:1	10:1	20:1	30:1	40:1	50:1	60:1	70:1	80:1	90:1	100:1
Na/Ca	0.065978	0.144849	0.275699	0.406775	0.535159093	1.04530358	1.544072194	2.031841	2.50897066	4.746577035	8.592593971	11.77941917	14.46315	16.7542029	18.73288702	20.459009	21.9780239	23.32509652	24.52785707
K/Ca	0.00148	0.00321	0.00607	0.00893	0.011732403	0.02287549	0.033770089	0.04442	0.05484636	0.103722394	0.187730932	0.257340747	0.3159615	0.36600493	0.409225328	0.44692901	0.48010885	0.509532948	0.535804844
Mg/Ca	0.00620	0.01515	0.03001	0.04489	0.05947065	0.11739694	0.174031506	0.22942	0.28359455	0.537672036	0.974382582	1.336242709	1.640977	1.90112335	2.125800526	2.32179958	2.49428188	2.64724033	2.783812328
Sr/Ca																			
SO4/Ca	1.00202	1.00504	1.01006	1.01508	1.020001627	1.03955386	1.058670099	1.07736	1.09565163	1.181412058	1.328817816	1.450958823	1.5538178	1.64162667	1.717463421	1.78362026	1.84183933	1.893468397	1.939566434

[X/Ca] (mol/mol) in calcite from dissolving gypsum + water (used high distribution coefficients)																		
Ratios	0.1:1	0.25:1	0.5:1	0.75:1	1:1	2:1	3:1	4:1	5:1	10:1	20:1	30:1	40:1	50:1	60:1	70:1	80:1	90:1	100:1
Na/Ca	0.000010	0.000022	0.000041	0.000061	0.000080	0.000157	0.000232	0.000305	0.000376	0.000712	0.001289	0.001767	0.002169	0.002513	0.002810	0.003069	0.003297	0.003499	0.003679
K/Ca	0.000000	0.000001	0.000002	0.000003	0.000004	0.000007	0.000010	0.000013	0.000016	0.000031	0.000056	0.000077	0.000095	0.000110	0.000123	0.000134	0.000144	0.000153	0.000161
Mg/Ca	0.001301	0.003182	0.006302	0.009427	0.012489	0.024653	0.036547	0.048178	0.059555	0.112911	0.204620	0.280611	0.344605	0.399236	0.446418	0.487578	0.523799	0.555920	0.584601
Sr/Ca																			
SO4/Ca	0.000180	0.000181	0.000182	0.000183	0.000184	0.000187	0.000191	0.000194	0.000197	0.000213	0.000239	0.000261	0.000280	0.000295	0.000309	0.000321	0.000332	0.000341	0.000349

[X/Ca] (ppm/ppm) in calcite from dissolving gypsum + water (used high distribution coefficients)																			
Ratios	0.1:1	0.25:1	0.5:1	0.75:1	1:1	2:1	3:1	4:1	5:1	10:1	20:1	30:1	40:1	50:1	60:1	70:1	80:1	90:1	100:1
Na/Ca	0.0000056906	0.0000125	0.0000238	0.0000351	0.000046	0.000090	0.000133	0.000175	0.000216	0.000409	0.000741	0.001016	0.001247	0.001445	0.001616	0.001765	0.001896	0.002012	0.002116
K/Ca	0.0000004341	0.0000009	0.0000018	0.0000026	0.000003	0.000007	0.000010	0.000013	0.000016	0.000030	0.000055	0.000075	0.000092	0.000107	0.000120	0.000131	0.000140	0.000149	0.000157
Mg/Ca	0.0007806547	0.0000000	0.0000000	0.0000000	0.000000	0.000000	0.000000	0.000000	0.000000	0.000000	0.000000	0.000000	0.000000	0.000000	0.000000	0.000000	0.000000	0.000000	0.000000
Sr/Ca																			
SO4/Ca	0.0004328724	0.0004342	0.0004363	0.0004385	0.000441	0.000449	0.000457	0.000465	0.000473	0.000510	0.000574	0.000627	0.000671	0.000709	0.000742	0.000771	0.000796	0.000818	0.000838

For SW at halite saturation

	In liquid (ppm/ppm) Using the high Dx values in gypsum																					
Element	[X] mod SW cf 10	[X]gypsum	0.1:1	0.25:1	0.50:1	0.75:1	1:1	1:2	1:3	1:4	1:5	1:10	1:20	1:30	1:40	1:50	1:60	1:70	1:80	1:90	1:100	
Na	106168.00	2239.975736	128567.8	115127.9	110648.0	109147.2	108408.0	107288.0	106914.7	106728.0	106616.0	106392.0	106280.0	106242.7	106224.0	106212.8	106205.3	106200.0	106196.0	106192.9	106190.4	
K	4027.10	95.27359601	4979.8	4408.2	4217.6	4153.8	4122.4	4074.7	4058.9	4050.9	4046.2	4036.6	4031.9	4030.3	4029.5	4029.0	4028.7	4028.5	4028.3	4028.2	4028.1	
Mg	14947.60	36.6964788	15314.6	15094.4	15021.0	14996.4	14984.3	14965.9	14959.8	14956.8	14954.9	14951.3	14949.4	14948.8	14948.5	14948.3	14948.2	14948.1	14948.1	14948.0	14948.0	
Sr	39.87	2819.320698	28233.1	11317.2	5678.5	3789.6	2859.2	1449.5	979.6	744.7	603.7	321.8	180.8	133.8	110.4	96.3	86.9	80.1	75.1	71.2	68.1	
SO4	21321.30	705882	7080141.3	2844849.3	1433085.3	960144.4	727203.3	374262.3	256615.3	197791.8	162497.7	91909.5	56615.4	44850.7	38968.4	35438.9	33086.0	31405.3	30144.8	29164.4	28380.1	
Ca	501.00	294118	2941681.0	1176973.0	588737.0	391677.9	294619.0	147560.0	98540.3	74030.5	59324.6	29912.8	15206.9	10304.9	7854.0	6383.4	5403.0	4702.7	4177.5	3769.0	3442.2	

[X/Ca] in liquid (PPM/PPM)

Ratios	0.1:1	0.25:1	0.5:1	0.75:1	1:1	2:1	3:1	4:1	5:1	10:1	20:1	30:1	40:1	50:1	60:1	70:1	80:1	90:1	100:1
Na/Ca	0.043706	0.097817	0.187941	0.278666	0.367960	0.72708043	1.084983732	1.441676	1.79716332	3.556738171	6.988932576	10.30988386	13.524914	16.6390114	19.65685511	22.5828401	25.4210976	28.17551466	30.84975212
K/Ca	0.001693	0.003745	0.007164	0.010605	0.013992	0.0276141	0.041189813	0.054720	0.06820366	0.13494649	0.265133833	0.391101588	0.5130516	0.63117316	0.74564367	0.85662987	0.96428846	1.068766873	1.17020398
Mg/Ca	0.005206	0.012825	0.025514	0.038288	0.050860	0.1014228	0.151814304	0.202035	0.25208664	0.49982849	0.983069187	1.450647251	1.903312	2.34176577	2.766667376	3.1786356	3.5782521	3.966064174	4.342587246
Sr/Ca	0.009598	0.009615	0.009645	0.009675	0.009705	0.00982333	0.009941549	0.010059	0.01017679	0.010758006	0.011891709	0.012988668	0.0140506	0.01507927	0.016076108	0.0170426	0.01798012	0.018889946	0.019773285
SO4/Ca	2.406835	2.417090	2.434169	2.451362	2.468284	2.53633979	2.60416513	2.671761	2.73912846	3.072580969	3.723007319	4.352352271	4.9616244	5.55176897	6.123672797	6.67816871	7.21603959	7.738022099	8.244809975

[X/Ca] in liquid (mol/kg)/(mol/kg)

Ratios	0.1:1	0.25:1	0.5:1	0.75:1	1:1	2:1	3:1	4:1	5:1	10:1	20:1	30:1	40:1	50:1	60:1	70:1	80:1	90:1	100:1
Na/Ca	0.076010	0.170116	0.326854	0.484636	0.639930249	1.2644877	1.886928229	2.507263	3.12550143	6.185631602	12.15466535	17.9302328	23.52159	28.937411	34.18583497	39.2745046	44.2106045	49.00089506	53.65174282
K/Ca	0.00174	0.00384	0.00735	0.01088	0.014350994	0.02832216	0.042245962	0.05612	0.06995247	0.138406656	0.271932136	0.401129833	0.5262068	0.64735708	0.764762738	0.87859474	0.9890138	1.096171152	1.20020921
Mg/Ca	0.00868	0.02137	0.04252	0.06381	0.08476652	0.169038	0.253023841	0.33673	0.42014441	0.833047483	1.638448645	2.417745419	3.1721867	3.90294295	4.611112293	5.297726	5.96375351	6.610106957	7.237645409
Sr/Ca	0.00441	0.00442	0.00443	0.00445	0.004461934	0.00451647	0.004570827	0.00462	0.00467899	0.004946209	0.005467453	0.005971801	0.0064601	0.006933	0.007391314	0.00783568	0.00826672	0.008685033	0.009091166
SO4/Ca	1.00285	1.00712	1.01424	1.02140	1.028451576	1.05680825	1.085068804	1.11323	1.14130352	1.28024207	1.55125305	1.813480113	2.0673435	2.31323707	2.551530332	2.78257029	3.00668316	3.224175874	3.43533749

[X/Ca] (mol/mol) in calcite from dissolving gypsum + water (used high distribution coefficients)

Ratios	0.1:1	0.25:1	0.5:1	0.75:1	1:1	2:1	3:1	4:1	5:1	10:1	20:1	30:1	40:1	50:1	60:1	70:1	80:1	90:1	100:1
Na/Ca	0.000011	0.000026	0.000049	0.000073	0.000096	0.000190	0.000283	0.000376	0.000469	0.000928	0.001823	0.002690	0.003528	0.004341	0.005128	0.005891	0.006632	0.007350	0.008048
K/Ca	0.000001	0.000001	0.000002	0.000003	0.000004	0.000008	0.000013	0.000017	0.000021	0.000042	0.000082	0.000120	0.000158	0.000194	0.000229	0.000264	0.000297	0.000329	0.000360
Mg/Ca	0.001822	0.004489	0.008930	0.013401	0.017801	0.035498	0.053135	0.070712	0.088230	0.174940	0.344074	0.507727	0.666159	0.819618	0.968334	1.112522	1.252388	1.388122	1.519906
Sr/Ca	0.001059	0.001061	0.001064	0.001068	0.001071	0.001084	0.001097	0.001110	0.001123	0.001187	0.001312	0.001433	0.001550	0.001664	0.001774	0.001881	0.001984	0.002084	0.002182
SO4/Ca	0.000181	0.000181	0.000183	0.000184	0.000185	0.000190	0.000195	0.000200	0.000205	0.000230	0.000279	0.000326	0.000372	0.000416	0.000459	0.000501	0.000541	0.000580	0.000618

[X/Ca] (ppm/ppm) in calcite from dissolving gypsum + water (used high distribution coefficients)

Ratios	0.1:1	0.25:1	0.5:1	0.75:1	1:1	2:1	3:1	4:1	5:1	10:1	20:1	30:1	40:1	50:1	60:1	70:1	80:1	90:1	100:1
Na/Ca	0.0000065558	0.0000147	0.0000282	0.0000418	0.000055	0.000109	0.000163	0.000216	0.000270	0.000534	0.001048	0.001546	0.002029	0.002496	0.002949	0.003387	0.003813	0.004226	0.004627
K/Ca	0.0000005079	0.0000011	0.0000021	0.0000032	0.000004	0.000008	0.000012	0.000016	0.000020	0.000040	0.000080	0.000117	0.000154	0.000189	0.000224	0.000257	0.000289	0.000321	0.000351
Mg/Ca	0.0010932724	0.0006366	0.0006386	0.0006406	0.000643	0.000650	0.000658	0.000666	0.000674	0.000712	0.000787	0.000860	0.000930	0.000998	0.001064	0.001128	0.001190	0.001251	0.001309
Sr/Ca	0.0023034240	0.0023077	0.0023149	0.0023221	0.002329	0.002358	0.002386	0.002414	0.002442	0.002582	0.002854	0.003117	0.003372	0.003619	0.003858	0.004090	0.004315	0.004534	0.004746
SO4/Ca	0.0004332303	0.0004351	0.0004382	0.0004412	0.000444	0.000457	0.000469	0.000481	0.000493	0.000553	0.000670	0.000783	0.000893	0.000999	0.001102	0.001202	0.001299	0.001393	0.001484

For SW at cf 20

			In liquid (ppm/ppm) Using the high Dx values in gypsum																	
Element	[X] mod SW cf 20	[X]gypsum	0.1:1	0.25:1	0.50:1	0.75:1	1:1	1:2	1:3	1:4	1:5	1:10	1:20	1:30	1:40	1:50	1:60	1:70	1:80	1:90	1:100
Na	223100.00	2239.975736	245499.8	232059.9	227580.0	226079.2	225340.0	224220.0	223846.7	223660.0	223548.0	223324.0	223212.0	223174.7	223156.0	223144.8	223137.3	223132.0	223128.0	223124.9	223122.4
K	8264.10	95.27359601	9216.8	8645.2	8454.6	8390.8	8359.4	8311.7	8295.9	8287.9	8283.2	8273.6	8268.9	8267.3	8266.5	8266.0	8265.7	8265.5	8265.3	8265.2	8265.1
Mg	26424.00	36.6964788	26791.0	26570.8	26497.4	26472.8	26460.7	26442.3	26436.2	26433.2	26431.3	26427.7	26425.8	26425.2	26424.9	26424.7	26424.6	26424.5	26424.5	26424.4	26424.4
Sr	N/A	2819.320698																			
SO4	56035.20	705882	7114855.2	2879563.2	1467799.2	994858.3	761917.2	408976.2	291329.2	232505.7	197211.6	126623.4	91329.3	79564.6	73682.3	70152.8	67799.9	66119.2	64858.7	63878.3	63094.0
Ca	8476.00	294118	2949656.0	1184948.0	596712.0	399652.9	302594.0	155535.0	106515.3	82005.5	67299.6	37887.8	23181.9	18279.9	15829.0	14358.4	13378.0	12677.7	12152.5	11744.0	11417.2

[X/Ca] in liquid (PPM/PPM)

Ratios	0.1:1	0.25:1	0.5:1	0.75:1	1:1	2:1	3:1	4:1	5:1	10:1	20:1	30:1	40:1	50:1	60:1	70:1	80:1	90:1	100:1
Na/Ca	0.083230	0.195840	0.381390	0.565689	0.744694	1.44160471	2.10154399	2.727378	3.32168386	5.894351152	9.628718905	12.20872428	14.097966	15.5411063	16.67946546	17.6003732	18.3607043	18.99908982	19.54268915
K/Ca	0.003125	0.007296	0.014169	0.020995	0.027626	0.05343966	0.077884166	0.101065	0.12307881	0.218371807	0.356694821	0.452259625	0.5222382	0.57569287	0.617858311	0.65196923	0.68013231	0.70377846	0.723913675
Mg/Ca	0.009083	0.022424	0.044406	0.066239	0.087446	0.17000899	0.248191799	0.322334	0.3927414	0.697524524	1.13993395	1.445586411	1.6694043	1.84037271	1.975233776	2.08433344	2.17440963	2.250038976	2.314439027
Sr/Ca																			
SO4/Ca	2.412097	2.430118	2.459812	2.489305	2.517952	2.62948018	2.735091661	2.835245	2.93035323	3.342062616	3.939681389	4.352565108	4.6549045	4.88585326	5.068027279	5.21540209	5.33707948	5.439241673	5.526235025

[X/Ca] in liquid (mol/kg)/(mol/kg)

Ratios	0.1:1	0.25:1	0.5:1	0.75:1	1:1	2:1	3:1	4:1	5:1	10:1	20:1	30:1	40:1	50:1	60:1	70:1	80:1	90:1	100:1
Na/Ca	0.144748	0.340591	0.663287	0.983807	1.295120227	2.50713862	3.654859113	4.743266	5.7768415	10.25104548	16.7455981	21.23256396	24.518202	27.028011	29.00776602	30.6093447	31.9316596	33.04189534	33.98728549
K/Ca	0.00320	0.00748	0.01453	0.02153	0.02833406	0.0548099	0.079881196	0.10366	0.12623468	0.223971084	0.365840842	0.463856025	0.5356289	0.59045423	0.633700832	0.66868639	0.6975716	0.721824062	0.742475564
Mg/Ca	0.01514	0.03737	0.07401	0.11040	0.145743672	0.28334832	0.413652998	0.53722	0.654569	1.162540873	1.899889916	2.409310685	2.7823405	3.06728785	3.292056293	3.47388906	3.62401606	3.750064961	3.857398378
Sr/Ca																			
SO4/Ca	1.00504	1.01255	1.02492	1.03721	1.049146711	1.09561674	1.139621526	1.18135	1.22098051	1.39252609	1.641533912	1.813568795	1.9395435	2.03577219	2.111678033	2.1730842	2.22378312	2.266350697	2.302597927

[X/Ca] (mol/mol) in calcite from dissolving gypsum + water (used high distribution coefficients)

Ratios	0.1:1	0.25:1	0.5:1	0.75:1	1:1	2:1	3:1	4:1	5:1	10:1	20:1	30:1	40:1	50:1	60:1	70:1	80:1	90:1	100:1
Na/Ca	0.000022	0.000051	0.000099	0.000148	0.000194	0.000376	0.000548	0.000711	0.000867	0.001538	0.002512	0.003185	0.003678	0.004054	0.004351	0.004591	0.004790	0.004956	0.005098
K/Ca	0.000001	0.000002	0.000004	0.000006	0.000009	0.000016	0.000024	0.000031	0.000038	0.000067	0.000110	0.000139	0.000161	0.000177	0.000190	0.000201	0.000209	0.000217	0.000223
Mg/Ca	0.003179	0.007848	0.015542	0.023184	0.030606	0.059503	0.086867	0.112817	0.137459	0.244134	0.398977	0.505955	0.584292	0.644130	0.691332	0.729517	0.761043	0.787514	0.810054
Sr/Ca																			
SO4/Ca	0.000181	0.000182	0.000184	0.000187	0.000189	0.000197	0.000205	0.000213	0.000220	0.000251	0.000295	0.000326	0.000349	0.000366	0.000380	0.000391	0.000400	0.000408	0.000414

[X/Ca] (ppm/ppm) in calcite from dissolving gypsum + water (used high distribution coefficients)

Ratios	0.1:1	0.25:1	0.5:1	0.75:1	1:1	2:1	3:1	4:1	5:1	10:1	20:1	30:1	40:1	50:1	60:1	70:1	80:1	90:1	100:1
Na/Ca	0.0000124845	0.0000294	0.0000572	0.0000849	0.000112	0.000216	0.000315	0.000409	0.000498	0.000884	0.001444	0.001831	0.002115	0.002331	0.002502	0.002640	0.002754	0.002850	0.002931
K/Ca	0.0000009374	0.0000022	0.0000043	0.0000063	0.000008	0.000016	0.000023	0.000030	0.000037	0.000066	0.000107	0.000136	0.000157	0.000173	0.000185	0.000196	0.000204	0.000211	0.000217
Mg/Ca	0.0019073758	0.0000000	0.0000000	0.0000000	0.000000	0.000000	0.000000	0.000000	0.000000	0.000000	0.000000	0.000000	0.000000	0.000000	0.000000	0.000000	0.000000	0.000000	0.000000
Sr/Ca																			
SO4/Ca	0.0004341774	0.0004374	0.0004428	0.0004481	0.000453	0.000473	0.000492	0.000510	0.000527	0.000602	0.000709	0.000783	0.000838	0.000879	0.000912	0.000939	0.000961	0.000979	0.000995

APPENDIX 3

Sample	Type	Na (ppm)	Mg (ppm)	K (ppm)	Ca (ppm)	V (ppb)
R1-D127	Evaporite	159.90	4440.40	161.33	392683.58	445.06
R1-D133	Evaporite	477.45	10732.60	355.73	382611.48	1701.72
R1-D140	Evaporite	153.60	2019.43	130.43	396013.49	566.86
R1-D149	Evaporite	323.93	1673.39	326.37	394401.96	975.90
R1-D156	Evaporite	261.67	15067.90	214.72	370623.99	1114.47
R1-D138(2)	Evaporite	1093.57	3154.95	200.81	393092.22	432.99
R2-D2-7	Evaporite	164.49	43661.92	60.73	339580.44	830.28
R1-D165	Non-evaporite	481.82	4957.16	427.27	387740.52	1159.21
R1-D128	Evaporite	285.99	9977.07	226.81	384414.88	791.23
R1-D135	Non-evaporite	512.80	2036.47	284.32	393201.63	1767.21
R1-D141	Evaporite	435.08	16861.11	111.61	373370.44	627.73
R2-D2-10	Evaporite	166.60	59649.12	53.57	318193.03	743.80
R1-D151	Evaporite	1828.15	2110.56	466.69	390912.67	1322.85
R1-D158	Evaporite	456.96	8673.01	328.61	382123.31	963.43
R2-D2-5	Evaporite	152.56	25123.71	156.31	364168.10	1247.12
R1-D142	Evaporite	107.51	1604.23	130.65	396586.49	610.37
R1-D136	Evaporite	8278.60	3190.98	158.55	385342.02	1729.90
R1-D129	Evaporite	5022.67	2255.43	117.36	390808.82	1066.26
R2-D2-8	Non-evaporite	17179.32	41819.17	212.30	323353.97	3210.28
R1-D150	Evaporite	7000.97	8868.19	472.68	374741.32	1918.92
R2-D2-6	Non-evaporite	5685.91	14818.46	167.10	373329.81	1975.38
R1-D157	Evaporite	6633.30	2377.27	498.81	386760.08	1911.05
R1-D137	Evaporite	5580.65	10149.87	129.68	378626.31	1276.27
R2-D2-3	Evaporite	595.42	20142.26	46.94	368970.58	462.29
R1-D130	Evaporite	816.78	1889.56	252.32	395596.12	451.49
R1-D156(2)	Evaporite	251.90	14917.73	195.63	370762.44	1091.82
R1-D159	Non-evaporite	841.52	11071.25	210.31	377072.78	640.75
R2-D2-12	Evaporite	262.26	3178.73	95.20	395124.41	566.11
R1-D143	Evaporite	705.61	3833.04	136.17	392403.39	449.47
R1-D152	Evaporite	816.33	6064.89	127.20	386914.49	397.52
R1-D161	Evaporite	1110.09	17578.63	201.23	365164.47	930.43
R1-D131	Evaporite	1067.76	28913.89	158.35	357604.96	1233.84
R1-D144	Evaporite	1158.33	5786.08	151.86	387963.10	791.88
R1-D155	Evaporite	1384.61	2727.45	570.20	390398.31	1713.31
R2-D2-19	Non-evaporite	738.97	9509.00	198.15	386552.90	1022.81
R1-D139	Evaporite	789.16	16710.15	128.89	373352.37	795.47
R2-D2-2	Evaporite	711.77	75292.95	105.11	276694.35	1515.04
R1-D162	Evaporite	795.11	11710.39	245.86	375954.05	882.09
R1-D132	Non-evaporite	725.75	11155.26	250.82	382561.78	1135.31
R1-D159(2)	Non-evaporite	818.12	10786.87	218.39	377433.80	594.28
R2-D2-13	Evaporite	9789.47	59504.26	137.44	305519.94	2747.44
R1-D138	Evaporite	1039.94	3063.38	189.53	393222.12	377.57
R1-D154	Evaporite	502.51	2720.01	225.20	392166.03	503.40
R2-D2-4	Evaporite	259.39	18161.81	211.75	372805.40	1940.52

Sample	Cr (ppb)	Mn (ppb)	Fe (ppm)	Cu (ppb)	Zn (ppb)	Rb (ppb)
R1-D127	60160.22	250220.08	1638.86	964.16	0.00	519.03
R1-D133	202607.22	258169.39	3569.34	2907.04	1635.53	1490.40
R1-D140	59455.60	234350.02	1418.77	980.80	0.00	500.78
R1-D149	109809.47	439242.23	2970.91	1427.56	14229.97	1819.95
R1-D156	119014.46	809925.56	10403.28	1663.05	10934.43	1090.85
R1-D138(2)	36593.60	206319.59	1695.18	5574.91	0.00	747.83
R2-D2-7	75924.31	184497.01	5856.34	1014.93	8979.88	106.21
R1-D165	27841.18	661814.34	5095.48	2067.80	13744.58	2293.98
R1-D128	111751.12	257548.54	2728.39	1719.35	0.00	1037.26
R1-D135	689710.88	199069.45	3252.38	6614.06	4040.66	1328.27
R1-D141	113950.65	334801.20	5444.71	1851.12	0.00	362.70
R2-D2-10	27886.69	175738.85	6234.94	996.60	15860.79	99.35
R1-D151	141194.59	426706.27	3425.84	3917.84	632791.30	2125.91
R1-D158	99878.82	575949.83	6521.82	2937.27	11339.37	1347.45
R2-D2-5	44444.86	166276.42	4773.88	1709.36	9622.39	411.02
R1-D142	37400.58	284411.39	1361.16	1081.39	0.00	435.17
R1-D136	327836.83	203980.21	1867.80	43838.85	37411.43	308.39
R1-D129	176218.77	223118.75	1243.80	24172.40	20944.28	253.85
R2-D2-8	512196.63	204044.23	6352.26	63710.27	83162.26	145.40
R1-D150	192567.82	619810.08	6655.25	28394.32	102422.08	1601.48
R2-D2-6	201708.40	111660.34	2712.48	26384.16	37924.55	381.04
R1-D157	200531.05	490436.29	3155.27	28641.43	44828.95	2070.09
R1-D137	166194.95	245779.25	3266.66	22965.17	46556.98	367.04
R2-D2-3	8627.06	195622.99	5891.12	1786.62	18998.80	113.31
R1-D130	8660.46	269421.16	1056.96	1984.48	3808.24	1209.89
R1-D156(2)	115776.07	800384.87	10477.34	1310.37	19282.43	1077.11
R1-D159	10884.07	659311.17	8302.83	2583.50	24081.13	979.50
R2-D2-12	3717.95	67349.11	831.67	655.87	18977.11	292.59
R1-D143	11884.15	295456.74	2217.39	2218.95	5724.10	648.54
R1-D152	11615.73	497489.04	4657.08	2411.35	33777.33	581.86
R1-D161	66489.76	737473.14	11896.50	4486.70	24980.91	877.64
R1-D131	296291.54	415440.21	5480.21	8146.83	10908.21	582.86
R1-D144	131202.38	387826.36	3734.74	4961.54	8325.25	572.52
R1-D155	112648.58	493372.25	4051.44	5620.93	33070.92	3019.90
R2-D2-19	58512.89	85926.03	1178.01	2800.02	22518.54	768.70
R1-D139	108706.67	329300.54	5284.36	9237.27	26590.76	501.47
R2-D2-2	69778.75	602116.28	24233.35	2841.62	24522.51	281.82
R1-D162	24101.00	584721.16	8640.91	2684.66	17762.58	1086.28
R1-D132	61084.57	259893.89	3009.79	3909.44	13834.08	937.14
R1-D159(2)	10506.61	662587.68	8314.12	2574.84	23042.74	936.60
R2-D2-13	295906.48	243277.94	8474.32	31526.40	81000.91	182.77
R1-D138	30278.28	209457.31	1741.33	5242.30	7383.01	731.99
R1-D154	17898.66	489556.44	3683.51	2589.69	15201.86	1013.93
R2-D2-4	22819.17	162917.88	4645.26	1202.62	19651.50	745.62

Sample	Sr (ppb)	Y (ppb)	Mo (ppb)	Ba (ppb)	La (ppb)	Ce (ppb)	Pr (ppb)
R1-D127	324463.21	2304.17	4327.10	33928.00	2076.94	5459.07	572.46
R1-D133	234340.20	3650.77	4869.87	4802.96	3962.29	11062.72	1260.25
R1-D140	215588.68	3230.91	21831.22	2259.01	2666.30	7009.50	725.34
R1-D149	289522.63	5890.98	11417.55	5358.26	5678.80	15361.60	1726.41
R1-D156	304970.39	5808.31	13654.21	3980.83	5929.72	16812.10	1767.00
R1-D138(2)	443114.53	2722.28	34007.42	4104.81	2426.42	6576.49	658.75
R2-D2-7	79759.97	1090.06	20929.33	2372.29	901.30	2023.87	244.84
R1-D165	150360.67	25777.16	8541.57	238730.94	11601.08	42008.19	7144.73
R1-D128	533739.21	3441.84	7350.02	6055.63	2255.39	5848.12	730.29
R1-D135	558127.03	2798.70	21550.52	83791.07	2469.55	6480.51	754.62
R1-D141	261564.60	2920.41	63878.78	4744.00	2360.26	5816.45	600.68
R2-D2-10	84664.55	999.86	3657.89	2550.35	749.72	1586.67	185.86
R1-D151	464272.34	8607.02	20583.43	34000.52	8077.61	23119.77	2706.83
R1-D158	309457.29	4902.41	12793.14	3665.70	4940.86	13630.95	1472.62
R2-D2-5	103825.28	3581.02	23663.23	4346.42	2288.25	5560.48	673.17
R1-D142	253521.51	4877.54	6542.17	3172.00	4429.25	11599.03	1255.20
R1-D136	659805.88	1947.79	107703.29	10530.21	1791.99	4347.83	457.03
R1-D129	282562.73	2408.18	136563.60	4111.64	1777.38	4112.83	471.46
R2-D2-8	106188.32	1095.94	174142.77	5013.05	949.64	2112.43	249.77
R1-D150	328063.88	8865.62	79614.34	5406.21	9890.93	26459.80	2806.36
R2-D2-6	177405.73	1940.73	59788.21	4590.26	1229.82	2494.23	302.40
R1-D157	264365.28	5635.49	81614.56	5644.01	5402.78	14737.16	1620.43
R1-D137	230031.35	2575.61	58175.78	3151.37	2321.41	6103.65	651.12
R2-D2-3	80642.47	2188.15	7139.47	3214.74	1095.07	2336.77	285.15
R1-D130	280828.95	3611.53	18938.68	77312.60	3254.87	9050.95	964.05
R1-D156(2)	304132.06	5806.57	9959.51	3747.64	5860.81	16435.26	1730.15
R1-D159	325625.86	7020.71	10404.66	3812.59	6113.24	18938.83	2015.42
R2-D2-12	216941.88	1649.22	740.40	5020.21	1832.08	3885.58	411.42
R1-D143	262147.26	3731.55	2185.43	5108.56	3206.33	8252.35	872.49
R1-D152	431797.50	4515.27	0.00	4861.53	5032.79	14111.95	1448.58
R1-D161	274759.82	4269.31	12110.55	13585.21	4084.57	11033.48	1124.17
R1-D131	170205.91	3322.88	66848.89	10526.48	2937.80	8896.96	889.70
R1-D144	288949.17	4071.45	30178.41	2958.85	3350.01	8789.33	920.58
R1-D155	538274.72	10491.13	32157.93	9906.43	8714.23	25247.75	3073.60
R2-D2-19	106019.79	1811.00	2565.90	4641.72	2124.93	4519.57	533.45
R1-D139	263074.84	2884.50	13121.50	7097.82	2466.35	6552.58	664.76
R2-D2-2	59593.43	3313.05	20995.28	9187.46	2084.84	5330.01	681.73
R1-D162	342408.94	5232.00	1566.61	10197.83	4975.19	13724.75	1502.20
R1-D132	186094.89	2731.74	5093.56	2683.90	2621.67	7232.25	770.71
R1-D159(2)	319425.20	6901.32	11381.62	3840.87	6209.82	19134.95	2044.35
R2-D2-13	77974.36	2774.64	108214.84	4799.80	2608.35	6407.33	774.68
R1-D138	431949.07	2585.27	39065.75	4021.47	2397.21	6515.80	656.81
R1-D154	436063.26	7858.79	10376.68	5036.79	7146.94	20860.79	2177.93
R2-D2-4	113031.02	6678.99	1279.48	7264.28	3532.91	8524.28	1067.71

Sample	Nd (ppb)	Sm (ppb)	Eu (ppb)	Gd (ppb)	Dy (ppb)	Ho (ppb)	Er (ppb)
R1-D127	2274.45	457.88	98.52	484.19	372.05	77.52	209.78
R1-D133	5108.11	1071.34	187.69	943.22	689.82	137.55	398.10
R1-D140	2888.37	602.84	112.60	604.28	500.73	106.34	294.34
R1-D149	6987.70	1458.17	278.47	1389.65	1046.02	197.63	548.73
R1-D156	7279.75	1553.10	298.77	1510.23	1066.29	206.68	544.82
R1-D138(2)	2580.56	542.17	108.01	591.27	472.70	96.40	263.50
R2-D2-7	952.77	183.92	37.81	186.93	152.23	34.90	98.69
R1-D165	42138.17	14749.50	2667.97	12289.61	5335.73	856.45	1986.24
R1-D128	3131.89	709.10	136.22	712.25	581.85	115.56	335.96
R1-D135	3122.08	684.42	146.10	621.32	475.86	93.96	264.27
R1-D141	2439.03	516.26	102.49	529.74	414.81	87.56	248.79
R2-D2-10	725.29	146.51	31.27	159.14	134.43	31.53	83.23
R1-D151	11245.88	2577.54	474.18	2263.46	1607.12	310.74	848.81
R1-D158	6083.30	1316.39	253.32	1260.96	908.45	177.80	482.99
R2-D2-5	2720.21	577.32	112.30	587.00	478.88	103.21	300.61
R1-D142	4946.16	975.92	197.20	1026.06	800.85	157.23	465.49
R1-D136	1732.00	354.85	75.06	364.29	280.41	59.31	174.48
R1-D129	1902.31	376.53	78.45	418.52	357.18	75.37	212.52
R2-D2-8	979.51	193.85	35.39	184.54	152.11	33.65	98.49
R1-D150	11058.13	2305.97	434.32	2207.48	1687.72	338.80	916.84
R2-D2-6	1217.10	271.02	59.93	291.20	250.56	56.12	163.59
R1-D157	6580.76	1432.29	267.84	1372.77	1018.80	202.69	550.82
R1-D137	2660.12	540.75	105.44	531.07	424.70	86.89	253.58
R2-D2-3	1218.39	243.84	55.04	305.17	235.65	51.89	157.32
R1-D130	3954.76	845.27	172.63	833.43	634.38	124.69	368.88
R1-D156(2)	7225.30	1566.86	294.70	1522.11	1053.87	202.96	556.50
R1-D159	8704.11	1917.22	361.54	1879.21	1281.89	247.25	643.60
R2-D2-12	1549.74	301.55	61.21	325.80	242.54	49.60	135.61
R1-D143	3509.93	715.29	142.28	734.18	568.43	116.17	302.69
R1-D152	5811.42	1130.04	212.38	1170.30	779.87	153.06	418.20
R1-D161	4635.62	986.47	186.09	1011.41	768.38	151.94	399.27
R1-D131	3657.98	809.87	157.85	825.06	586.14	115.39	322.23
R1-D144	3729.49	753.68	145.96	802.00	619.27	128.73	374.72
R1-D155	13108.21	3066.12	553.72	2748.68	1978.93	389.58	1091.46
R2-D2-19	2052.63	412.54	74.75	405.08	310.65	60.78	165.30
R1-D139	2694.22	551.51	122.06	604.92	475.95	96.71	276.57
R2-D2-2	2929.16	579.27	129.97	654.03	427.83	92.15	250.69
R1-D162	6132.99	1309.90	242.88	1318.21	945.47	184.43	490.09
R1-D132	3142.70	651.94	129.68	632.63	502.90	99.08	291.71
R1-D159(2)	8701.01	1953.97	372.24	1882.12	1284.55	243.78	647.46
R2-D2-13	3087.15	583.13	107.60	582.25	451.48	91.33	256.51
R1-D138	2660.36	576.08	111.88	561.23	467.19	94.68	259.47
R1-D154	8963.42	1914.38	358.15	1915.94	1446.59	278.72	750.85
R2-D2-4	4345.67	983.45	193.26	1004.28	909.59	193.52	551.74

Sample	Tm (ppb)	Yb (ppb)	Lu (ppb)	206 Pb (ppb)	207Pb (ppb)	208 Pb (ppb)	U (ppb)
R1-D127	29.41	171.86	117.97	1830.30	1766.43	1778.41	120.08
R1-D133	55.98	342.79	122.79	3921.80	3756.31	3851.39	188.09
R1-D140	43.09	267.24	180.55	1006.95	906.87	940.25	163.80
R1-D149	77.78	463.97	246.52	3569.50	3370.35	3463.18	254.04
R1-D156	73.51	473.60	138.37	2861.90	2799.35	2838.53	166.11
R1-D138(2)	35.69	219.28	119.29	2389.19	2343.91	2365.22	182.17
R2-D2-7	14.44	81.00	139.76	604.72	454.29	506.99	169.45
R1-D165	208.95	1227.81	267.07	18517.72	18400.52	18674.28	388.24
R1-D128	45.94	278.91	173.50	4965.15	4951.93	4959.70	172.04
R1-D135	35.29	225.23	151.12	3626.95	3534.99	3562.16	211.54
R1-D141	33.26	181.84	179.55	1060.78	1010.76	1023.16	150.46
R2-D2-10	11.77	74.09	85.01	552.78	458.70	493.25	78.56
R1-D151	112.96	689.55	226.03	2987.15	2846.84	2950.79	257.71
R1-D158	62.53	392.36	208.62	4495.19	4466.16	4480.96	191.41
R2-D2-5	43.94	258.39	277.92	840.24	713.90	775.03	114.57
R1-D142	58.63	388.18	290.48	991.39	897.52	938.23	168.38
R1-D136	23.64	139.94	177.16	5762.40	5934.17	5857.78	158.25
R1-D129	29.35	181.03	193.33	4007.48	4178.96	4094.72	135.54
R2-D2-8	14.54	91.69	194.54	7929.38	8499.44	8239.85	133.68
R1-D150	128.31	815.76	335.87	19296.81	20525.23	20024.98	244.46
R2-D2-6	22.38	145.86	222.85	4366.14	4354.52	4327.46	325.83
R1-D157	72.69	440.32	252.96	5860.72	6039.38	5996.50	247.25
R1-D137	34.98	204.46	0.00	4064.67	4268.77	4183.43	232.52
R2-D2-3	23.08	130.94	68.30	759.66	639.50	672.93	203.38
R1-D130	51.56	304.24	43.28	2206.54	2138.11	2172.95	169.91
R1-D156(2)	72.72	457.35	77.26	2789.65	2742.60	2781.53	162.21
R1-D159	83.04	511.31	92.26	3077.88	3056.86	3092.80	159.10
R2-D2-12	17.37	98.69	57.35	628.50	484.73	548.32	184.83
R1-D143	41.82	255.41	117.33	1283.83	1184.40	1225.01	173.98
R1-D152	52.26	325.97	145.23	2108.18	2084.38	2118.99	137.95
R1-D161	54.33	341.13	82.38	3091.46	3103.66	3095.15	190.41
R1-D131	42.30	263.15	23.90	2808.60	2909.72	2821.53	199.67
R1-D144	50.96	322.68	68.58	1963.88	1956.74	1953.10	171.95
R1-D155	143.89	919.58	115.44	3941.61	3876.11	4015.39	311.20
R2-D2-19	21.73	134.16	87.89	1090.37	1069.97	1102.28	36.66
R1-D139	36.84	245.11	17.20	2348.03	2318.15	2319.90	173.00
R2-D2-2	30.89	192.61	158.27	1384.77	1195.77	1280.58	209.74
R1-D162	66.34	391.80	101.66	4575.10	4617.53	4575.14	174.90
R1-D132	42.20	259.15	89.01	2490.55	2394.65	2405.36	169.47
R1-D159(2)	87.53	537.42	185.54	3115.27	3089.67	3113.42	151.67
R2-D2-13	32.37	199.42	44.62	13033.95	13842.53	13497.84	62.42
R1-D138	34.67	213.61	77.77	2346.80	2356.08	2324.30	173.73
R1-D154	101.35	631.25	159.94	6662.64	6530.27	6622.09	232.87
R2-D2-4	79.21	465.60	164.47	5513.80	4708.43	5080.39	176.68

Sample	Type	Na (ppm)	Mg (ppm)	K (ppm)	Ca (ppm)	V (ppb)
R2-D2-19(2)	Non-evaporite	723.21	9347.71	207.95	386744.84	981.66
R1-D148	Evaporite	4206.82	2405.43	769.76	387649.19	2355.18
R1-D60	Non-evaporite	486.28	4040.60	799.94	383127.56	2826.20
R1-D90	Non-evaporite	692.81	4290.09	1267.68	386456.93	2566.00
R1-D79	Non-evaporite	9641.42	11884.85	13200.90	303130.56	29231.08
R1-D105	Non-evaporite	491.46	3447.05	1219.47	386825.53	2575.77
R1-D65	Non-evaporite	6646.67	10589.10	9580.10	320085.31	25050.07
R1-D45	Non-evaporite	1301.20	3260.16	1631.86	378865.22	4296.17
R1-D29	Non-evaporite	222.38	3434.21	280.84	390559.50	839.15
R1-D103	Non-evaporite	287.90	3257.38	536.33	384289.48	2683.88
R1-D71	Non-evaporite	2337.42	6082.38	4715.43	361374.33	11782.99
R1-D32	Non-evaporite	417.94	2941.95	883.86	387973.21	2705.38
R1-D76	Non-evaporite	2962.39	3782.92	5425.04	371864.77	11372.40
R1-D98	Non-evaporite	1827.52	5531.18	2840.76	377115.15	4947.61
R1-D63	Non-evaporite	4252.10	8285.76	6732.99	343343.08	16939.97
R1-D26	Non-evaporite	380.79	4451.08	677.31	384698.04	2127.04
R1-D73	Non-evaporite	3047.66	4407.51	4855.81	368892.45	8518.04
R1-D43	Non-evaporite	278.47	3130.68	470.08	389695.25	1171.08
R1-D100	Non-evaporite	659.01	5432.39	1151.08	383123.54	2724.47
R1-D28	Non-evaporite	443.34	2633.53	720.45	388011.51	1667.13
R1-D89	Non-evaporite	239.47	5131.23	472.88	387738.40	1508.37
R1-D61	Non-evaporite	971.82	2619.24	1992.73	378783.45	4435.02
R1-D97	Non-evaporite	406.10	7192.80	794.83	382589.55	1988.75
R1-D25	Non-evaporite	571.34	3068.27	1011.06	387090.06	2924.29
R1-D75	Non-evaporite	791.80	2962.83	1021.70	378772.39	4641.10
R1-D85	Non-evaporite	150.01	2960.46	256.77	390881.22	1015.05
R1-D72	Non-evaporite	3460.00	6058.93	6215.88	357114.18	12892.50
R1-D24	Non-evaporite	2130.93	5853.80	407.53	379192.12	1775.51

Sample	Cr (ppb)	Mn (ppb)	Fe (ppm)	Cu (ppb)	Zn (ppb)	Rb (ppb)
R2-D2-19(2)	59072.25	87277.63	1191.76	2979.05	23098.40	743.82
R1-D148	165378.69	530834.70	4153.31	22135.59	48217.76	3956.45
R1-D60	241189.40	2152162.67	9962.15	3586.51	53348.45	3986.09
R1-D90	96665.84	434591.48	5630.96	2185.53	8968.71	4054.94
R1-D79	1267625.38	2074865.36	55676.63	40963.35	136458.93	50989.56
R1-D105	138419.87	557780.72	6484.04	5136.60	8027.66	3962.74
R1-D65	264056.57	5240174.74	42093.53	10224.71	4104515.40	41781.90
R1-D45	103290.06	1127779.68	12629.44	3823.96	76804.55	6915.64
R1-D29	1976.82	484331.88	4224.86	1862.94	44103.19	1529.33
R1-D103	617170.98	536865.01	10178.32	18594.27	9581.88	1974.33
R1-D71	53060.55	2570171.16	22976.12	11583.93	164432.69	16659.30
R1-D32	23461.78	628952.80	6417.46	88418.36	63583.58	3536.69
R1-D76	176439.81	5546855.80	12691.25	2306.36	38357.89	19000.04
R1-D98	74788.43	759073.16	10660.51	15872.26	27205.08	8519.58
R1-D63	399769.88	5969500.64	30965.80	8782.72	98226.94	27412.02
R1-D26	155623.58	543223.83	8293.03	9838.76	65452.41	3334.60
R1-D73	350722.42	2127808.18	16468.96	5512.39	164248.67	18895.88
R1-D43	64478.58	872575.94	4884.70	1700.69	42959.87	2426.43
R1-D100	322435.66	597768.68	7916.21	1898.26	10294.30	3549.92
R1-D28	0.00	543310.77	6798.43	1342.17	60000.14	3785.97
R1-D89	215287.55	278010.57	4790.35	3756.60	8217.40	1957.31
R1-D61	112214.08	3857681.67	13503.33	9894.22	79871.05	8883.46
R1-D97	0.00	523013.41	7015.87	964.92	9099.64	2437.17
R1-D25	41559.49	156140.11	5940.28	3113.49	74931.47	4422.54
R1-D75	159039.79	3070036.81	14705.94	13602.04	20581.71	4385.35
R1-D85	21601.57	407388.76	4502.57	2642.52	23373.23	1242.90
R1-D72	206186.33	2786920.06	24259.43	8648.11	158579.08	22248.22
R1-D24	75164.50	1126957.03	8137.02	2065.60	2880626.03	1592.07

Sample	Sr (ppb)	Y (ppb)	Mo (ppb)	Ba (ppb)	La (ppb)	Ce (ppb)	Pr (ppb)
R2-D2-19(2)	105580.01	1816.09	177.55	4689.60	2149.72	4567.71	531.09
R1-D148	430775.09	11527.04	63749.76	52489.46	10352.65	28387.41	3496.42
R1-D60	850711.98	22934.51	14909.40	88751.64	7921.03	23999.43	3204.90
R1-D90	921553.33	13791.15	6791.76	108707.17	10449.55	26586.80	3554.52
R1-D79	1333531.14	64432.46	42934.37	1519184.87	19438.62	70670.93	9653.22
R1-D105	1039056.84	19622.91	3621.38	44098.01	8890.68	29174.68	3695.63
R1-D65	720322.62	121700.69	105282.39	1820180.37	32326.77	121446.28	20103.44
R1-D45	1681200.86	20039.13	20393.51	113255.81	9949.26	31843.10	3714.75
R1-D29	831074.90	10970.40	3172.28	17866.03	7226.85	15715.91	2171.46
R1-D103	993459.68	17232.88	18342.19	26781.13	9964.90	28454.74	3371.75
R1-D71	647206.40	63053.48	16096.08	326348.39	20230.25	81159.73	10528.03
R1-D32	871994.78	11589.87	1742.34	46695.63	8075.18	19815.81	2919.44
R1-D76	1114929.14	188648.01	32991.14	467319.85	31483.06	94762.09	16030.64
R1-D98	802481.97	27495.77	15605.86	171864.39	13051.22	41578.52	5773.54
R1-D63	590784.55	104835.25	5897.65	2879492.18	26394.25	110129.88	18329.85
R1-D26	738619.70	10825.58	21403.96	38228.05	9313.45	18535.69	2606.82
R1-D73	815485.36	54912.48	44343.38	356513.87	17113.66	69140.75	8716.02
R1-D43	1142703.38	7387.51	15109.96	36879.45	4551.46	11228.33	1603.97
R1-D100	758665.06	13818.97	7277.16	68514.55	9368.35	26297.40	3348.81
R1-D28	1020301.70	21051.89	15102.62	33988.81	12745.46	27750.19	3916.41
R1-D89	818232.30	7915.06	13222.19	35034.09	6541.81	14851.24	2013.53
R1-D61	1286515.60	76887.18	5774.65	224506.43	27088.29	102395.17	12531.05
R1-D97	670643.38	12235.71	20884.77	41688.34	9713.33	26009.01	3368.99
R1-D25	1806365.57	10519.80	24153.68	57645.59	5729.53	12711.07	1897.26
R1-D75	983227.50	64438.58	30094.76	209198.56	13222.47	49129.78	5477.53
R1-D85	885977.88	12012.91	17318.83	20627.57	10084.23	26000.25	3220.04
R1-D72	910025.72	79020.51	11676.31	343986.31	24285.88	96027.08	11493.25
R1-D24	348072.76	12713.60	2290.74	83926.16	8201.78	17943.35	2563.59

Sample	Nd (ppb)	Sm (ppb)	Eu (ppb)	Gd (ppb)	Dy (ppb)	Ho (ppb)	Er (ppb)
R2-D2-19(2)	2080.30	396.46	82.18	415.86	319.15	61.24	169.86
R1-D148	14979.73	3340.97	599.62	3077.14	2101.63	409.01	1121.77
R1-D60	16057.12	4663.73	1076.11	5019.00	3916.96	765.96	2011.65
R1-D90	15739.70	3831.87	775.12	3549.81	2572.73	495.03	1303.99
R1-D79	51742.79	18438.86	4419.19	18441.31	13233.41	2380.13	6087.75
R1-D105	17709.78	4665.70	968.36	4417.53	3389.53	669.37	1767.29
R1-D65	101848.36	33057.61	8780.82	39657.55	28103.32	4773.23	11145.79
R1-D45	17390.03	4488.42	1001.11	4651.08	3574.93	709.92	1911.81
R1-D29	9199.39	2129.63	448.80	2148.04	1796.22	366.74	993.39
R1-D103	14978.69	3652.22	746.20	3659.45	3018.06	608.97	1708.19
R1-D71	52332.11	15892.48	3611.89	16867.87	12651.72	2331.58	6000.40
R1-D32	12240.73	2733.95	564.25	2628.81	2180.34	434.02	1261.86
R1-D76	82302.86	30647.21	7161.57	37474.95	33274.23	6096.62	15195.70
R1-D98	27213.18	7168.50	1483.49	6801.25	5274.11	972.65	2656.69
R1-D63	96371.92	31319.44	8595.32	36611.68	25418.40	4087.92	9513.87
R1-D26	11304.91	2471.85	524.01	2348.99	1782.58	342.56	929.68
R1-D73	42859.46	13808.53	3188.01	14551.18	10590.08	1973.93	5120.52
R1-D43	7120.77	1606.39	330.24	1600.85	1194.05	235.99	674.18
R1-D100	14875.29	3745.63	763.24	3526.98	2585.98	485.49	1332.58
R1-D28	17639.38	4327.13	985.66	4526.60	3909.99	770.60	2095.95
R1-D89	8668.17	1958.99	388.45	1803.05	1338.40	266.94	709.06
R1-D61	60492.28	15923.02	3678.27	17560.82	13984.56	2681.35	7091.13
R1-D97	14693.61	3498.78	677.56	3141.69	2315.06	440.50	1209.06
R1-D25	8836.87	2320.63	513.46	2285.80	1737.57	343.90	896.51
R1-D75	26573.35	8923.67	2579.53	12292.00	11024.46	2131.72	5604.23
R1-D85	13743.66	3166.22	643.58	2990.35	2252.38	436.54	1147.90
R1-D72	56362.59	17223.31	4191.66	19284.73	15516.60	2929.28	7563.08
R1-D24	11478.97	2582.40	559.61	2591.41	1941.07	383.63	1058.58

Sample	Tm (ppb)	Yb (ppb)	Lu (ppb)	206 Pb (ppb)	207Pb (ppb)	208 Pb (ppb)	U (ppb)
R2-D2-19(2)	23.10	137.62	165.56	1125.97	1105.68	1137.53	35.24
R1-D148	144.51	924.05	226.39	5979.68	5760.85	5971.61	377.27
R1-D60	264.42	1629.86	353.65	2547.47	2409.68	2444.54	508.50
R1-D90	173.70	1075.59	176.86	3700.00	3495.62	3693.02	444.40
R1-D79	823.08	5029.73	846.17	46775.54	44601.21	46610.54	1740.26
R1-D105	233.55	1456.96	300.07	1603.45	1368.80	1457.16	481.03
R1-D65	1380.23	8508.72	1240.58	425276.72	422444.58	427382.15	1097.06
R1-D45	260.92	1730.81	311.47	2457.05	2185.03	2418.85	558.15
R1-D29	136.57	857.63	191.75	2443.00	2397.91	2401.14	413.21
R1-D103	234.16	1517.16	274.95	962.89	836.67	900.43	217.28
R1-D71	789.24	5042.36	621.07	12392.33	11767.55	12329.47	737.38
R1-D32	174.49	1142.81	202.46	3409.81	3403.16	3535.89	154.38
R1-D76	1881.58	11321.52	1109.66	203230.27	199082.45	203274.66	1221.31
R1-D98	347.33	2104.48	234.88	7536.96	7139.20	7408.71	420.77
R1-D63	1141.60	7358.33	516.68	233383.94	232390.11	234884.95	655.35
R1-D26	125.27	778.62	137.64	2266.85	2099.16	2157.74	338.66
R1-D73	686.25	4391.52	413.67	29740.66	28653.26	29599.00	905.14
R1-D43	90.86	550.23	121.55	3005.84	2855.71	2942.73	267.38
R1-D100	180.03	1129.58	197.35	2974.39	2743.63	2951.76	284.88
R1-D28	278.27	1660.66	253.53	3637.65	3393.64	3430.73	693.57
R1-D89	95.25	581.69	135.17	1229.30	1132.94	1197.32	256.57
R1-D61	942.39	5786.24	812.57	3346.52	3140.57	3385.94	211.89
R1-D97	159.85	998.04	221.16	1489.34	1291.43	1432.09	288.16
R1-D25	118.13	701.20	110.54	19385.84	18483.26	18769.66	483.67
R1-D75	766.42	4761.63	648.34	14326.47	13807.51	14246.89	685.00
R1-D85	153.76	998.59	219.88	2732.02	2562.59	2646.18	409.62
R1-D72	1020.87	6290.75	867.32	26430.51	25299.07	26292.88	1116.87
R1-D24	142.19	863.91	158.14	4073.22	3819.72	3908.59	520.07

APPENDIX 4

PHREEQC Modern Evaporation Model Code

```
#must use DATABASE pitzer.dat
SOLUTION 1 Modern Seawater
units mmol/kgw
density 1.014
pH 8.0 # estimated
Ca 10.6
Mg 55.1
Na 485.2
K 10.6
S(6) 29.2
Cl 565.7
Br 0.86
Sr 0.09
EQUILIBRIUM_PHASES
# carbonates...
CO2(g) -3.5 10; Calcite 0 0
# sulfates...
Gypsum 0 0; Anhydrite 0 0; Glauberite 0 0; Polyhalite 0 0
Epsomite 0 0; Kieserite 0 0; Hexahydrite 0 0
# chlorides...
Halite 0 0;
USER_GRAPH Example 17B
-head H2O Na K Mg Ca Cl SO4 Calcite Gypsum Anhydrite Halite\
Glauberite Polyhalite
-init false
-axis_scale x_axis 0 100
-axis_scale y_axis -5 1. 1
-axis_scale sy_axis -5 10 5 100
-axis_titles "Concentration factor" "Log(Molality)" "Log(Moles of solid)"
-chart_title "Evaporating Modern Sea water"
-start
10 graph_x 1 / tot("water")
20 graph_y log10(tot("Na")), log10(tot("K")), log10(tot("Mg")), log10(tot("Ca")),\
log10(tot("Cl")), log10(tot("S"))
30 if equi("Calcite") > 1e-5 then graph_sy log10(equi("Calcite")) else graph_sy -5
35 if equi("Gypsum") > 1e-5 then graph_sy log10(equi("Gypsum")) else graph_sy -5
40 if equi("Anhydrite") > 1e-5 then graph_sy log10(equi("Anhydrite")) else graph_sy -5
50 if equi("Halite") > 1e-5 then graph_sy log10(equi("Halite")) else graph_sy -5
60 if equi("Glauberite") > 1e-5 then graph_sy log10(equi("Glauberite")) else graph_sy -5
70 if equi("Polyhalite") > 1e-5 then graph_sy log10(equi("Polyhalite")) else graph_sy -5
80 if STEP_NO > 20 THEN PRINT "x", "Na", "K", "Mg", "Ca", "Cl", "S"
90 if STEP_NO > 20 THEN PRINT 1 / tot("water"), (tot("Na")), (tot("K")), (tot("Mg")),\
(tot("Ca")), (tot("Cl")), (tot("S"))
-end
REACTION
H2O -1; 0 36 3*4 6*1 2*0.25 0.176 4*0.05 5*0.03
```

```
INCREMENTAL_REACTIONS true
END
```

PHREEQC Precambrian Evaporation Model Code

```
#must use DATABASE pitzer.dat
SOLUTION 1 PC Seawater
units mmol/kgw
density 1.014
pH 9.0 # estimated
Ca 9
Mg 50
Na 456
K 1
S(6) 3
Cl 565
HCO3 18
EQUILIBRIUM_PHASES
# carbonates...
CO2(g) -3.5 10; Calcite 0 0
# sulfates...
Gypsum 0 0; Anhydrite 0 0; Glauberite 0 0; Polyhalite 0 0
Epsomite 0 0; Kieserite 0 0; Hexahydrite 0 0
# chlorides...
Halite 0 0; Bischofite 0 0; Carnallite 0 0
USER_GRAPH Example 17B
-head H2O Na K Mg Ca Cl SO4 Calcite Gypsum Anhydrite Halite\
Glauberite Polyhalite
-init false
-axis_scale x_axis 0 100
-axis_scale y_axis -5 1. 1
-axis_scale sy_axis -5 10 5 100
-axis_titles "Concentration factor" "Log(Molality)" "Log(Moles of solid)"
-chart_title "Evaporating Modern Sea water"
-start
10 graph_x 1 / tot("water")
20 graph_y log10(tot("Na")), log10(tot("K")), log10(tot("Mg")), log10(tot("Ca")),\
log10(tot("Cl")), log10(tot("S"))
30 if equi("Calcite") > 1e-5 then graph_sy log10(equi("Calcite")) else graph_sy -5
35 if equi("Gypsum") > 1e-5 then graph_sy log10(equi("Gypsum")) else graph_sy -5
40 if equi("Anhydrite") > 1e-5 then graph_sy log10(equi("Anhydrite")) else graph_sy -5
50 if equi("Halite") > 1e-5 then graph_sy log10(equi("Halite")) else graph_sy -5
60 if equi("Glauberite") > 1e-5 then graph_sy log10(equi("Glauberite")) else graph_sy -5
70 if equi("Polyhalite") > 1e-5 then graph_sy log10(equi("Polyhalite")) else graph_sy -5
80 if STEP_NO > 20 THEN PRINT "x", "Na", "K", "Mg", "Ca", "Cl", "S"
90 if STEP_NO > 20 THEN PRINT 1 / tot("water"), (tot("Na")), (tot("K")), (tot("Mg")),\
(tot("Ca")), (tot("Cl")), (tot("S"))
-end
```

```
REACTION
H2O -1; 0 36 3*4 6*1 2*0.25 0.176 4*0.05 5*0.03
INCREMENTAL_REACTIONS true
END
```

APPENDIX 5

XRD patterns of insoluble residue after the CAS extractions.

R1-D131 (Breccia)

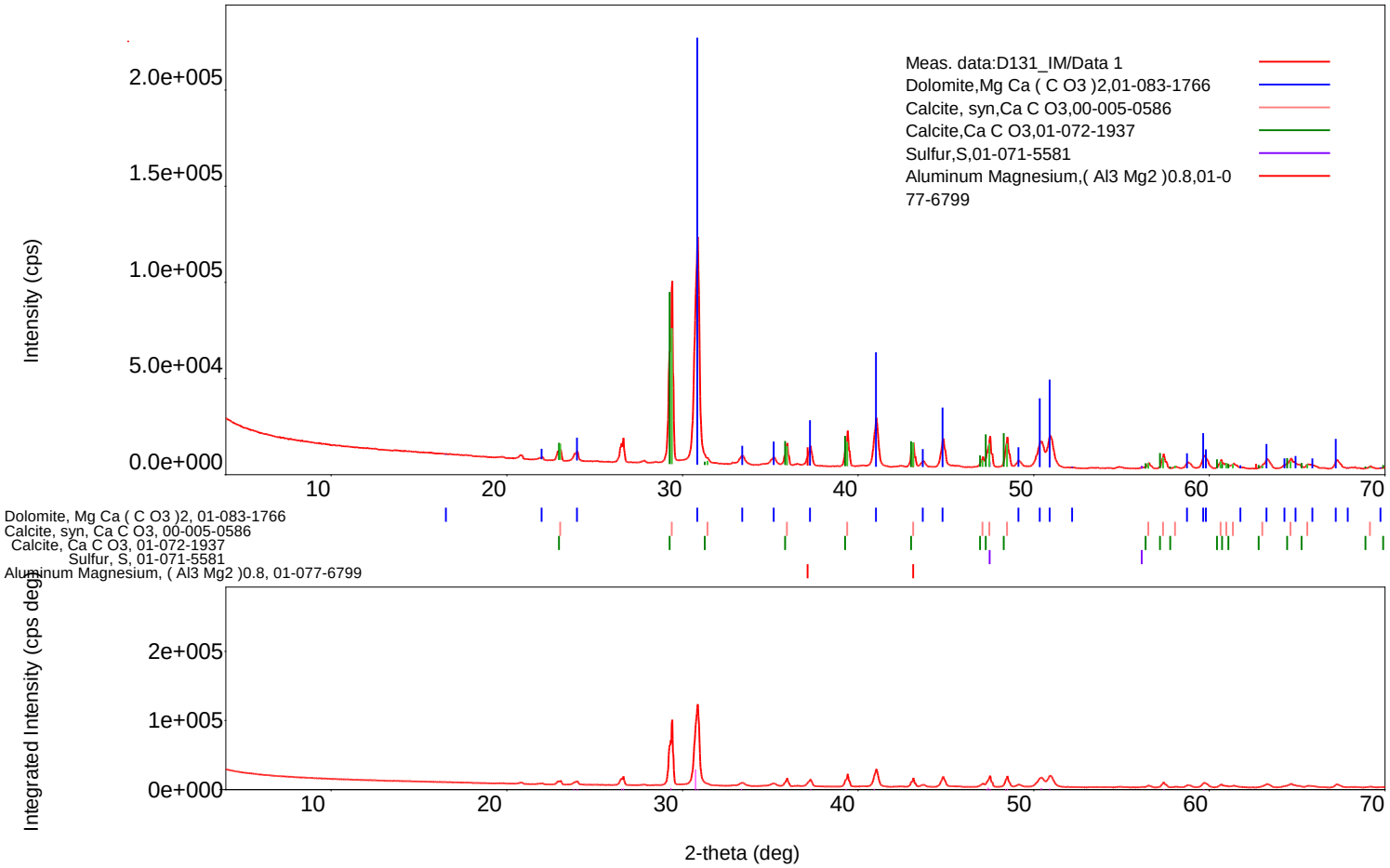

R1-D154 (Breccia)

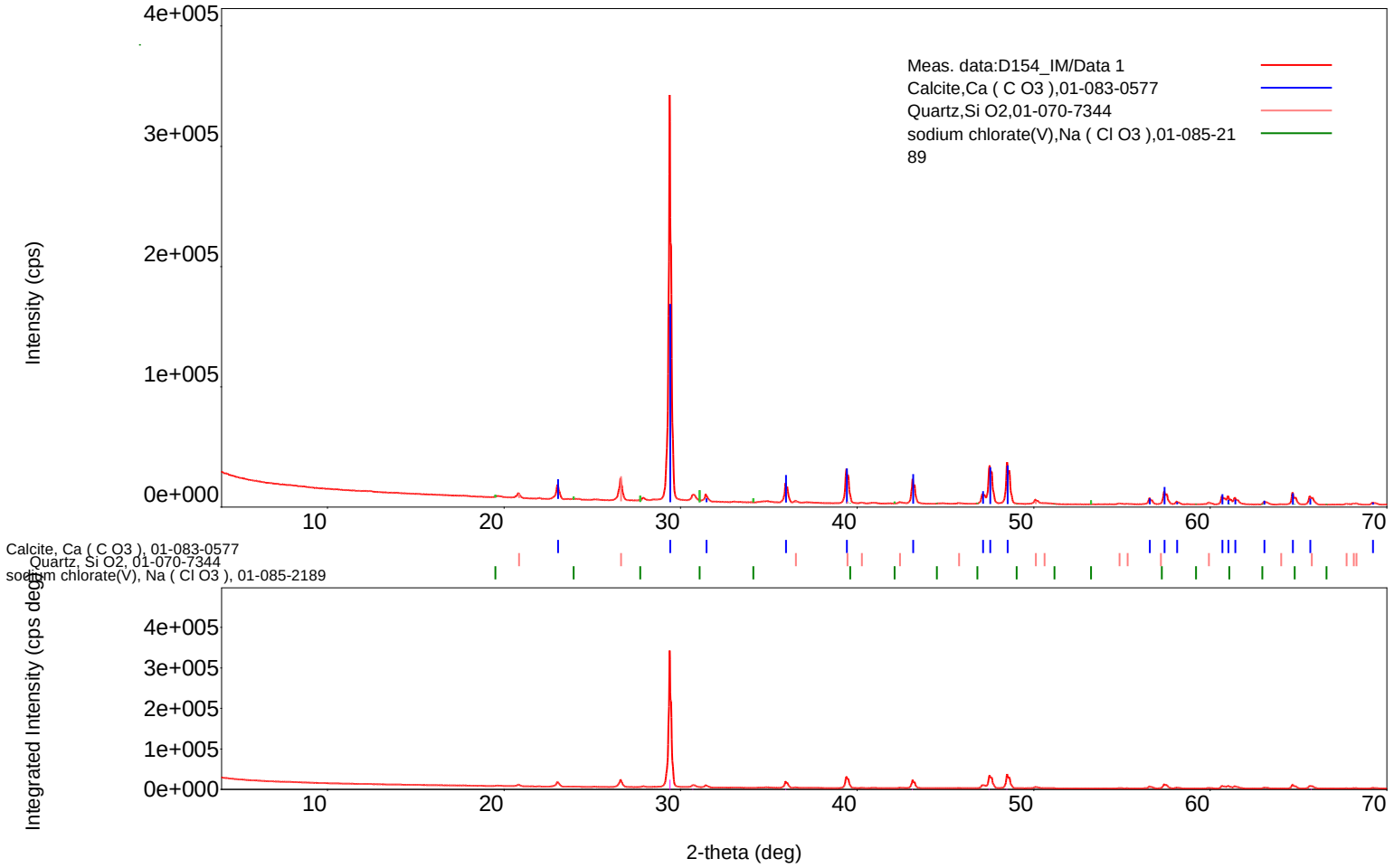

APPENDIX 6

Sem Elemental Distribution Maps

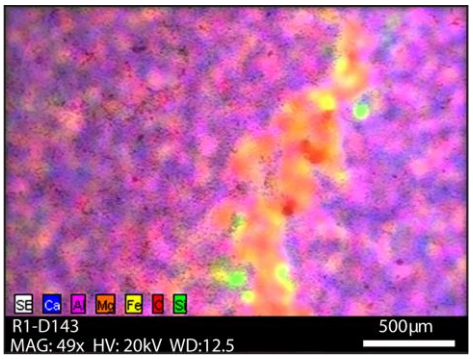

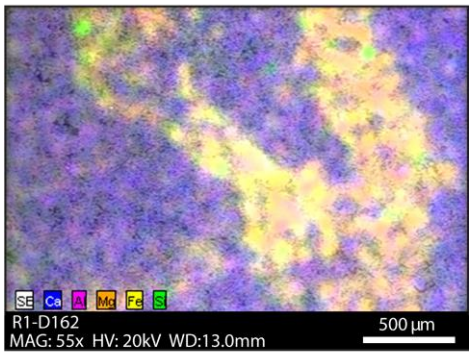

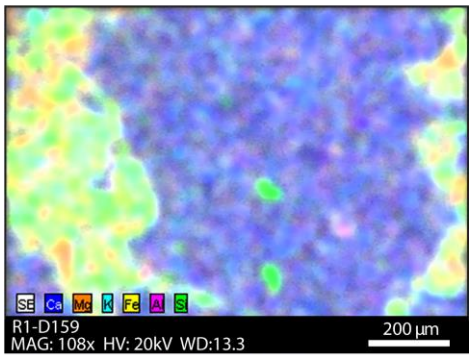

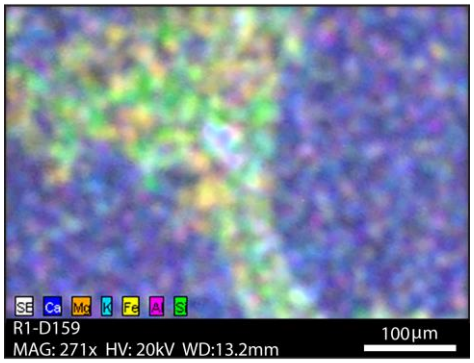

Calcium
Aluminum
Magnesium
Silicon
Iron
Potassium

VITA

Ashley Manning-Berg received her Bachelors of Science degree at the University of West Georgia in 2009. While obtaining her B.S. she received the Department of Defense Science, Mathematics, And Research for Transformation (SMART) fellowship. After finishing her degree, she worked as a research geologist at the Army Corps of Engineers–Engineer Research and Development Center where she received several awards including the Achievement Medal for Civilian Service. In 2012 she moved to Tennessee and began working towards her Master's degree. Ashley plans to continue her education by returning to the University of Tennessee in the fall as a PhD student.